

Synchrotron radiation techniques and their application to actinide materials

R. Caciuffo 

European Commission, Joint Research Centre (JRC),
Postfach 2340, DE-76125 Karlsruhe, Germany
and Istituto Nazionale di Fisica Nucleare,
Via Dodecaneso 33, IT-16146 Genova, Italy

G. H. Lander

European Commission, Joint Research Centre (JRC),
Postfach 2340, DE-76125 Karlsruhe, Germany
and Interface Analysis Centre, School of Physics, University of Bristol,
Tyndall Avenue, Bristol BS8 1TL, United Kingdom

G. van der Laan 

Diamond Light Source, Harwell Science and Innovation Campus,
Didcot OX11 0DE, United Kingdom

 (published 3 March 2023)

Research on actinide materials, both basic and applied, has been greatly advanced by the general techniques available from high-intensity photon beams from x-ray synchrotron sources. The most important single reason is that such x-ray sources can work with minute (e.g., microgram) samples, and at this level the radioactive hazards of actinides are significantly reduced. The form and encapsulation procedures used for different techniques are discussed, followed by the basic theory for interpreting the results. To demonstrate the potential of synchrotron radiation techniques for the study of lattice and electronic structure, hybridization effects, multipolar order, and lattice dynamics in actinide materials, a selection of x-ray diffraction, resonant elastic x-ray scattering, x-ray magnetic circular dichroism, resonant and nonresonant inelastic scattering, dispersive inelastic x-ray scattering, and conventional and resonant photoemission experiments are reviewed.

DOI: [10.1103/RevModPhys.95.015001](https://doi.org/10.1103/RevModPhys.95.015001)

CONTENTS

I. Introduction	2	1. Thomson scattering	11
II. Samples and Beamlines	2	2. Nonresonant inelastic x-ray scattering	11
III. Introduction to the Theory	4	3. Generalized spin-orbit sum rule	12
A. Interaction of radiation with electronic matter	4	4. Nonresonant magnetic scattering	12
1. The Hamiltonian	4	E. Resonant scattering	13
2. Kramers-Heisenberg formula	5	1. Resonant elastic x-ray scattering	13
3. Green's function approach	6	2. Resonant inelastic x-ray scattering	14
4. Initial- and final-state wave functions	6	IV. X-Ray Diffraction Experiments	15
5. Specific x-ray spectroscopies	7	A. High-pressure experiments	15
B. X-ray absorption spectroscopy	7	B. High intensity and resolution	16
1. Transition-matrix element	7	C. Experiments at high magnetic fields	18
2. Sum rules	8	D. Materials science and microstructural studies	18
3. Isotropic spectrum	9	V. REXS Experiments	20
4. X-ray magnetic circular dichroism	9	A. Electric-quadrupole order	20
5. X-ray absorption fine structure	9	B. General trends in REXS studies	22
C. X-ray photoelectron spectroscopy	10	VI. XAS Experiments	24
1. Core-level photoemission	10	A. Examples of XAS studies on actinide systems	25
2. Angle-resolved PES	10	B. Examples of EXAFS studies on actinides	27
3. Resonant PES	11	C. Examples of XMCD studies on actinides	29
D. Nonresonant scattering	11	VII. RIXS and Resonant X-Ray Emission Spectroscopy Experiments	33
		VIII. NIXS Experiments	35
		IX. High-Resolution IXS Experiments	37
		X. PES and ARPES Experiments	39
		A. Core-level photoemission	40
		B. ARPES	41

*Corresponding author.
roberto.caciuffo@ge.infn.it, rgm.caciuffo@gmail.com

XI. Conclusions	43
Acknowledgments	44
References	44

I. INTRODUCTION

Actinides are the heaviest chemical elements available on a macroscopic scale. The complexity of their electronic structure often produces exotic physical properties, such as heavy-Fermi-liquid ground states (Coleman, 2007) and unconventional superconductivity (Sarraf *et al.*, 2002; Aoki *et al.*, 2007). The richness of actinide physics has multiple origins (Moore and van der Laan, 2009; Caciuffo, 2014). The strong Coulomb repulsion between electrons in the open $5f$ shell favors electron localization and the formation of large magnetic moments. This is contrasted by the effects of the hybridization between $5f$ and conduction or neighboring-atom electronic states, promoting the opposite tendency toward itinerancy. This competition between localization and itinerancy results in frail, narrow-band $5f$ states that can be driven by small perturbations toward one behavior or the other. The complexity of actinides is due largely to this instability. Moreover, when quantum fluctuations become large enough, magnetism disappears and a new kind of order may develop, unveiling new physics beyond the “standard” Landau-Fermi liquid theory (von Löhneysen *et al.*, 2007).

Relativistic effects are a second source of complexity in actinide materials. Whereas the mass increase due to core electrons moving at almost 70% of the speed of light affects the orbit size and the screening of the nuclear charge, strong spin-orbit coupling and the presence of unquenched orbital degrees of freedom give rise to a rich variety of phenomena involving dipole and higher-order electromagnetic multipole interactions. These interactions influence the dynamics of the system and may also drive exotic phase transitions with hidden (nondipolar) order parameters that have inspired many different theoretical models (Santini *et al.*, 2009; Mydosh, Oppeneer, and Riseborough, 2020).

X-ray synchrotron radiation (SR) techniques provide powerful tools to unravel the complexity of actinide materials. These element- and shell-specific techniques probe spatial and temporal fluctuations of structural and electronic degrees of freedom, allowing one to observe hidden order parameters and characterize elementary excitations with high sensitivity and resolution (Caciuffo and Lander, 2021). Contrary to neutron scattering, SR experiments require samples only on the microgram scale. This is important for actinides, as large quantities considerably raise the radioactive inventory, thus breaching safety limits imposed at a general user facility, and large single crystals are also rarely obtained.

A central feature of the research on actinides is illustrated by Fig. 1 and the atomic volume as a function of electron count across the $3d$, $4f$, and $5f$ series of elements. For $3d$ elements, the additional $3d$ electrons result in a contraction of the atomic volume as each additional electron adds to the cohesion of the element. In the $4f$ (rare-earth) series, apart from the two divalent elements Eu and Yb, the atomic volume remains practically constant across the series. This is because the $4f$ electrons are spatially located close to the nucleus and are not involved in the bonding. However, for the $5f$ (actinide)

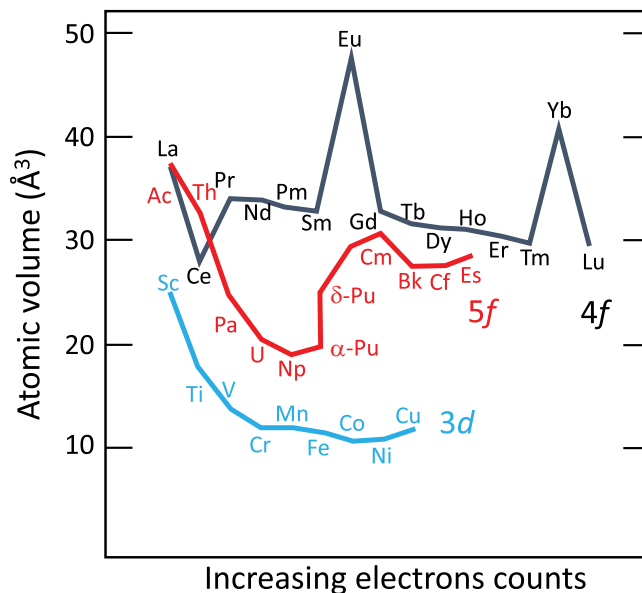


FIG. 1. Atomic volume of the transition ($3d$), rare-earth ($4f$), and actinide ($5f$) elements as a function of electron count. Note the unusual shape of the curve for the actinide series. In the case of Eu and Yb the large expansion is due to these elements being stable in the divalent state. All other rare-earth elements have the trivalent ground state. From Caciuffo and Lander, 2021.

series both behaviors are observed; an initial drop in the volume up to α -Pu, suggesting that the $5f$ states are contributing to the bonding and are therefore *itinerant* for the light actinides, and then a strong expansion for other phases of Pu and through to heavier actinide elements, hence suggesting a *localization* of the $5f$ states from Am onward.

Actinide elements, unlike most metals, crystallize in open-packed, low-symmetry structures. The behavior of elemental plutonium, which exhibits six ambient pressure allotropes, is exemplary (Zachariasen and Ellinger, 1955, 1957, 1963a; 1963b; Lashley and Lawson, 2019). A key factor in metallic actinide systems is the position of the $5f$ bands with respect to the conduction electrons, and in ionic systems we need to know the excited states and their energy differences, especially if covalency effects are induced by mixing the $5f$ states with those of p (or d) character from the neighboring anions. As we see in this review, there are many spectroscopic methods that can address these questions using x-ray techniques, including photoemission (PE). Angle-resolved PE has been particularly valuable in this respect, as the results can be compared directly to theoretical predictions. SR techniques, which provide a growing arsenal of tools for structural characterizations at atomic and mesoscopic level, as well as for electronic structure investigations, are now recognized as a major source of information on the properties of nuclear fuel, the stability of nuclear waste forms, and the behavior of actinide materials in the environment. Although these topics are of great industrial and societal importance, we do not cover them exhaustively in this review, which focuses mainly on the physics.

II. SAMPLES AND BEAMLINES

The safety concerns raised by the radiotoxicity of the samples demand the implementation of strict rules and

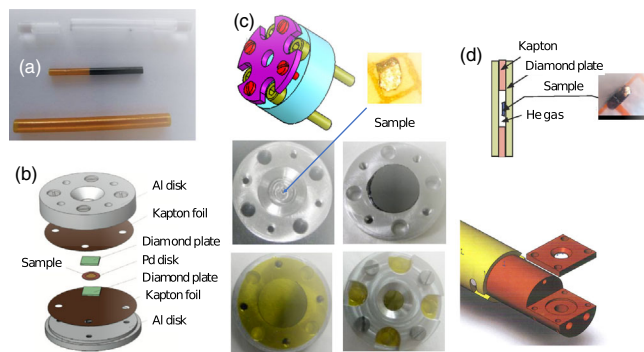


FIG. 2. Hermetic sample holders used for investigating actinide materials with different synchrotron-radiation-based techniques. (a) Low-temperature powder x-ray diffraction (Hill *et al.*, 2013). (b) Inelastic x-ray scattering in transmission geometry (Walters *et al.*, 2015). (c) X-ray magnetic circular dichroism (Lander *et al.*, 2019) and nonresonant inelastic x-ray scattering (Sundermann *et al.*, 2020). (d) Inelastic x-ray scattering in reflection geometry (Maldonado *et al.*, 2016). (c), (d) Images of ^{248}Cm ($0.6 \times 0.8 \times 0.1 \text{ mm}^3$, $m \approx 650 \mu\text{g}$) and NpO_2 ($0.78 \times 0.56 \times 0.25 \text{ mm}^3$, $m \approx 1.2 \text{ mg}$) samples used for the studies described by Maldonado *et al.* (2016) and Lander *et al.* (2019).

procedures to exclude any potential health risks and contamination of the beamline. Handling of radioisotopes should be undertaken in a properly regulated radiological facility, and hermetic sample holders with multiple level of containment should be used. Some examples are shown in Fig. 2. Figure 2(a) shows a photograph of the sample holder developed at the Joint Research Centre, Karlsruhe, Germany, for low-temperature x-ray diffraction (XRD) experiments on powder transuranium samples. It consists of a 1-mm-diameter polyimide capillary, containing the powder material mixed with a low-viscosity epoxy resin, inserted into a drilled-out plexiglass rod, which is in turn enveloped within a 4-mm-diameter polyimide tube (Hill *et al.*, 2013). Figure 2(b) shows an enlarged view of a sample holder used for inelastic x-ray scattering (IXS) measurements in transmission geometry, with the sample sandwiched between two single-crystal diamond plates, protected by Kapton foils and an aluminum case (Walters *et al.*, 2015). Figure 2(c) shows a sample holder used for x-ray magnetic circular dichroism (XMCD) and nonresonant inelastic x-ray scattering (NIXS) measurements. The sample sitting in the middle of the aluminum support is covered by a Be window glued with epoxy resin and protected by a 6- μm -thick Kapton foil. The external cover of the capsule is kept in place by screws made from a diamagnetic material (Lander *et al.*, 2019). Figure 2(d) shows the drawings of a sample holder used for IXS experiments in reflection geometry. The sample is kept between two 0.5-mm-thick single-crystal diamond slabs separated by a hollow Kapton foil (Maldonado *et al.*, 2016).

The presence of windows covering the sample can degrade the signal-to-noise quality due to the absorption of incoming and outgoing photons or because a signal originating from the windows can overlap and swamp the one coming from the sample. Their material and thickness must therefore be chosen with care. Moreover, if the windows are not transparent, hitting a small sample with an x-ray beam with dimensions of

microns can be challenging. It is then useful to glue the sample onto a single-crystal substrate and to monitor the intensity of a Bragg peak from the substrate during an x - y position scan, looking for the dip of minimum intensity expected at the sample position. Care should be taken if using any epoxy glue in a confined volume with α -emitting samples, as the glue may radiolyze, producing reactive products such as HF (Mannix, Langridge *et al.*, 1999).

Pioneering work on actinides stimulated the construction of dedicated beamlines: BL27B (Konishi *et al.*, 1996) at the Photon Factory in Tsukuba, Japan, and BL23SU (Saitoh, Nakatani *et al.*, 2001; Saitoh *et al.*, 2012) at SPring-8, in Sayo, Hyōgo Prefecture, Japan; BL 11-2 (Bargar *et al.*, 2002) at the Stanford Synchrotron Radiation Laboratory, Menlo Park, CA; MARS (Solari *et al.*, 2009) at SOLEIL, Gif-sur-Yvette, France; CAT-ACT (Dardenne *et al.*, 2009; Rothe *et al.*, 2012; Zimina *et al.*, 2017; Schacherl, Prüssmann *et al.*, 2022) at the Karlsruhe Research Accelerator (KARA, formerly ANKA) in Karlsruhe, Germany; MicroXAS (Borca *et al.*, 2009) at the Swiss Light Source, Villigen, Switzerland; and ROBL-II (Kvashnina and Scheinost, 2016; Scheinost *et al.*, 2021) at the European Synchrotron Radiation Facility (ESRF), Grenoble, France. Generally, dedicated beamlines have several experimental stations. For instance, the ROBL-II beamline, located at a bending magnet of the ESRF (Fig. 3), has four stations dedicated to (i) fluorescence and transmission detection for x-ray absorption fine-structure (XAFS) spectroscopy, including conventional x-ray absorption near-edge structure (XANES) and extended x-ray absorption fine-structure (EXAFS) spectroscopies, (ii) high-energy-resolution fluorescence-detection (HERFD) XANES, x-ray emission spectroscopy (XES), and resonant inelastic x-ray scattering (RIXS), (iii) powder x-ray diffraction (PXRD), surface-sensitive crystal truncation rod and resonant anomalous x-ray reflectivity measurements, and (iv) single-crystal x-ray diffraction and *in situ* or *in operando* PXRD.

The construction of dedicated actinide beamlines at many synchrotrons, as discussed, has greatly increased the number of experiments that have been performed over the last 20 years on actinide materials. In most cases the capability of these special actinide beamlines is sufficient, but they are usually designed to perform a variety of different tasks, so they are often not at the cutting edge of synchrotron research. It is thus important in this context that the synchrotron staff can define

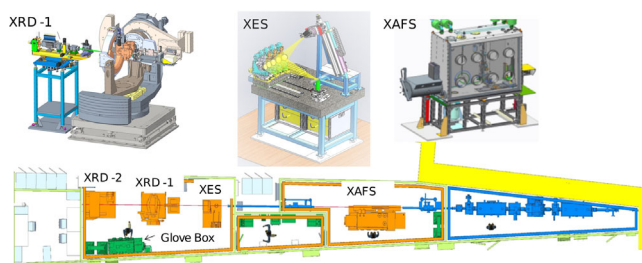


FIG. 3. Schematic layout of the ROBL-II beamline at the European Synchrotron Radiation Facility (ESRF), Grenoble. Insets: powder x-ray diffraction, x-ray emission spectroscopy, and x-ray absorption fine-structure stations. Adapted from Scheinost *et al.*, 2021.

conditions at which actinides can be used at any beamline. This has been our experience at the ESRF, where the allowed quantities of each radioactive isotope are well defined, and we have developed, together with the staff, special sample holders, several of which are shown in Fig. 2. Diamond Light Source (Harwell, England) has a dedicated radioactive materials laboratory to prepare hot samples for measurements at the beamlines.

Examples of experiments on transuranium samples that have been performed on general beamlines at the ESRF are high-pressure diffraction (Lindbaum *et al.*, 2001; Heathman *et al.*, 2005), resonant elastic x-ray scattering (REXS) (Paixão *et al.*, 2002), XMCD (Halevy *et al.*, 2012; Magnani *et al.*, 2015, 2017; Lander *et al.*, 2019), IXS (Wong *et al.*, 2003; Maldonado *et al.*, 2016), NIXS (Sundermann *et al.*, 2020), and RIXS (Heathman *et al.*, 2010). The amount of allowed radioisotopes will then be less than at a dedicated actinide beamline. For example, at a general beamline at the ESRF the radioactivity should not exceed 10 μCi (370 kBq), which gives an amount of ^{239}Pu of 160 μg . On the other hand, at the ROBL beamline experiments can be performed on samples with a maximum activity of 185 MBq, a factor of 500 higher than that on nondedicated beamlines.

Some synchrotrons state that they will not allow any radioactive material on the beamlines. However, our experience has been that one has to convince the management of the need for the special techniques available and work with them constructively to satisfy the relevant safety conditions.

III. INTRODUCTION TO THE THEORY

By providing a theoretical foundation of the most explored x-ray spectroscopies, we can point out the conceptually common aspects and classify the different processes (elastic and inelastic, resonant and nonresonant, first- and second-order transitions, coherent and incoherent).

The various kinds of x-ray spectroscopies practiced at synchrotrons around the globe have much in common: they are all based on photon absorption or scattering, as opposed to, say, electron or neutron scattering, which entail different mechanisms. Subject to Fermi's golden rule, photon processes are either direct transitions from initial to final state or second-order coherent transitions involving an intermediate state. In a few exceptional cases they are higher-order processes like the ones in nonlinear optics. Here we provide a basic introduction that serves to put the different spectroscopic techniques in perspective and place them on a common platform. One can make a distinction between the various electric- and magnetic-multipole transitions, such as dipole and quadrupole transitions, each of which can be excited with circularly or linearly polarized x rays, thus amounting to different selection rules. Furthermore, one can distinguish between nonresonant and resonant transitions, which can be either elastic or inelastic. In a resonant transition a core electron is excited into a discrete state above the Fermi level, thereby giving a strong intensity enhancement as well as a sensitivity to the local environment. Bragg scattering is an example of elastic scattering, which has a nonresonant term (Thomson scattering) and a resonant one known as anisotropy of the tensor of susceptibility or resonant elastic x-ray scattering (REXS). Inelastic scattering can also

be divided up into nonresonant inelastic x-ray scattering (NIXS) and RIXS.

The following theoretical description is based on quantum mechanics and provides a step-by-step approach to x-ray spectroscopies. After presenting the electronic Hamiltonian that empowers us to obtain the initial and final states, the interaction Hamiltonian is presented. By Fermi's golden rule, the transition contains first-order (direct) and second-order components, which can be further classified according to the number of times that the vector potential occurs.

A. Interaction of radiation with electronic matter

1. The Hamiltonian

The Hamiltonian in the nonrelativistic limit with relativistic corrections for the photon-matter interaction can be separated into electronic, radiation, and interaction parts,

$$H = H_{\text{el}} + H_{\text{rad}} + H_{\text{int}}. \quad (1)$$

For n electrons moving about a point nucleus of the charge of an atom, the Hamiltonian for the electronic part can be written in the central field approximation as

$$H_{\text{el}} = \sum_{n=1}^N \left[\frac{\mathbf{p}_n^2}{2m} + V(\mathbf{r}_n) + \frac{e\hbar}{2m^2c^2} \mathbf{s}_n \cdot [\nabla V(\mathbf{r}_n) \times \mathbf{p}_n] \right], \quad (2)$$

where e is the elementary charge, m is the electron rest mass, and c is the speed of light. The first term is the kinetic energy, which contains the momentum operator $\mathbf{p}_n = -i\hbar\nabla_n$. The second term is the potential energy V , which depends on the position vector \mathbf{r}_n of the n th electron. This potential energy collects terms such as the electrostatic (Coulomb) interactions and external (magnetic and crystal) fields. The last term is the spin-orbit interaction, in which \mathbf{s}_n is the spin vector operator, which originates from the Dirac equation.

The Hamiltonian for the radiation field is

$$H_{\text{rad}} = \sum_{\mathbf{k}\epsilon} \hbar\omega_{\mathbf{k}} [a^\dagger(\mathbf{k}\epsilon)a(\mathbf{k}\epsilon) + \frac{1}{2}], \quad (3)$$

where $\hbar\omega_{\mathbf{k}}$ is the energy of a photon with the wave vector \mathbf{k} and polarization vector ϵ . a^\dagger and a are the photon creation and annihilation operators, respectively.

An electromagnetic field consists of two vector fields, an electric field $\mathbf{E}(\mathbf{r})$ and a magnetic field $\mathbf{B}(\mathbf{r})$. Both are time-dependent vector fields that in vacuum depend on the vector potential field $\mathbf{A}(\mathbf{r})$ and the scalar field $\phi(\mathbf{r})$,

$$\mathbf{B}(\mathbf{r}) = \nabla \times \mathbf{A}(\mathbf{r}), \quad (4)$$

$$\mathbf{E}(\mathbf{r}) = -\nabla\phi(\mathbf{r}) - \frac{\partial\mathbf{A}(\mathbf{r})}{c\partial t}. \quad (5)$$

Choosing the Coulomb gauge, for which $\nabla \cdot \mathbf{A} = 0$, makes \mathbf{A} a transverse field. The Fourier expansion of the vector potential is then

$$\mathbf{A}(\mathbf{r}) = \sum_{\mathbf{k}\epsilon} \sqrt{\frac{\hbar}{2\omega_{\mathbf{k}}V\epsilon_0}} [a^\dagger(\mathbf{k}\epsilon)\boldsymbol{\epsilon}^* e^{-i\mathbf{k}\cdot\mathbf{r}} + a(\mathbf{k}\epsilon)\boldsymbol{\epsilon} e^{i\mathbf{k}\cdot\mathbf{r}}], \quad (6)$$

where V is the normalization volume and ϵ_0 is the vacuum permittivity. The time evolution is obtained by replacing $\mathbf{k} \cdot \mathbf{r}$ with $\mathbf{k} \cdot \mathbf{r} - \omega_{\mathbf{k}}t$.

For x rays, the reciprocal of \mathbf{k} is large compared to the core orbitals involved in the transition, and for $\mathbf{k} \cdot \mathbf{r} \ll 1$ Eq. (6) simplifies to the dipole approximation $\mathbf{A}(\mathbf{r}) \sim \sum_{\mathbf{k}\epsilon} [a^\dagger(\mathbf{k}\epsilon)\boldsymbol{\epsilon}^* + a(\mathbf{k}\epsilon)\boldsymbol{\epsilon}]$.

The interaction Hamiltonian that involves terms with the vector potential \mathbf{A} is (Blume, 1985; Blume and Gibbs, 1988; Schülke, 2007; Altarelli, 2013)

$$\begin{aligned} H_{\text{int}} &= \sum_{n=1}^N \left\{ \frac{e^2}{2mc^2} \mathbf{A}^2(\mathbf{r}_n) - \frac{e}{mc} \mathbf{A}(\mathbf{r}_n) \cdot \mathbf{p}_n \right. \\ &\quad - \frac{e\hbar}{mc} \mathbf{s}_n \cdot [\nabla \times \mathbf{A}(\mathbf{r}_n)] \\ &\quad \left. + \frac{e\hbar}{2m^2c^3} \mathbf{s}_n \cdot \left[\frac{\partial \mathbf{A}(\mathbf{r}_n)}{\partial t} \times \left(\mathbf{p}_n - \frac{e}{c} \mathbf{A}(\mathbf{r}_n) \right) \right] \right\} \\ &\equiv H'_1 + H'_2 + H'_3 + H'_4. \end{aligned} \quad (7)$$

For brevity, we often omit the summation over n in the following.

To shed some light on Eq. (7), the generalized momentum in the presence of an electromagnetic field is $\boldsymbol{\Pi} = \mathbf{p} - (e/c)\mathbf{A}$. Expanding the nonrelativistic kinetic energy operator $(1/2m)[\mathbf{p} - (e/c)\mathbf{A}]^2$ gives the terms H'_1 and H'_2 in H_{int} , while the term $\mathbf{p}^2/2m$ is captured in H_{el} . The H'_1 interaction gives nonresonant photon scattering, while H'_2 interacts with the charge and gives an electric-multipole transition.

The term H'_3 with $\mathbf{s} \cdot (\nabla \times \mathbf{A})$ gives an interaction of spin \mathbf{s} with the magnetic field $\mathbf{B} = \nabla \times \mathbf{A}$ of the radiation and leads to magnetic transitions. Compared to charge scattering, the magnetic scattering is smaller by a factor $(\hbar\omega/mc^2)^2$ (of the order of 10^{-4} at the M edges of uranium).

The origin of the relativistic term H'_4 is the spin-orbit interaction of the electron spin and the radiation field, not to be confused with the atomic spin-orbit interaction given in Eq. (2).

2. Kramers-Heisenberg formula

Armed with the interaction Hamiltonian, we are ready to write down the transition probability. Applying Fermi's golden rule in first- and second-order perturbation, we arrive at the Kramers-Heisenberg (KH) formula for the number of transitions per unit time (Sakurai, 1967),

$$\begin{aligned} w &= \frac{2\pi}{\hbar} \sum_f \left| \langle f | H_{\text{int}} | g \rangle + \sum_n \frac{\langle f | H_{\text{int}} | n \rangle \langle n | H_{\text{int}} | g \rangle}{E_g - E_n + \hbar\omega + i\Gamma_n/2} \right|^2 \\ &\quad \times \delta(E_g - E_f + \hbar\omega - \hbar\omega'), \end{aligned} \quad (8)$$

where the delta function indicates the energy conservation for the initial state $|g\rangle$ and the final state $|f\rangle$. Also implicitly included in the initial state is a photon that is annihilated by the vector potential \mathbf{A} given in Eq. (6).

Equation (8) contains a direct and an indirect transition; the latter contains an intermediate (virtual) state $|n\rangle$. The modulus square over these two transition terms allows for interference between different $|n\rangle$ intermediate states, leading to the same final state $|f\rangle$.

A formula equivalent to Eq. (8) was first obtained by Kramers and Heisenberg in 1925 using the correspondence principle (Kramers and Heisenberg, 1925). A classical example is provided by Rayleigh scattering, which describes the elastic scattering of light with wavelengths much longer than the particle size, where $|f\rangle = |g\rangle$ and $\hbar\omega = \hbar\omega'$. The interaction $\boldsymbol{\epsilon} \cdot \mathbf{p}$ (dipole approximation) with the incoming and outgoing photon results in a scattering cross section that varies as the inverse fourth power of the wavelength (Rayleigh's law). This theory explains why the sky is blue and the sunset is red.

In the nonresonant case, where the incident photon energy is far from the atomic binding energy, we can ignore the second-order perturbation term and the scattering is due to \mathbf{A}^2 , which in the dipole approximation becomes $\boldsymbol{\epsilon}'^* \cdot \boldsymbol{\epsilon}$, which is independent of the propagation direction. This gives the Thomson scattering, which is insensitive to the nature of the electron bonding. The Thomson cross section for light scattering by free (unbound) electrons is given by

$$\frac{d\sigma}{d\Omega} = r_0^2 (\boldsymbol{\epsilon}'^* \cdot \boldsymbol{\epsilon})^2, \quad (9)$$

where $r_0 \equiv e^2/mc^2 \equiv 2.818 \times 10^{-15}$ m is the classical electron radius or Thomson scattering length, e is the elementary charge, m is the electron mass, and c is the speed of light. The cross section is independent of ω but has a strong polarization dependence as a function of the scattering angle. For linearly polarized x rays the intensity vanishes at a scattering angle of 90° , which can be used to suppress the elastic scattering when other types of scattering are measured. For further discussion of Thomson scattering, see Sec. III.D.1. The KH formula can also be applied to inelastic scattering of light, with $\omega \neq \omega'$ and $|f\rangle \neq |g\rangle$, where in the optical region it is called the Raman effect.

Here our aim is to describe different types of x-ray spectroscopies, and the KH formula facilitates this by plugging in the various interactions. As seen in Eq. (6), the vector potential \mathbf{A} is linear in the creation and annihilation operators of the photon. Thus, $\mathbf{A}|g\rangle$ annihilates a photon in the initial state, whereas $\langle f|\mathbf{A}$ creates a photon in the final state.

SR studies imply the presence of incoming photons, either without or with emission of a secondary photon, corresponding to absorption and scattering, respectively. Emission-only processes, such as radiative deexcitation and bremsstrahlung, fall beyond the frame of these studies. We also neglect the effects of electron recoil ($\hbar\omega \ll m_e c^2$) that occur with Compton scattering.

We first consider the first-order perturbation, shown in Fig. 4(a), which corresponds to photon absorption. The vector potential \mathbf{A} is linear for the interaction terms H'_2 and H'_3 . The interaction $H'_2 \sim \mathbf{p} \cdot \mathbf{A}$ gives electric- and magnetic-multipole transitions (see Sec. III.B.1), in which a photon is absorbed under the excitation of an electron. This process encompasses both x-ray absorption spectroscopy (XAS) and photoemission spectroscopy (PES) where an electron is excited into a discrete

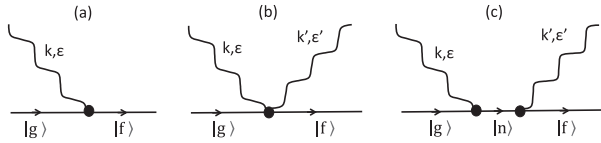


FIG. 4. Feynman diagrams representing the scattering amplitude. (a) First-order diagram for photon absorption with interaction H'_2 or H'_3 . (b) First-order diagram for photon scattering with interaction H'_1 or H'_4 . (c) Second-order diagram for photon scattering (see the text). Not shown is another second-order Feynman diagram with emission followed by absorption, which contributes to the nonresonant scattering.

or continuum state, respectively. The interaction term $H'_3 \sim \mathbf{s} \cdot (\nabla \times \mathbf{A}) = \mathbf{s} \cdot \mathbf{B}$ gives the pure magnetic absorption, which is much smaller.

The first-order perturbation is quadratic in \mathbf{A} for the interaction terms H'_1 and H'_4 , which describes photon scattering (photon in, photon out). This is shown by the so-called seagull diagram in Fig. 4(b). $H'_1 \sim \mathbf{A}^2$ gives a nonresonant process since it does not contain the momentum operator \mathbf{p} . Besides the previously mentioned elastic process of Thomson scattering, there is also an inelastic process (NIXS); see Sec. III.D.2.

Next we consider the second-order perturbation term in the KH formula shown in Fig. 4(c). This contains a scattering process involving two photons, i.e., twice the interaction $\mathbf{A} \cdot \mathbf{p}$, and an intermediate state $|n\rangle$, as in REXS and RIXS. Alternatively, there can also be second-order interaction processes that are first order in \mathbf{A} , such as resonant photoemission spectroscopy (RPES), in which the photon absorption (interaction $\mathbf{A} \cdot \mathbf{p}$) is followed by a Coulomb decay; see Sec. III.C.3. All of these processes are later treated in more detail.

Finally, nonlinear optical effects, such as the third-order process of second-harmonic generation (SHG), are also possible, although they remain largely unexplored in the x-ray region due to the relatively low photon flux compared to lasers in the optical region. The recent advent of free-electron lasers (FELs) in energy ranges from extreme ultraviolet to x rays allows us to explore these effects involving core-level resonances. In SHG an incident photon excites an electron of the atom, which is promoted to an empty state, and a second photon excites it to the next level. The state then deexcites to the equilibrium ground state under emission of a photon that, due to energy conservation, has twice the energy and frequency of the original photons. As in the case of natural circular dichroism, the process of SHG for circular dichroism is parity odd and time even, which allows one to measure the helicity of a material from the piezoelectric crystal class (van der Laan and Lovesey, 2021), such as the noncentrosymmetric uranium (IV) fluoride U_3F_{12} (H_2O).

3. Green's function approach

In the KH formula, the denominator containing the intermediate states can be written in terms of the Green's function, also referred to as the intermediate-state propagator, which describes the system in the presence of a core hole,

$$G(z) = \frac{1}{z - H} = \sum_n \frac{|n\rangle\langle n|}{z - E_n}, \quad (10)$$

where $|n\rangle$ forms a complete basis set and $z = E_g + \hbar\omega + i\Gamma/2$. This reduces the scattering amplitude to the compact expression

$$F_{gf} = \langle f | H_{\text{int}}^\dagger G(z) H_{\text{int}} | g \rangle. \quad (11)$$

Equation (11) is frequently encountered in both RPES and RIXS.

4. Initial- and final-state wave functions

The atomic wave functions can be obtained from the electronic Hamiltonian given in Eq. (2), in which $V(\mathbf{r})$ may contain external fields such as magnetic, electric, and crystal fields.

The electronic wave functions ψ_i for the initial states are obtained by finding the eigenvalues E_i of the Hamiltonian using $H_{\text{el}}\psi_i = E_i\psi_i$. By including the core-hole potential in H_{el} , one can also obtain the final states $|f\rangle = c_{m'\sigma'} \ell_{m\sigma}^\dagger |g\rangle$, where $c_{m'\sigma'}$ is the annihilation operator of a core electron c with quantum numbers m' and σ' and $\ell_{m\sigma}^\dagger$ is the creation operator of an electron ℓ in a partly empty shell with quantum numbers m and σ .

The wave function can be separated into angular and radial parts. The angular part depends on the angular quantum numbers of the basis states of the configuration and are independent of the radial wave functions. General analytical methods for calculating angular coefficients were computerized by Cowan (1981). The basis wave functions are an antisymmetrized product of one-electron functions, so-called Slater determinants. In spherical symmetry these wave functions are eigenfunctions of the total angular momentum J and its components M_J .

Upon application of a magnetic field \mathbf{B} along the quantization direction \hat{z} , the $(2J + 1)$ -fold degenerate ground state splits into its M_J sublevels with energy $g\mu_B B M_J$, of which only the level $M_J = -J$ is populated at $T = 0$ K, where $\mu_B = e\hbar/2m$ is the Bohr magneton and g is the Landé g factor. At finite temperatures the levels are populated by the $Z^{-1} \exp(-g\mu_B B M_J / k_B T)$ probability factor, where Z is the partition function and k_B is the Boltzmann factor.

If the spin-orbit interaction is much smaller than the electrostatic interactions, the states are characterized by quantum numbers αLS , where α is a suitable quantity for distinguishing between terms having the same values of the orbital and spin angular momenta L and S .

Two different kind of basis sets, i.e., LS - and jj -coupled wave functions, are commonly used. The electrostatic interaction is diagonal in LS coupling, whereas the spin-orbit interaction is diagonal in jj coupling. In the LS -coupling scheme, the various one-electron orbital momenta ℓ are coupled together successively to give a total orbital momentum, and the various one-electron spin momenta s are coupled to give a total spin

$$(\{(\ell_a s_a) L_a S_a, \ell_b s_b\} L_b S_b, \dots, \ell_n s_n\} L_n S_n) J_n, \quad (12)$$

with triangulation rules such as $L_b = |L_a - \ell_b|, \dots, L_a + \ell_b$, or in short $\Delta(L_b, L_a, \ell)$.

In the other scheme of jj coupling, each ℓ and s are coupled to give a total angular momentum j , and the various j are then coupled to give successive values of J ,

$$\{[(\ell_a s_a j_a) J_a, (\ell_b s_b j_b) J_b, \dots, (\ell_n s_n j_n) J_n]\} J_n. \quad (13)$$

In practice, neither electrostatic nor spin-orbit interactions can be neglected. In this intermediate coupling case, any multielectronic wave function can be written as a linear combination $\psi = \sum_{LSJ} c_{LSJ} \psi_{LSJ} = \sum_{jj'J} c_{jj'J} \psi_{jj'J}$, where c_{LSJ} and $c_{jj'J}$ are wave function coefficients (van der Laan and Thole, 1996).

5. Specific x-ray spectroscopies

In the remainder of this theory section, we give the fundamentals in terms of transition probabilities for the photon-matter interactions of the various x-ray techniques. To create some structure, we use the term expansion in the KH formula, thereby gradually building toward more complexity. We start by describing processes involving first-order absorption [Fig. 4(a)], such as XAS, XMCD, and PES. Thereafter, we progress to first-order scattering [Fig. 4(b)], such as Thomson scattering and NIXS, and finally second-order scattering [Fig. 4(c)], such as REXS and RIXS, which contain an intermediate state and allow for resonant enhancement. However, we do not keep the same order in the experimental part, where we start with techniques that readers are most familiar with, such as XRD, and gradually shift to more “exotic” techniques.

B. X-ray absorption spectroscopy

1. Transition-matrix element

XAS represents an atomic transition from a core level into an unoccupied, discrete state below the continuum. Transitions to states at higher energies are treated in Sec. III.B.5. As the excited electron remains in the solid and is not directly detectable, the XAS is measured either by the x-ray transmission probability or by the decay of the created core holes, which gives fluorescence, Auger, and secondary electron yield (van der Laan and Figueroa, 2014).

The XAS process arises from the $\mathbf{A} \cdot \mathbf{p}$ term in H_{int} , with its transition probability given by the first-order term in Fermi's golden rule as

$$T_{gf} = \frac{2\pi}{\hbar} |\langle f | \mathbf{A} \cdot \mathbf{p} | g \rangle|^2 \delta(E_g - E_f + \hbar\omega). \quad (14)$$

The matrix element $\langle f | \mathbf{A} \cdot \mathbf{p} | g \rangle$ can also be featured as the initial step in second-order processes, which makes it rewarding to examine its properties. Converting it to the length form using the commutator between the position vector \mathbf{r} of an electron and the Hamiltonian of the unperturbed atom H ,

$$\mathbf{p} \equiv -i\hbar\nabla = \frac{m}{i\hbar} [\mathbf{r}, H], \quad (15)$$

and using the annihilation part of the vector potential $\mathbf{A}(\mathbf{k}, \mathbf{r}) = \mathbf{e} e^{i\mathbf{k} \cdot \mathbf{r}}$ gives

$$\langle f | \mathbf{A} \cdot \mathbf{p} | g \rangle = \frac{m}{i\hbar} (E_f - E_g) \langle f | (\mathbf{e} \cdot \mathbf{r}) e^{i\mathbf{k} \cdot \mathbf{r}} | g \rangle. \quad (16)$$

Next we show how to factorize the scalar operator $\mathbf{A} \cdot \mathbf{p} \sim (\mathbf{e} \cdot \mathbf{r}) e^{i\mathbf{k} \cdot \mathbf{r}}$ in the matrix element. The transition operator can be factorized into a part that depends only on the geometry of the experiment (which is commonly called the *photon part*, or sometimes the geometrical or angular factor) and another part that depends only on the material properties (which is commonly called the *matter part*, or sometimes the dynamic or physical factor). For simplicity we assume spherical symmetry and neglect crystal-field interaction. This gives us a proper way to assign the different multipole moments of the electromagnetic radiation field. Furthermore, it offers a first glance on the rather powerful method of moment recoupling, which is usually done using spherical tensor algebra (van der Laan, 2006).

Cartesian and spherical components of a dipole $\mathbf{r} = (x, y, z)$ are related by $r_{\pm 1} = \mp (x \pm iy)/\sqrt{2}$, $r_0 = z$. Cartesian tensors are conceptually more simple and are closely related to the natural coordinate system of the crystal but become unwieldy for higher multipole moments. Spherical tensors are irreducible and follow general rules of angular momentum algebra (Edmonds, 1957). In both formulations, the aim is to separate the cross section into a matter part and a geometric part. While the resonant amplitude of the matter part requires detailed knowledge of the electronic wave function, the geometric part can be factored out. This also allows us to handle the polarization and angular part of the matrix elements.

Spherical tensors can be coupled using the tensor coupling theorem

$$[C^{(z')}, C^{(z'')}]_{\zeta}^{(z)} \equiv \sum_{\zeta', \zeta''} C_{\zeta'}^{(z')} C_{\zeta''}^{(z'')} C_{\zeta}^{z' z'' z}, \quad (17)$$

where $C_{\zeta}^{(z)} = \sqrt{4\pi/(2z+1)} Y_{\zeta}^{(z)}$ is the renormalized spherical harmonic and $C_{z' z'' z}^{z' z'' z} = \langle z' \zeta', z'' \zeta'' | z \zeta \rangle$ is the Clebsch-Gordan coefficient.

For $\mathbf{k} \cdot \mathbf{r} \ll 1$, the exponential factor in the vector potential \mathbf{A} can be expanded as

$$e^{i\mathbf{k} \cdot \mathbf{r}} = \sum_{L=0}^{\infty} \frac{(i\mathbf{k} \cdot \mathbf{r})^L}{L!} = 1 + i\mathbf{k} \cdot \mathbf{r} - \frac{1}{2} (\mathbf{k} \cdot \mathbf{r})^2 + \dots, \quad (18)$$

and using the tensor coupling theorem of Eq. (17) we can decompose the transition operator into multipole moments of rank z , which couple to a scalar product,

$$\begin{aligned} (\mathbf{e} \cdot \mathbf{p}) e^{i\mathbf{k} \cdot \mathbf{r}} &\propto i^L \sum_{z=L}^{\infty} \sum_{\zeta=-z}^{L+1} \sum_{\zeta=-z}^{+z} [[\mathbf{e}, \mathbf{k}]_{-\zeta}^{(L)}]^{(z)} [\mathbf{p}, \mathbf{r}]_{\zeta}^{(L)}]_{\zeta}^{(z)}]_0^{(0)} \\ &= \mathbf{e} \cdot \mathbf{p} + i \sum_{z=1}^2 \sum_{\zeta=-z}^{+z} [[\mathbf{e}, \mathbf{k}]_{-\zeta}^{(z)}]^{(z)} [\mathbf{p}, \mathbf{r}]_{\zeta}^{(z)}]_0^{(0)} + \dots \end{aligned} \quad (19)$$

Thus, this gives a sum over products of tensors of rank z for a geometric factor containing \mathbf{e} and \mathbf{k} , and a dynamic factor containing \mathbf{p} and \mathbf{r} . On the last line of Eq. (19) we retain only the terms $L = 0$ and 1, which are discussed next.

The $L = 0$ term is $\boldsymbol{\varepsilon} \cdot \mathbf{p} \propto \boldsymbol{\omega} \boldsymbol{\varepsilon} \cdot \mathbf{r}$ and corresponds to the electric-dipole ($E1$) term. Both the geometrical factor $\boldsymbol{\varepsilon}$ and the dynamic factor \mathbf{r} are time even and parity odd, so the matrix element $\langle f | \mathbf{r} | g \rangle$ is nonzero only if the initial and final states have opposite parities.

The $L = 1$ term factorizes into a geometric factor $[\boldsymbol{\varepsilon}, \mathbf{k}]^{(z)}$ and a dynamic factor $[\mathbf{p}, \mathbf{r}]^{(z)}$, which are parity even. For $z = 0$, the geometric factor vanishes due to transversality ($\boldsymbol{\varepsilon} \cdot \mathbf{k} = 0$). The $z = 1$ term gives the magnetic-dipole ($M1$) contribution with a geometric factor $[\boldsymbol{\varepsilon}, \mathbf{k}]^{(1)} \propto \mathbf{k} \times \boldsymbol{\varepsilon}$ and a dynamic factor $[\mathbf{p}, \mathbf{r}]^{(1)} \propto \mathbf{p} \times \mathbf{r} \propto \mathbf{L}$, the orbital momentum operator, which is time odd. The $z = 2$ term gives the electric-quadrupole ($E2$) term, with dynamic factor $[\mathbf{p}, \mathbf{r}]^{(2)} \propto \mathbf{L}^{(2)} \propto$ (the charge quadrupole), which is time even.

Thus, the leading terms in the transition amplitude can be written as (Hill and McMorro, 1996)

$$-\frac{m}{\hbar}(E_f - E_g) \left[\langle f | \boldsymbol{\varepsilon} \cdot \mathbf{r} | g \rangle + \frac{i}{2} \langle f | (\boldsymbol{\varepsilon} \cdot \mathbf{r})(\mathbf{k} \cdot \mathbf{r}) | g \rangle \right] - \langle f | (\mathbf{k} \times \boldsymbol{\varepsilon}) \cdot (\mathbf{L} + g\mathbf{S}) | g \rangle + \dots, \quad (20)$$

where the first, second, and third terms correspond to the $E1$, $E2$, and $M1$ transition-matrix elements, respectively. The $E1$ transition is parity odd, whereas $M1$ and $E2$ are parity even. The $E2$ and $M1$ transition probabilities are $(\alpha Z_{\text{eff}})^2$ times smaller than that of $E1$, where α is the fine-structure constant $e^2/\hbar c \approx 1/137$.

Expressions for the geometric and dynamical parts of electric- and magnetic-multipole transitions of arbitrary rank were given by van der Laan (2006). In essence, the L term with parity $(-)^{L+1}$ separates into a magnetic 2^L pole with dynamic factor $[\mathbf{p}, \mathbf{r}]^{(L)}$ and an electric $2^{(L+1)}$ pole with dynamic factor $[\mathbf{p}, \mathbf{r}]^{(L+1)}$. The exception is $L = 0$ since there is no magnetic monopole.

The magnetic-dipole operator does not incorporate the radial variable \mathbf{r} , so its matrix elements vanish if the radial part of the initial and final states are orthogonal. In the LS coupling scheme, the one-electron magnetic-dipole transition rules are $|\Delta j| \leq 1$, $\Delta \ell = 0$, $\Delta s = 0$, and $\Delta n = 0$ (identical principal quantum numbers). This means that magnetic-dipole absorption is relevant only at low energy (typically in the microwave and optical ranges). Its observation at higher energy implicates an appreciable configuration interaction between the initial and final states due to a departure from a pure LS coupling. However, such a configuration interaction is negligible in core-level spectroscopy because of the large energy difference between the initial and final states. Nevertheless, $E1$ - $M1$ absorption in UV spectroscopy is a standard tool for characterizing chiral molecules.

The electric-multipole transition operator with $z = L + 1$ is proportional to

$$\sum_{\Delta z} \left[C^{(1)}(\boldsymbol{\varepsilon}), C^{(z-1)}(\mathbf{k}) \right]_{-\Delta z}^{(z)}, C_{\Delta z}^{(z)}(\mathbf{r}) \Big]_0^{(0)}, \quad (21)$$

where the factor $C_{\Delta z}^{(z)}(\mathbf{r})$ of the matter part gives the spectra $I_{\Delta z}^{(z)}(\omega)$. For instance, for the electric-dipole transition

($z = 1$), where the \mathbf{k} dependence is absent, the transition operator is

$$\boldsymbol{\varepsilon} \cdot \mathbf{r} = \sum_{j=x,y,z} \varepsilon_j r_j = r \sum_{\zeta=-1,0,1} C_{\zeta}^{(1)*}(\boldsymbol{\varepsilon}) C_{\zeta}^{(1)}(\mathbf{r}), \quad (22)$$

where $C_{\zeta}^{(1)*} = C_{-\zeta}^{(1)}$.

The electric 2^z -pole matrix elements with components ζ for a transition operator $T_{\zeta}^{(z)}$ from a core state $|\alpha' c \gamma\rangle$ to an empty valence state $|\alpha \ell m\rangle$ are, according to the Wigner-Eckart theorem, proportional to the $3j$ symbol times the reduced matrix element

$$I_{\zeta}^{(z)}(\omega) \propto \langle \alpha' c \gamma | T_{\zeta}^{(z)} | \alpha \ell m \rangle = (-1)^{c-\gamma} \begin{pmatrix} c & z & \ell \\ -\gamma & \zeta & m \end{pmatrix} \times \langle \alpha' c || T^{(z)} || \alpha \ell \rangle, \quad (23)$$

where the $3j$ symbol (or Wigner coefficient), denoted by the parentheses, is related to the Clebsch-Gordan coefficient as

$$\langle c \gamma z \zeta | \ell m \rangle = (-1)^{c+\zeta+m} \sqrt{2\ell+1} \begin{pmatrix} c & z & \ell \\ -\gamma & \zeta & m \end{pmatrix}. \quad (24)$$

The $3j$ symbol is zero unless the following conditions are satisfied: $c + z + \ell$ is an integer (integer perimeter rule) or an even integer if $\gamma = \zeta = m = 0$ (parity rule), $|c - \ell| \leq z \leq |c + \ell|$ [triangular inequality $\Delta(cz\ell)$], and $-\gamma + \zeta + m = 0$ (rotational invariance). We immediately recognize these physically relevant conditions as the selection rules for optical transitions. The reduced matrix element $\langle \alpha' c || T^{(z)} || \alpha \ell \rangle$ is responsible for the parity rule $c + z + \ell = \text{even}$.

Similar selection rules apply for the matrix elements in the multipole transition $\alpha J M \rightarrow \alpha' J' M'$ for jj -coupled states

$$\langle \alpha' J' M' | T_{\zeta}^{(z)} | \alpha J M \rangle = (-1)^{J'-M'} \begin{pmatrix} J' & z & J \\ -M' & \zeta & M \end{pmatrix} \times \langle \alpha' J' || T^{(z)} || \alpha J \rangle, \quad (25)$$

where the conservation of angular momentum is contained in the $3j$ symbol as $\Delta(J'zJ)$ and $M' = M + \zeta$.

2. Sum rules

The polarization dependence of XAS is one of its greatest assets, making it sensitive to charge anisotropy and spin and orbital magnetism (Thole *et al.*, 1992; Carra *et al.*, 1993; van der Laan, 1998b). Starting from the electric-dipole spectra $I_{\zeta} \equiv I_{\zeta}^{(1)}$ for left-circular ($\zeta = -1$), right-circular ($\zeta = +1$), and linear polarization along the beam direction ($\zeta = 0$), we can make new linear combinations of the so-called fundamental spectra I^x , where x is the angular momentum transferred from the photon to the atom. This gives the isotropic spectrum $I^0 = I_{-1} + I_0 + I_{+1}$, the XMCD (the difference between the left- and right-circular polarization $I^1 = I_{-1} - I_{+1}$ and the x-ray linear dichroism $I^2 = I_{-1} - 2I_0 + I_{+1}$).

The spectra I^0 , I^1 , and I^2 provide sum rules that relate the energy-integrated intensities $\rho^x = \int I^x dE$ over the spin-orbit-separated regions of the core-level spectrum with the

expectation values of the ground-state moments. For a deep core level, the large spin-orbit interaction splits the spectrum into two separate manifolds with good quantum numbers $j_{\pm} = \ell \pm s$. For example, the core $3d \rightarrow 5f$ transition gives rise to a multiplet spectrum $3d^{10}5f^n \rightarrow 3d^95f^{n+1}$, which splits into $3d_{5/2}$ and $3d_{3/2}$ manifolds (M_5 and M_4 edges for uranium at ~ 3552 and 3728 eV, respectively). The sum rules for this excitation are the same as they are for $4d \rightarrow 5f$ ($N_{5,4}$ edges for U at ~ 736 and 778 eV). However, in the case of $5d \rightarrow 5f$ ($O_{5,4}$ edges for U at ~ 94 and 103 eV) the core spin-orbit interaction is not large enough compared to the $5d$ - $5f$ electrostatic interaction to fully separate both edges, leading to jj mixing between the edges and making the spin sum rule inaccurate.

3. Isotropic spectrum

In this section and Sec. III.B.4 we present the expressions of the XAS and XMCD sum rules for the $d^{10}f^n \rightarrow d^9f^{n+1}$ electric-dipole transitions at the $M_{4,5}$ and $N_{4,5}$ absorption edges.

For the isotropic XAS spectrum the integral over the two absorption edges ρ_{j+}^0 and ρ_{j-}^0 is proportional to the number of holes $n_h = 14 - n$ in the $5f$ shell, which can be used to normalize the dichroic sum rules.

The weighted intensity difference between the two edges is proportional to the expectation value of the angular part of the spin-orbit operator $\boldsymbol{\ell} \cdot \mathbf{s}$ (Thole and van der Laan, 1988),

$$\frac{\rho_{j+}^0 - (3/2)\rho_{j-}^0}{\rho_{j+}^0 + \rho_{j-}^0} = \frac{2 \langle \boldsymbol{\ell} \cdot \mathbf{s} \rangle}{3 \langle n_h \rangle}, \quad (26)$$

where

$$\begin{aligned} \langle \boldsymbol{\ell} \cdot \mathbf{s} \rangle &= -2 \langle n_h^{5/2} \rangle + (3/2) \langle n_h^{7/2} \rangle, \\ \langle n_h \rangle &= \langle n_h^{5/2} \rangle + \langle n_h^{7/2} \rangle, \end{aligned} \quad (27)$$

with $\langle n_h^{5/2} \rangle$ and $\langle n_h^{7/2} \rangle$ the number of $j = 5/2$ and $j = 7/2$ holes in the f shell.

Alternatively, we can relate the spin-orbit expectation value to the branching ratio

$$\begin{aligned} B &\equiv \frac{\rho_{j+}^0}{\rho_{j-}^0 + \rho_{j+}^0} = \frac{3}{5} + \frac{4 \langle \boldsymbol{\ell} \cdot \mathbf{s} \rangle}{15 \langle n_h \rangle} \\ &= \frac{3}{5} + \frac{-8 \langle n_h^{5/2} \rangle + 6 \langle n_h^{7/2} \rangle}{15 \langle n_h \rangle}, \end{aligned} \quad (28)$$

where the fraction $3/5$ is the statistical ratio for B in the absence of a spin-orbit interaction.

4. X-ray magnetic circular dichroism

For the XMCD the integral over both edges is proportional to the expectation value of the orbital moment L_z . For the $d \rightarrow f$ transition we have

$$\frac{\rho_{j+}^1 + \rho_{j-}^1}{\rho_{j+}^0 + \rho_{j-}^0} = \frac{1}{3} \frac{\langle L_z \rangle}{n_h}. \quad (29)$$

The weighted difference over the core spin-orbit-split intensities is proportional to the ground-state expectation value of the effective spin moment $S_{z,\text{eff}}$, which comprises the spin moment S_z and the magnetic-dipole term $\mathbf{T} = \sum_i \mathbf{s}_i - 3\mathbf{r}_i(\mathbf{r}_i \cdot \mathbf{s}_i)$,

$$\frac{\rho_{j+}^1 - (3/2)\rho_{j-}^1}{\rho_{j+}^0 + \rho_{j-}^0} = \frac{2 \langle S_{z,\text{eff}} \rangle}{3 n_h} = \frac{2 \langle S_z \rangle + 3 \langle T_z \rangle}{3 n_h}. \quad (30)$$

While the spin moment \mathbf{S} is isotropic, \mathbf{T} gives the anisotropy of the spin moment due to the coupling with the charge quadrupole moment.

The number of f holes ($n_h = 14 - n$) is often known in the case of the more localized rare earths (Thole *et al.*, 1985), but this is usually not so for the actinides (Moore and van der Laan, 2009). The number of holes cancels out in the orbital-to-spin moment ratio,

$$\frac{\langle L_z \rangle}{\langle S_{z,\text{eff}} \rangle} = 2 \frac{\rho_{j+}^1 + \rho_{j-}^1}{\rho_{j+}^1 - (3/2)\rho_{j-}^1}. \quad (31)$$

Further, there are sum rules for the x-ray magnetic linear dichroism relating the integrated intensities to the charge anisotropy and the anisotropic part of the spin-orbit interaction of the f electrons (van der Laan, 1999).

5. X-ray absorption fine structure

Thus far we have looked at transitions into the localized $5f$ states. We now consider transitions to states at higher energies. In the solid, the core-level absorption spectrum can be separated into transitions to bound (discrete) final states and continuum states below and above the ionization potential due to excitations of the photoelectron in the vacuum. While the naming of these regions is a matter of taste, it makes sense to classify them according to the applicable theoretical models. In the case of atomlike transitions, the onset of the edge shows an intense multiplet structure that we call XAS. The region with excitations to continuum states can be divided into the XANES and EXAFS at respective higher energies above the edge. The XANES region gives information about the electronic structure of the binding electrons and is often calculated using multiple scattering theory. In the EXAFS region, the core electron is excited into a continuum state that still feels the potential of the neighboring atoms. The interference of the outgoing and backscattered electron waves by the neighboring atoms depends on the wave nature of the photoelectron and is particularly sensitive to the radial distances of the various shells of neighboring atoms around the absorbing one. It is convenient to think of the XAFS in terms of the photoelectron wave number, $k = \sqrt{2m(E - E_0)}/\hbar$, where E_0 is the threshold absorption energy (Lytle, 1999).

The modulation of the x-ray absorption coefficient $\mu(E) \sim |f|H|g|^2$ at energies near and above an x-ray absorption edge is captured by the EXAFS equation (Stöhr, 1992)

$$\chi(E) \equiv \frac{\mu(E) - \mu_0(E)}{\Delta\mu_0(E)} = \sum_j \frac{N_j f_j(k) e^{-2k^2 \sigma_j^2}}{k R_j^2} \sin[2kR_j + \delta_j(k)], \quad (32)$$

where $\mu_0(E)$ is a smooth background function representing the absorption of the isolated atom, and $\Delta\mu_0(E)$ is the measured jump in the absorption $\mu(E)$ at the threshold energy E_0 .

The sum is over “shells” of similar neighboring atoms with coordination number N , distance R , and mean-square disorder σ^2 . The scattering amplitude $f(k)$ and phase shift $\delta(k)$ depend on the atomic number Z of the scattering atom, which can be used to determine the species of the neighboring atoms.

C. X-ray photoelectron spectroscopy

1. Core-level photoemission

Photoelectron emission spectroscopy is well established as a popular method to study the electronic structure of materials. Owing to the small electron elastic escape depth, PES is rather surface sensitive, so good vacuum conditions are needed to conduct measurements of a prepared surface. The photoelectron inelastic mean free path varies as a function of kinetic energy with a minimum at around 40 eV. Bulk sensitivity is acquired at high photon energy, but at the cost of a reduced cross section and, often, reduced energy resolution. One distinguishes between x-ray photoelectron spectroscopy (XPS) and ultraviolet photoelectron spectroscopy (UPS) when using soft x rays and ultraviolet radiation, respectively. XPS is performed primarily with Al or Mg $K\alpha$ radiation from a laboratory x-ray source or monochromatized radiation from the synchrotron; UPS is performed mainly using a He-I or He-II gas discharge lamp in the laboratory. A benefit of the different photon energies, especially when using tunable SR, is that it gives different relative cross sections of the transitions involved, thereby providing a way to distinguish between them. PES is also performed in an angle-resolved fashion using single-crystal samples, or at resonance using x-ray energies that coincide with a core-valence excitation (Terry *et al.*, 2002).

In the PES process, a photon $h\nu$ is absorbed under emission of an electron with kinetic energy E_{kin} . Energy conservation requires that $E_{\text{kin}} = h\nu + E_N - E_{N-1}$, where E_N and E_{N-1} are the energies of the N -electron initial state and the $(N-1)$ -electron final state. The energy $E_B = h\nu - E_{\text{kin}} = E_{N-1} - E_N$ is usually called the electron binding energy; however, it would be better to call this the electron removal energy. Only when the electrons do not feel each other, PES gives the one-electron DOS. However, in correlated materials, such as many of the actinide metals, PES should be regarded as a probe of the many-electron state.

In contrast to XAS, where the excited electron goes into an unoccupied valence state, in PES it goes into a continuum state and reaches a detector that analyses its kinetic energy. The ionization has major implications for the screening of the photoexcited hole. Thus, in the actinide atom the valence and core PES can be represented by the transitions $5f^n \rightarrow 5f^{n-1}e$

and $5f^n \rightarrow \underline{c}5f^n e$, respectively, where e is a continuum state far above the Fermi level and \underline{c} denotes a core hole. In the so-called sudden approximation, one assumes that the excited photoelectron has no interaction with the state left behind so that in the calculation the photoelectron state can be decoupled from the atomic state. The PE spectrum is expressed as a function of binding energy as

$$I(E_B) = \sum_{nmm'\sigma\sigma'} |\langle f_n | \epsilon_{m'\sigma'}^\dagger c_{m\sigma} | g \rangle|^2 \delta_{\sigma,\sigma'} \delta(E_B + E_g - E_{f_n}), \quad (33)$$

where the ground and final states $|g\rangle$ and $|f_n\rangle$ have energies E_g and E_{f_n} , respectively. $c_{m\sigma}$ is the annihilation operator of an electron c with quantum numbers m and σ , and $\epsilon_{m'\sigma'}^\dagger$ is the creation operator of a continuum electron e with quantum numbers m' and σ' . The $5f$ PES of actinide atoms displays an intense multiplet structure, which was calculated for intermediate coupling by Gerken and Schmidt-May (1983).

In contrast to XAS, core-level PES is well suited to determine the hybridization between the valence electrons (van der Laan *et al.*, 1986). In XAS the core electron is excited into an unoccupied f state, thus effectively screening the core hole. The potential energy change is $U_{ff} - Q_{cf}$, where U_{ff} is the Coulomb interaction between two f electrons and Q_{cf} is the Coulomb interaction between the core and the f electron. If $U_{ff} \approx Q_{cf}$, as is roughly the case, the change in hybridization (mixing) between the initial and final states is small. In PES the core electron is excited into the continuum, leaving the core hole unscreened. The potential energy change is $-Q_{cf}$. Hence, the change in hybridization in the final state is large and can be used to determine the hybridization in the initial state, as demonstrated for the example of Pu $4f$ core-level PES in Sec. X.A.

2. Angle-resolved PES

At low photon energies, which are typically used in angle-resolved photoemission spectroscopy (ARPES), the photon momentum can be neglected. Taking advantage of the total energy and momentum conservation laws, one can relate the kinetic energy and momentum of the photoelectron to the binding energy E_B and crystal momentum $\hbar\mathbf{k}$ inside the solid.

The PE is measured as a function of kinetic energy $E_{\text{kin}} = \hbar\omega - E_B - \phi$ and angle ϑ relative to the surface normal, where ϕ is the work function of the material. The Bloch wave vector \mathbf{k} can be linked to the measured electron momentum $|\mathbf{p}| = \sqrt{2m_e E_{\text{kin}}}$ such that

$$\begin{aligned} \mathbf{p}_{\parallel} &= \hbar\mathbf{k}_{\parallel} = \sqrt{2m_e E_{\text{kin}}} \sin \vartheta, \\ \mathbf{p}_{\perp} &= \hbar\mathbf{k}_{\perp} = \sqrt{2m_e (E_{\text{kin}} \cos^2 \vartheta + V_0)}, \end{aligned} \quad (34)$$

where $\hbar\mathbf{k}_{\parallel}$ and $\hbar\mathbf{k}_{\perp}$ are the components parallel and normal to the surface, respectively, and the inner potential V_0 is an *a priori* unknown parameter. Upon going to larger angles ϑ , one actually probes electrons with \mathbf{k} in higher-order Brillouin zones. By subtracting the corresponding reciprocal lattice vector \mathbf{G} , one obtains the reduced electron crystal momentum in the first Brillouin zone.

3. Resonant PES

In the t -matrix approach the transition probability for RPES is determined by an operator (van der Laan *et al.*, 1999)

$$T = D + VGT = D + VGD + VGVGT = \sum_{n=0}^{\infty} (VG)^n D, \quad (35)$$

which is first order in the dipole operator D and infinite order in the Coulomb decay operator V . The Green's function is $G = 1/(H - h\nu - E_g - i\eta)$, where H is the unperturbed Hamiltonian and η is a small positive number; see Eq. (10). For ζ -polarized light, the probability for the angle-integrated photoemission in resonance with a core level can be expressed as

$$\begin{aligned} I_{\zeta}(h\nu, E_B) &= |\langle f | T_{\zeta} | g \rangle|^2 \delta(E_g - E_f + h\nu) \\ &= \sum_f \left| \langle f | D_{\zeta} | g \rangle + \sum_n \frac{\langle f | V | n \rangle \langle n | D_{\zeta} | g \rangle}{E_n - E_g - h\nu - i\Gamma_n/2} + \dots \right|^2 \\ &\quad \times \delta(E_g - E_f + h\nu), \end{aligned} \quad (36)$$

with the decay full width

$$\Gamma_n = 2\pi |\langle f | V | n \rangle|^2. \quad (37)$$

For instance, for the $4d \rightarrow 5f$ resonant photoemission, $|g\rangle$, $|n\rangle$, and $|f\rangle$ are the eigenstates in the transition $5f^{N+} + h\nu \rightarrow 4d^9 5f^{N+1} \rightarrow 5f^{N-1} + e$. Equation (36) may serve to illustrate the different ways to reach the final state, i.e., direct photoemission from the initial to the final state, photoexcitation into an intermediate state followed by decay into the final state, and the coherent superposition of these processes.

D. Nonresonant scattering

At incident photon energies far from resonant excitation, the double differential cross section (DDCS) for x-ray scattering is obtained from the KH formula at first order in \mathbf{A}^2 [Fig. 4(b)], with a vector potential $\mathbf{A}(\mathbf{k}, \mathbf{r}) = \boldsymbol{\epsilon} e^{i\mathbf{k}\cdot\mathbf{r}}$, as

$$\begin{aligned} \frac{d^2\sigma}{d\Omega d\omega} &= r_0^2 \frac{\omega_{\mathbf{k}'}}{\omega_{\mathbf{k}}} (\boldsymbol{\epsilon}'^* \cdot \boldsymbol{\epsilon})^2 \sum_f \left| \langle f | \sum_j e^{i(\mathbf{k}-\mathbf{k}')\cdot\mathbf{r}_j} | g \rangle \right|^2 \\ &\quad \times \delta(E_g - E_f + \hbar\omega_{\mathbf{k}} - \hbar\omega_{\mathbf{k}'}). \end{aligned} \quad (38)$$

Defining the photon momentum transfer (or scattering vector) $\mathbf{Q} \equiv \mathbf{k} - \mathbf{k}'$ leads to a factor $e^{i\mathbf{Q}\cdot\mathbf{r}_j}$ in Eq. (38).

1. Thomson scattering

The previously introduced Thomson scattering is the elastic scattering of an electromagnetic wave from charged particles due to \mathbf{A}^2 . Whereas this falls more in the domain of conventional x-ray diffraction using cathode ray tubes, it is discussed here for completeness.

As Thomson scattering is elastic, $\omega_{\mathbf{k}'} = \omega_{\mathbf{k}}$ and $|f\rangle = |g\rangle$, which leads us to Eq. (9). The scattering cross section in a crystal can be written as

$$\frac{d\sigma}{d\Omega} = r_0^2 (\boldsymbol{\epsilon}'^* \cdot \boldsymbol{\epsilon})^2 |F(\mathbf{Q})|^2 = r_0^2 (\boldsymbol{\epsilon}'^* \cdot \boldsymbol{\epsilon})^2 \left| \sum_j e^{i\mathbf{Q}\cdot\mathbf{r}_j} f_j(\mathbf{Q}) \right|^2, \quad (39)$$

where $f_j(\mathbf{Q})$ is the atomic form factor. When energy dispersion corrections are neglected, $f_j(\mathbf{Q})$ is a real number given by the Fourier transform of the charge distribution in the j th atom; the sum is over the n atoms of the unit cell basis, and \mathbf{Q} is equal to a reciprocal lattice vector \mathbf{G} .

The unit cell structure factor $F(\mathbf{Q}) = \sum_j f_j e^{i\mathbf{Q}\cdot\mathbf{r}_j}$ takes into account the phase factor that arises from the path difference of the x rays between the atoms. $F(\mathbf{Q})$ is generally complex, although it is purely real in centrosymmetric crystals with a suitable choice of origin (again, if dispersion corrections are negligible; see Sec. III.E.1). Away from resonance, the charge scattering becomes an integral over the continuous electron density $\rho(\mathbf{r})$ as $F(\mathbf{Q}) = \int d\mathbf{r} e^{i\mathbf{Q}\cdot\mathbf{r}} \rho(\mathbf{r})$.

Since the scattering cross section in Eq. (39) is related to the absolute square of the Fourier transform of the electron density at momentum \mathbf{Q} , the phase information is lost in the measurement. This is known as the phase problem.

2. Nonresonant inelastic x-ray scattering

NIXS is a photon-in, photon-out process, which is a direct transition not involving an intermediate state. Compared to XAS, the main benefit of NIXS is that it gives us access to higher multipole transitions; the main disadvantage is, as for all nonresonant techniques, the low cross section and the required narrow bandwidth optics that make measurements challenging (Schülke, 2007; Caciuffo, van der Laan *et al.*, 2010; van der Laan, 2012a).

Reshuffling the DDCS in Eq. (38), the Thomson differential scattering cross section $(d\sigma/d\Omega)_{\text{Th}}$ can be factored out so that the technique measures a target excitation structure known as the dynamical structure factor, $S(\mathbf{Q}, \omega)$, which is independent of the specific experimental geometry,

$$\frac{d^2\sigma}{d\Omega d\omega} = \left(\frac{d\sigma}{d\Omega} \right)_{\text{Th}} S(\mathbf{Q}, \omega), \quad (40)$$

with

$$S(\mathbf{Q}, \omega) = \sum_f \left| \langle f | \sum_j e^{i\mathbf{Q}\cdot\mathbf{r}_j} | g \rangle \right|^2 \delta(E_g - E_f + \hbar\omega) \quad (41)$$

and

$$\left(\frac{d\sigma}{d\Omega} \right)_{\text{Th}} = r_0^2 \frac{\omega_{\mathbf{k}'}}{\omega_{\mathbf{k}}} (\boldsymbol{\epsilon}'^* \cdot \boldsymbol{\epsilon})^2, \quad (42)$$

where $\hbar\omega = \hbar\omega_{\mathbf{k}} - \hbar\omega_{\mathbf{k}'}$ is the energy transfer and $d\Omega$ is the solid angle element of the scattered photons.

The dynamical structure factor $S(\mathbf{Q}, \omega)$ in Eq. (41) can be related to a density-density correlation function in the space and time of the system (Van Hove, 1954),

$$S(\mathbf{Q}, \omega) = \int d\mathbf{r} dt e^{i(\mathbf{Q}\cdot\mathbf{r} - \omega t)} \int d\mathbf{r}' \langle g | \rho(\mathbf{r}', 0) \rho(\mathbf{r} + \mathbf{r}', t) | g \rangle. \quad (43)$$

This means that the inelastic analog of the Thomson scattering permits one to study the spectrum of charge-density fluctuations, such as phonons, electronic excitations, and plasmons.

The transition operator $e^{i\mathbf{Q}\cdot\mathbf{r}}$ in Eq. (41) can be expanded as a sum over scalar products of spherical multipole tensors with rank k and components $\kappa = -k, \dots, k$ as

$$e^{i\mathbf{Q}\cdot\mathbf{r}} = \sum_{k=0}^{\infty} \sum_{\kappa=-k}^k i^k (2k+1) j_k(Qr) C_{\kappa}^{(k)*}(\mathbf{Q}) C_{\kappa}^{(k)}(\mathbf{r}), \quad (44)$$

where $j_k(Qr)$ are spherical Bessel functions of rank k and $C_{\kappa}^{(k)}(\mathbf{r})$ are renormalized spherical harmonics.

Assuming spherical symmetry, the interference terms ($k \neq k'$, where k' is the rank of the conjugated multipole) vanish. Taking the radial-matrix elements as constant over the spectral region of interest, $S(\mathbf{Q}, \omega)$ [Eq. (41)] can be separated into an angular and a radial part:

$$S(\mathbf{Q}, \omega) = \sum_{k=0}^{\infty} I^k(\omega) |\langle f | j_k(Qr) | g \rangle|^2. \quad (45)$$

The angular part of the isotropic 2^k -pole spectrum is

$$I^k(\omega) = \sum_{f,\kappa} |\langle f | C_{\kappa}^{(k)}(\mathbf{r}) | g \rangle|^2 \delta(E_g - E_f + \hbar\omega). \quad (46)$$

Multipole moments k for the $\ell \rightarrow \ell'$ transition are restricted by the triangle condition $|\ell - \ell'| \leq k \leq \ell + \ell'$ and the parity rule $\ell + \ell' + k = \text{even}$. Thus, for $d \rightarrow f$ transitions, $k = 1$ (dipole), $k = 3$ (octupole), and $k = 5$ (triakontadipole) transitions are allowed.

At low momentum transfer ($Q \rightarrow 0$) the radial matrix elements $|\langle f | j_k(Qr) | g \rangle|$ are negligible for $k > 1$ and only dipole transitions are important, similar to the case of soft XAS. On the other hand, for large enough Q values (larger than $\sim 9 \text{ \AA}^{-1}$ at the uranium $O_{4,5}$ edges) $|\langle f | j_0(Qr) | g \rangle|$ vanishes and the spectra are dominated by the $k = 3$ and 5 contributions.

In the dipole approximation the NIXS spectrum for $f^n + \hbar\omega_{\mathbf{k}} \rightarrow d^9 f^{n+1} + \hbar\omega_{\mathbf{k}'}$ is the same as the XAS spectrum for $f^n + \hbar\omega \rightarrow d^9 f^{n+1}$. Also in the dipole approximation $\hat{\mathbf{Q}} = \mathbf{Q}/Q$ plays in NIXS the same role as $\boldsymbol{\varepsilon}$ in XAS. However, note that $\hat{\mathbf{Q}}$ is a polar vector allowing only Hermitian matrix elements, whereas $\boldsymbol{\varepsilon}$ is an axial vector, allowing anti-Hermitian matrix elements and hence enabling XMCD, making the latter a supreme tool for magnetism (van der Laan and Figuera, 2014).

In contrast to XAS, it is easy in NIXS to reach the range $Qa \geq 1$, where a is the atomic radius, enabling one to reach dipole-forbidden transitions with high probability by increasing the scattering angle θ , and thereby shifting Q .

The reason that XAS and NIXS give the same spectra, despite different transition-matrix elements, is provided by the

concept of the fundamental spectra, where the angular part of the transition probability is separated from the radial and geometrical parts. A requirement for this is that the radial part remains constant over the spectral range, which is usually fulfilled.

3. Generalized spin-orbit sum rule

The spin-orbit sum rule for XAS given in Eq. (28) can be expanded to the case of NIXS. According to this sum rule, the initial-state spin-orbit interaction per hole is linearly related to the core-level branching ratio.

For the 2^k -multipole transition $d \rightarrow f$ we obtain the branching ratio of the core spin-orbit split levels as (van der Laan, 2012b)

$$B^k = \frac{3}{5} + \frac{18 - k(k+1)}{60} \frac{\langle \boldsymbol{\ell} \cdot \mathbf{s} \rangle}{\langle n_h \rangle} \\ = \frac{3}{5} + [18 - k(k+1)] \frac{-4\langle n_h^{5/2} \rangle + 3\langle n_h^{7/2} \rangle}{120\langle n_h \rangle}, \quad (47)$$

which generalizes the spin-orbit sum rule in Eq. (28). Thus, the various multipole moments k have strongly different values of B^k . For a $f_{7/2}$ hole we have $B^1 = 1$ since the excitation $d_{3/2} \rightarrow f_{7/2}$ is forbidden for dipole transitions. However, this transition is allowed for higher multipole moments, for which $B^3 = 3/4$ and $B^5 = 3/10$. For a $f_{5/2}$ hole we find $B^1 = 1/15$, $B^3 = 2/5$, and $B^5 = 1$. Equation (47) is useful for the actinide $M_{4,5}$ and $N_{4,5}$ edges, which, however, have low NIXS cross sections. Although for the $O_{4,5}$ edges the jj mixing is too large to separate the individual $5d_{3/2}$ and $5d_{5/2}$ edges, the spin-orbit sum rule is still useful since it gives a large intensity transfer to higher energy as $\langle \boldsymbol{\ell} \cdot \mathbf{s} \rangle$ reduces. For the ground state with the lowest spin-orbit energy, higher k spectra have a lower branching ratio. Hence, in the low-energy region the overall intensity of the $k = 3$ spectrum is higher than that of the $k = 5$ spectrum, whereas this is the opposite in the high-energy region.

4. Nonresonant magnetic scattering

Nonresonant magnetic scattering provides a direct method of distinguishing spin and orbital magnetic moments for long-range magnetic structures (Blume, 1985; Blume and Gibbs, 1988). Pioneering experimental studies were published by de Bergevin and Brunel (1981).

A pure spin contribution to the magnetic scattering is obtained by the term $H'_4 \sim \partial \mathbf{A} / \partial t \cdot (e/c) \mathbf{A}$ in the interaction Hamiltonian. On the other hand, an orbital contribution arises mainly from the term $\mathbf{A} \cdot \mathbf{p}$ at second order. The scattering amplitude can be written as

$$f^{\text{mag}} = -i \frac{\hbar\omega_{\mathbf{k}}}{mc^2} \langle g | \sum_j e^{i\mathbf{Q}\cdot\mathbf{r}_j} \left[\frac{i\mathbf{Q} \times \mathbf{p}_j}{\hbar k^2} \cdot \mathbf{P}_L - \mathbf{s}_j \cdot \mathbf{P}_S \right] | g \rangle, \quad (48)$$

with the polarization factors related to the orbital and spin moments

$$\mathbf{P}_L = \boldsymbol{\varepsilon}^{*k} \times \boldsymbol{\varepsilon}, \quad (49)$$

$$\mathbf{P}_S = (\boldsymbol{\epsilon}'^* \times \boldsymbol{\epsilon}) + (\mathbf{k}' \times \boldsymbol{\epsilon}'^*)(\mathbf{k}' \cdot \boldsymbol{\epsilon}) - (\mathbf{k} \times \boldsymbol{\epsilon})(\mathbf{k} \cdot \boldsymbol{\epsilon}'^*) - (\mathbf{k}' \times \boldsymbol{\epsilon}'^*) \times (\mathbf{k} \times \boldsymbol{\epsilon}). \quad (50)$$

The cross section of the magnetic scattering is $\hbar^2 \omega_k^2 / m^2 c^4$ times smaller than that of the charge scattering, which amounts to a factor 4×10^{-4} at 10 keV incident photon energy. However, the interference term between the two amplitudes can be used to extract the magnetic cross section.

We define the microscopic electric current density operator

$$\mathbf{j}(\mathbf{r}) = -\frac{e}{2m} \sum_j [\mathbf{p}_j \delta(\mathbf{r} - \mathbf{r}_j) + \delta(\mathbf{r} - \mathbf{r}_j) \mathbf{p}_j] \equiv c[\nabla \times \mathbf{M}_L(\mathbf{r})] \quad (51)$$

such that $\mathbf{j}(\mathbf{Q}) = -ic\mathbf{Q} \times \mathbf{M}_L(\mathbf{Q})$, where $\mathbf{M}_L(\mathbf{Q})$ is the Fourier transform of the orbital magnetization. The Fourier transform of the spin magnetization is

$$\mathbf{M}_S(\mathbf{Q}) = \frac{e\hbar}{mc} \sum_j e^{i\mathbf{Q} \cdot \mathbf{r}_j} \mathbf{s}_j. \quad (52)$$

Equation (48) can then be written as

$$f^{\text{mag}} = -i \frac{\omega \mathbf{k}}{ec} [4 \sin^2 \theta \langle g | \mathbf{Q} \times [\mathbf{M}_L(\mathbf{Q}) \times \mathbf{Q}] \cdot \mathbf{P}_L | g \rangle + \langle g | \mathbf{M}_S(\mathbf{Q}) \cdot \mathbf{P}_S | g \rangle]. \quad (53)$$

The imaginary prefactor in Eq. (53) means that after taking the square modulus there is no interference between the Thomson and the magnetic scattering unless the structure factors $\sum_j \langle g | e^{i\mathbf{Q} \cdot \mathbf{r}_j} | g \rangle$ are complex, in which case the crystallographic structure is noncentrosymmetric, leading to interference terms. Nonresonant magnetic scattering has been used to separate spin and orbital moments in UAs (Langridge *et al.*, 1997).

With reference to the geometry described in Fig. 5, the scattering amplitude f^{mag} can be written as (Blume and Gibbs, 1988)

$$f^{\text{mag}} = \begin{pmatrix} f_{\sigma\sigma'} \\ f_{\sigma\pi'} \end{pmatrix} = \begin{pmatrix} \sin 2\theta M_{S2}(\mathbf{Q}) \\ \sin \theta \sin 2\theta [M_{S1}(\mathbf{Q}) + M_{L1}(\mathbf{Q})] + 2\sin^3 \theta M_{S3}(\mathbf{Q}) \end{pmatrix}, \quad (54)$$

where θ is the Bragg angle and $M_{S_i}(\mathbf{Q})$ and $M_{L_i}(\mathbf{Q})$ ($i = 1, 2, 3$) are the Cartesian components of $\mathbf{M}_S(\mathbf{Q})$ and $\mathbf{M}_L(\mathbf{Q})$ along the unit vectors \mathbf{u}_i shown in Fig. 5.

With an appropriate choice of the scattering geometry, measuring the integrated intensity of magnetic Bragg peaks as a function of the azimuthal angle ρ allows one to determine the ratio $M_L(\mathbf{Q})/M_S(\mathbf{Q})$ and to obtain information on the relative orientation of spin and orbital magnetic moments.

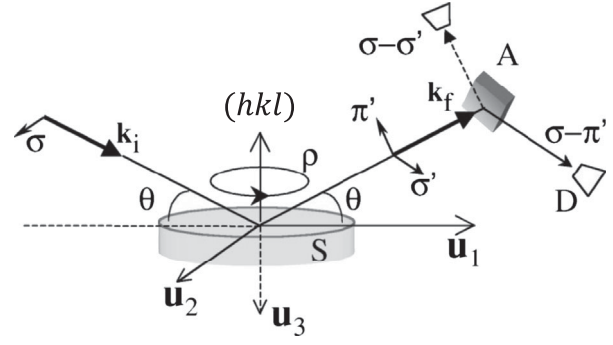


FIG. 5. Schematic representation of the experimental geometry for nonresonant magnetic diffraction measurements. The incident photon beam is polarized perpendicularly to the scattering plane (σ polarization, from the initial of the German word *senkrecht*). S is the sample, D is the detector, and A is the analyzer crystal allowing one to select the components of the scattered beam with polarization parallel (π') or perpendicular (σ') to the scattering plane. Integrated intensities of the Bragg peaks are measured as a function of the photon energy for different values of the azimuthal angle (ρ) defining the crystal orientation about the scattering vector (hkl). The unit vectors \mathbf{u}_i define the reference frame. From Caciuffo *et al.*, 2002.

E. Resonant scattering

1. Resonant elastic x-ray scattering

The resonance process in REXS gives a cross-section enhancement of several orders in magnitude together with a strong dependence on the polarization of the incident and scattered beams. The latter requires a formal description of the atomic scattering amplitude as a tensor, instead of a scalar quantity, with consequences for the angular dependence of the diffracted beam (Templeton and Templeton, 1980). It gives a sensitivity of the resonant scattering to the charge and magnetic order, as well as to the orbital order.

The atomic form factor becomes an energy-dependent complex scalar quantity (Als-Nielsen and McMorrow, 2011)

$$f(\mathbf{Q}, \omega) = f_0(\mathbf{Q}) + f'(\omega) + if''(\omega). \quad (55)$$

The nonresonant Thomson term $f_0(\mathbf{Q})$ is the Fourier transform of the electronic charge distribution in the atom, modeled as a cloud of free electrons with a spatial extent comparable to the x-ray wavelength. Therefore, f_0 is dependent on \mathbf{Q} but not on the photon energy $\hbar\omega$. On the other hand, the resonant dispersion correction term $f'(\omega) + if''(\omega)$ (also called anomalous scattering correction) describes the effect of the electrons being bound in atoms. It is therefore dependent on ω , with resonances at energies corresponding to the atomic absorption edges. It is, however, almost \mathbf{Q} independent when the electrons involved in the resonance excitation are in the K , L , or M shells, whose spatial extent is much smaller than the x-ray wavelength. We recall that the real and imaginary parts of the dispersion correction $f'(\omega)$ and $f''(\omega)$ are related by the Kramers-Kronig transformation.

According to second-order perturbation theory with H'_2 , the anomalous scattering factor in the vicinity of the absorption edge is given by

TABLE I. Binding energy (BE), x-ray attenuation length ($1/\epsilon$) at the continuum maximum, and core-level linewidth of the various absorption edges in solid uranium (density 18.92 g cm^{-3}). The BE and attenuation length values, which were obtained from [Henke, Gullikson, and Davis \(1993\)](#), do not explicitly include the white line intensity but give a good impression of the x-ray penetration depth in the solid just above the white line. The attenuation lengths for U compounds roughly scale with the inverse of the partial U density. The core-level linewidths (full widths at half maxima) were from [Raboud *et al.* \(1999\)](#) and [Caciuffo, van der Laan *et al.* \(2010\)](#) for the $O_{4,5}$ edges.

Edge	Core level	BE (eV)	Attenuation length (nm)	Core-level width (eV)
K	$1s$	115 606	108 000	
L_2	$2p_{1/2}$	20 948	5786	10.0 ± 0.1
L_3	$2p_{3/2}$	17 166	4798	8.4 ± 0.2
M_4	$3d_{3/2}$	3728	394	3.2 ± 0.1
M_5	$3d_{5/2}$	3552	444	3.3 ± 0.1
N_4	$4d_{3/2}$	778	72	4.7 ± 0.1
N_5	$4d_{5/2}$	736	78	4.2 ± 0.6
$O_{4,5}$	$5d_{3/2,5/2}$	100	12	~ 8

$$f_{\text{res}} = \frac{1}{m} \sum_n \frac{\langle g | (\boldsymbol{\epsilon}'^* \cdot \mathbf{p}) e^{-i\mathbf{k}' \cdot \mathbf{r}} | n \rangle \langle n | (\boldsymbol{\epsilon} \cdot \mathbf{p}) e^{i\mathbf{k} \cdot \mathbf{r}} | g \rangle}{E_g - E_n + \hbar\omega_{\mathbf{k}} - i\Gamma_n/2}, \quad (56)$$

where Γ_n is the full width of the emission decay. Values of Γ_n for several uranium edges were given by [Raboud *et al.* \(1999\)](#) and are reported in Table I.

Expanding $e^{i\mathbf{k} \cdot \mathbf{r}}$ as in Eq. (18) leads to electric-dipole, dipole-quadrupole, and quadrupole transitions ([Hill and McMorro, 1996](#)).

The resonant $E1$ - $E1$ scattering amplitude in Cartesian form is given by

$$F_{E1-E1} = (\mathbf{r} \cdot \boldsymbol{\epsilon}')^* (\mathbf{r} \cdot \boldsymbol{\epsilon}) = r_i^* r_j \epsilon_i'^* \epsilon_j = T_{ij} X_{ij}, \quad (57)$$

with the second-rank tensors $T_{ij} = r_i^* r_j$ and $X_{ij} = \epsilon_i'^* \epsilon_j$, which represent the geometric and dynamic tensors for the matter and x-ray probes, respectively. Since the amplitude F is a scalar, the tensors

$$\mathbf{T} = \begin{pmatrix} r_1^* r_1 & r_1^* r_2 & r_1^* r_3 \\ r_2^* r_1 & r_2^* r_2 & r_2^* r_3 \\ r_3^* r_1 & r_3^* r_2 & r_3^* r_3 \end{pmatrix}, \quad \mathbf{X} = \begin{pmatrix} \epsilon_1'^* \epsilon_1 & \epsilon_1'^* \epsilon_2 & \epsilon_1'^* \epsilon_3 \\ \epsilon_2'^* \epsilon_1 & \epsilon_2'^* \epsilon_2 & \epsilon_2'^* \epsilon_3 \\ \epsilon_3'^* \epsilon_1 & \epsilon_3'^* \epsilon_2 & \epsilon_3'^* \epsilon_3 \end{pmatrix} \quad (58)$$

must have the same symmetry properties, for instance, chiral and magnetic materials can be probed only with circular dichroism. The anisotropy of the tensor \mathbf{T} allows one to observe transitions that are otherwise forbidden in Thomson scattering ([Templeton and Templeton, 1980](#)).

Since the tensor components are physical observables, the tensor must remain the same upon symmetry transformation in the point group of the atom. This implies that in cylindrical [i.e., $\text{SO}(2)$] symmetry we have

$$\mathbf{T} = \begin{pmatrix} F^{(0)} - (1/3)F^{(2)} & -F^{(1)} & 0 \\ F^{(1)} & F^{(0)} - (1/3)F^{(2)} & 0 \\ 0 & 0 & F^{(0)} + (2/3)F^{(2)} \end{pmatrix}, \quad (59)$$

which is invariant against rotation about the z axis. Equation (59) decomposes into a scalar $F^{(0)}$, a vector $F^{(1)}$, and a traceless symmetric tensor $F^{(2)}$, also known as a deviator. The antisymmetric vector term $F^{(1)}$ is purely imaginary, which means it is time odd, i.e., magnetic. Note that the $\text{SO}(2)$ model is valid when the crystal field is negligible compared to magnetic interactions. In the most general case, all nine elements of \mathbf{T} are independent.

If the magnetic unit vector is along \mathbf{z} , by substituting Eq. (59) into Eq. (57) we obtain the well-known expression for the resonant magnetic scattering amplitude ([Hannon *et al.*, 1988](#); [van der Laan, 2008](#))

$$F_{E1-E1} = (\boldsymbol{\epsilon}'^* \cdot \boldsymbol{\epsilon}) F^{(0)} - i\mathbf{z} \cdot (\boldsymbol{\epsilon}'^* \times \boldsymbol{\epsilon}) F^{(1)} + (\boldsymbol{\epsilon}'^* \cdot \mathbf{z})(\boldsymbol{\epsilon} \cdot \mathbf{z}) F^{(2)}. \quad (60)$$

Since absorption is a special case of scattering, it is possible to link the two together. The relation between the total absorption coefficient $\sigma(\hbar\omega)$ (including all elastic and inelastic processes) and the imaginary part of the forward scattering amplitude is given by the optical theorem

$$\sigma(\hbar\omega) = \frac{4\pi n_0}{k} \text{Im} F(\mathbf{k}' = \mathbf{k}, \boldsymbol{\epsilon}' = \boldsymbol{\epsilon}, \hbar\omega), \quad (61)$$

where n_0 is the atomic density. Applying the optical theorem to Eq. (60) with \mathbf{m} along \mathbf{z} gives

$$\sigma = F^{(0)''} - i\mathbf{m} \cdot (\boldsymbol{\epsilon}'^* \times \boldsymbol{\epsilon}) F^{(1)''} + |\boldsymbol{\epsilon} \cdot \mathbf{m}|^2 F^{(2)''}, \quad (62)$$

where the double prime indicates the imaginary part of the scattering amplitude. $F^{(0)''}$, $F^{(1)''}$, and $F^{(2)''}$ correspond to the isotropic spectrum, XMCD, and x-ray magnetic linear dichroism, respectively. Note that the XMCD, which is the only term linear in \mathbf{m} , vanishes if $\boldsymbol{\epsilon}$ is real, and thus requires circular polarization.

2. Resonant inelastic x-ray scattering

In the RIXS process there is a single photon in the initial state with momentum $\hbar\mathbf{k}$, energy $\hbar\omega_{\mathbf{k}}$, and polarization $\boldsymbol{\epsilon}$ that is scattered to $\hbar\mathbf{k}'$, $\hbar\omega_{\mathbf{k}'}$, and $\boldsymbol{\epsilon}'$ in the final state ([Kotani and Shin, 2001](#); [Schülke, 2007](#); [Ament *et al.*, 2011](#)). The differential cross section is

$$\frac{d\sigma}{d\Omega} = \frac{2\pi}{\hbar} \sum_f |F_{gf}(\mathbf{k}, \mathbf{k}', \boldsymbol{\epsilon}, \boldsymbol{\epsilon}', \omega_{\mathbf{k}}, \omega_{\mathbf{k}'})|^2 \times \delta(E_g - E_f + \hbar\omega_{\mathbf{k}} - \hbar\omega_{\mathbf{k}'}), \quad (63)$$

where the resonant scattering amplitude is given by the second-order term in the KH formula with $H'_2 \sim \mathbf{A} \cdot \mathbf{p}$ as

$$\begin{aligned}
F_{gf}(\mathbf{k}, \mathbf{k}', \varepsilon, \varepsilon', \omega_{\mathbf{k}}, \omega_{\mathbf{k}'}) &= \sum_n \frac{\langle f|H'_2|n\rangle\langle n|H'_2|g\rangle}{E_g - E_n + \hbar\omega_{\mathbf{k}} + i\Gamma_n/2} \\
&= \langle f|H'_2 G(z) H'_2|g\rangle, \quad (64)
\end{aligned}$$

with the Green's function $G(z)$ as defined in Eq. (10).

RIXS should be considered a coherent coupling of the virtual absorption with the reemission process, as indicated by the two matrix elements. One can separate the full propagator G into the unperturbed propagator $G_0 = (z - H_0)^{-1}$ and a term that contains the core-hole Hamiltonian H_C using the identity $G = G_0 + G_0 H_C G$. This separates the scattering amplitude into two parts that define the direct and indirect RIXS (Ament *et al.*, 2011),

$$\begin{aligned}
F_{gf}^{\text{direct}} &= \langle f|H'_2 G_0 H'_2|g\rangle, \\
F_{gf}^{\text{indirect}} &= \langle f|H'_2 G_0 H_C G H'_2|g\rangle. \quad (65)
\end{aligned}$$

The physical picture that arises for direct RIXS is that an incoming photon promotes a core electron to an empty valence state, and subsequently an electron from a different state in the valence-band decays, thereby annihilating the core hole; see Fig. 6. Indirect RIXS is more complicated. There the incoming photon promotes a core electron to an itinerant state far above the electronic chemical potential. Subsequently, the electron in this same state decays again, filling the core hole. Scattering of the x rays occurs via the core-hole potential that is present in the intermediate state. It shakes up the electronic system, creating excitations to which the x-ray photon loses energy and momentum (Ament *et al.*, 2011). However, notice that the two processes (direct and indirect RIXS) have the same initial and final states, differing only in the involved intermediate state(s), as in a two-slit experiment. As it is impossible to determine which intermediate states the system went through, the two processes interfere unless one of the two intermediate channels is forbidden by selection rules. Usually the direct and indirect RIXS processes have large cross sections for different sets of final states; therefore, it is customary to analyze experimental results by considering only

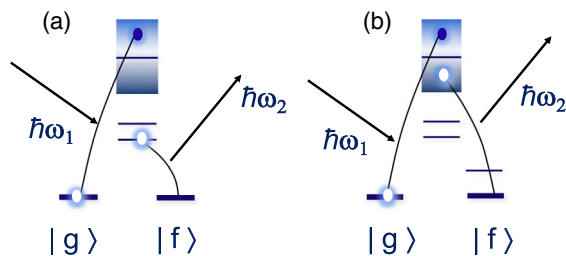


FIG. 6. Schematic representation of RIXS, a two-step process involving first the absorption of a photon and the promotion of a core electron into an empty valence state, followed by the emission of a photon with smaller energy and the filling of the core hole by an electron sitting either (a) in a core level (*direct core-to-core* RIXS) or (b) in the occupied valence band (*direct valence-to-core* RIXS). The process probes the convolution between empty (absorption step) and occupied (emission step) densities of states and leaves an electron-hole excitation in the final state. Adapted from Caciuffo and Lander, 2021.

one of the two classes of process. For instance, at the $L_{2,3}$ edges of transition metals and at the $M_{4,5}$ edges of rare-earth elements and actinides, charge-transfer, crystal-field, and spin-flip-type electronic excitations can be observed through direct RIXS. At the same edges, indirect RIXS processes allow one to observe phonon, plasmon, and bimagnon excitations (Forte, Ament, and van den Brink, 2008).

An elastic peak (Rayleigh scattering) appears when the final state is the same as the initial state. Furthermore, analogous to energy conservation, it is possible to apply momentum conservation between the initial and final states, which allows one to determine the momentum of the excitations created in the scattering process.

The RIXS process contains two radiative transitions, absorption and emission, which in the soft x-ray region obey the dipole-selection rules. The total RIXS transition, however, does not follow these rules. The ff excitations provide a typical example: The dipole transition $5f \rightarrow 5f$ would be forbidden since $\Delta\ell = 0$, but the two steps with cores $d \rightarrow 5f$ ($\Delta\ell = +1$) and $5f \rightarrow 5d$ ($\Delta\ell = -1$) are allowed, making the second-order transition possible. RIXS can therefore access transitions forbidden by dipole-selection rules. As each step follows the selection rules $\Delta J = 0, \pm 1$, the RIXS process also allows $\Delta J = \pm 2$. Under certain conditions, the orbital excitations can propagate through the crystal and give rise to an orbital wave, or “orbiton.” Such propagating collective excitations can show dispersion that has been measured by RIXS (Saitoh, Okamoto *et al.*, 2001).

RIXS also offers the possibility of exploring magnetic excitations (Ament *et al.*, 2011). Spin changes in the scattering process are allowed by the large spin-orbit coupling of the intermediate core-hole state. The angular momentum $\Delta L_z = 0, 1, 2$ can be exchanged through this coupling, thereby allowing magnetic excitations with $\Delta S_z = 0, 1, 2$. The magnetic excitations are not localized but instead propagate in the crystal as spin-wave modes (magnons). The magnon dispersion in RIXS has been shown to give results comparable to those measured by inelastic neutron scattering (Ament *et al.*, 2009).

IV. X-RAY DIFFRACTION EXPERIMENTS

Laboratory x-ray sources are usually adequate for conventional XRD crystallography on actinide materials. However, synchrotron radiation is often necessary to perform high-resolution, low-temperature, or high-pressure measurements. We now review some selected examples of such XRD experiments at SR facilities.

A. High-pressure experiments

Elemental light actinides crystallize in low-symmetry, open-packed structures that are unusual for a metal. However, these structures are prone to instability, and an external pressure of a few gigapascals is sufficient to destabilize them and induce a sequence of phase transformations. In some cases, the structural changes are accompanied by volume collapses, indicating a stepwise delocalization of $5f$ electrons and their increasing contribution to the crystal cohesion energy. High-pressure XRD experiments at synchrotron beamlines allowed one to identify the various allotropic

forms assumed by the elements in the $5f$ series, their sequence, and their range of stability. As discussed later, these experiments prompted a large amount of theoretical work, leading to the development of first-principles electronic structure calculation methods that are also reliable for strongly correlated systems.

As is well known, SR has allowed for the optimal use of diamond-anvil cells so that this field has been revolutionized by the advent of such facilities. Dedicated beamlines and special equipment have been developed at all of the major SR sources, as described by Mezouar *et al.* (2005), Shen *et al.* (2005), Liermann *et al.* (2015), Meng *et al.* (2015), and Hirao *et al.* (2020). A recent review was given by McMahon (2022). A number of works have been carried out on uranium compounds to determine crystal structural variation and equations of state. Some examples were given by Staun Olsen *et al.* (1988), Yoo, Cynn, and Söderlind (1998), Haire *et al.* (2003), Le Bihan *et al.* (2003), Dewaele *et al.* (2013), Jeffries *et al.* (2013), Zvoriste-Walters *et al.* (2013), Rittman *et al.* (2017), Shukla *et al.* (2017), Murphy *et al.* (2018), and Guo *et al.* (2019).

Figure 7 shows the equation of states for α -U, Am, and Cm as determined by high-pressure XRD. Under compression, uranium preserves its room-temperature-stable orthorhombic $Cmcm$ form up to at least 100 GPa. Different behavior is observed for americium, where the normal pressure, double-hexagonal, close-packed ($P6_3/mmc$) structure transforms at 6.1 GPa to a face-centered cubic ($Fm\bar{3}m$) lattice. At higher pressures, two lower symmetry structures appear, a face-centered orthorhombic Am III ($Fddd$) and a primitive orthorhombic structure, Am IV ($Pnma$). In the same pressure range, up to 100 GPa, curium exhibits five phases, from the double-hexagonal close-packed form of Cm I ($P6_3/mmc$) to the orthorhombic ($Pnma$) structure of Cm V. Of particular interest is the formation of the monoclinic structure with the space group $C2/c$ between about 37 and 56 GPa. Calculations based on the full potential linear muffin-tin orbital method

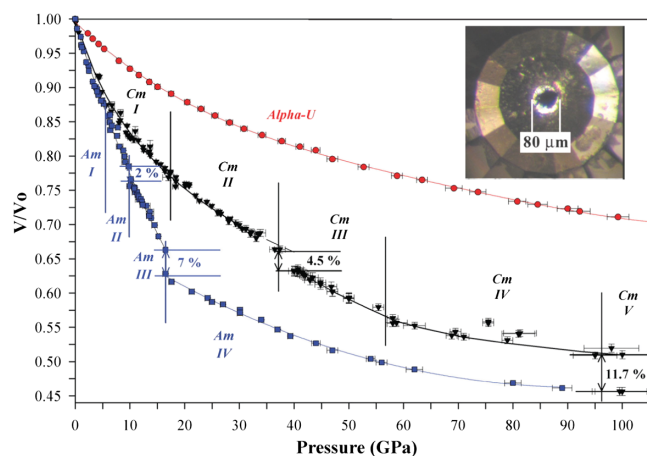


FIG. 7. Pressure dependence of the normalized unit cell volume $V(p)/V_0$ for α -uranium (Le Bihan *et al.*, 2003), americium (Lindbaum *et al.*, 2001), and curium (Heathman *et al.*, 2005). Inset: typical diamond-anvil cell used for angle-dispersive, high-pressure x-ray diffraction experiments. Adapted from Heathman *et al.*, 2005.

suggest that its stabilization is driven by the magnetic correlation energy (Heathman *et al.*, 2005). The collapse of Am and Cm from simple to complex structures under pressure shows, in line with Fig. 1, that the $5f$ electrons have transformed from localized to itinerant under pressure.

Beyond Cm, the available quantities become small, but recent work has shown that the concept of delocalization under pressure may be too simple of a picture. Examples are pressure work on Cf (Heathman *et al.*, 2013) and spectroscopy work on Es (Carter *et al.*, 2021), both of which use SR techniques.

Reproducing from first-principles electronic structure calculations the observed sequence of lattice geometry and the associated evolution of physical properties in actinide elements and compounds is challenging. Simple approximations of the density-functional theory, in fact, are not adequate for actinide materials, because of the strong intra-atomic correlations, the importance of scalar (first-order kinetic energy correction due to the mass variation) and nonscalar (spin-orbit coupling) relativistic effects, and the extent of the hybridization between $5f$ and the conduction electrons. In many cases a model that produces the correct crystal structure at a certain atomic volume fails to describe the electronic structure near the Fermi level and does not reproduce the correct magnetic state. This is the case of conventional density-functional theory (DFT) calculations in the local-spin density or generalized-gradient approximation (LDA/GGA) applied to δ -Pu (Lashley *et al.*, 2005; Joyce and Lander, 2019), or of static mean-field correlated band theory calculations making use of different flavors of the LDA/GGA plus Coulomb U (LDA + U) method, falling short of describing the itinerant-to-localized crossover of the $5f$ manifold in PuCoGa₅ (Daghero *et al.*, 2012; Shick *et al.*, 2013). During the last two decades, experiments such as those reported in Fig. 7 have, therefore, stimulated the development of increasingly sophisticated theoretical models that have now reached predictive capabilities close to a material-by-design level also for compounds in the $5f$ block (Kotliar *et al.*, 2006; Shim, Haule, and Kotliar, 2007; Suzuki, Magnani, and Oppeneer, 2010; Pezzoli, Haule, and Kotliar, 2011; Dudarev *et al.*, 2019; Pourovskii and Khmelevskiy, 2021; Shick, Fujimori, and Pickett, 2021). A review on methods for computing the electronic structure of correlated materials from first principles was given by Nilsson and Aryasetiawan (2018).

B. High intensity and resolution

The large increase in flux of modern synchrotron beams compared to conventional x-ray sources has meant that much smaller samples can be studied with increasing resolution. As an example of a high-resolution XRD study, we show in Fig. 8 the results obtained for the PuCoGa₅ unconventional superconductor (Eloirdi *et al.*, 2017). The experiment was performed at the ESRF ID22 beamline, affording a resolution $\Delta d/d = 10^{-6}$ at $\lambda = 0.354155$ Å. Data were collected on a 4.6 mg sample, obtained by crushing a single crystal grown from metallic plutonium (99.932 wt% ²⁴²Pu), put inside a hermetic holder providing four levels of containment. The absence of visible splitting or broadening of the diffraction peaks, as seen in the inset of Fig. 8 for the (220) Bragg

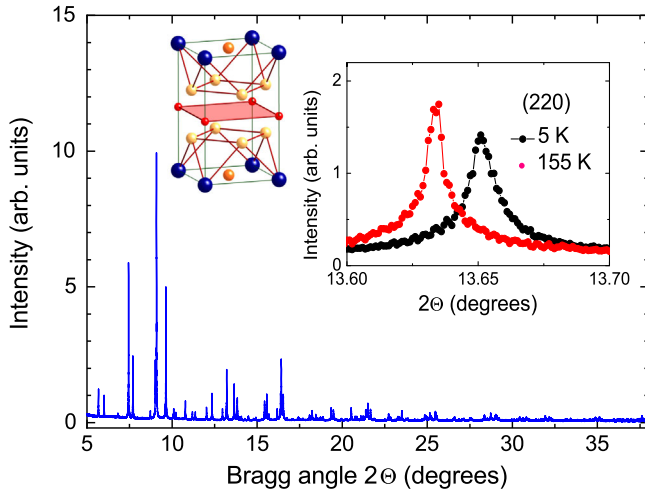


FIG. 8. X-ray diffraction pattern recorded for PuCoGa_5 at 5 K. Left inset: tetragonal crystallographic unit cell, with Pu and Co atoms represented by blue and red spheres, respectively. The two inequivalent Ga atoms are shown as orange and yellow spheres. Right inset: (220) Bragg peak measured at 5 K (black circles) and 155 K (red circles). Adapted from Eloidri *et al.*, 2017.

reflection, indicates that the tetragonal symmetry is preserved in the superconducting phase. The temperature dependence of the refined lattice parameters shows that the thermal expansion is isotropic above ~ 150 K. At lower temperatures, the c/a ratio increases with a decreasing T . In the same temperature range, Ramshaw *et al.* (2015) observed a softening of the bulk modulus that they attributed to the development of in-plane hybridization between conduction electrons and Pu $5f$.

Below $T_c = 18.5$ K, the critical temperature to the superconducting state in PuCoGa_5 , the expansion of the unit cell volume deviates from the predictions of a simple one-phonon Grüneisen-Einstein model (Fig. 9). The shrinking of the cell volume is similar to the one observed for the CeRu_2Si_2 Kondo system (Hiranaka *et al.*, 2013) and could suggest the

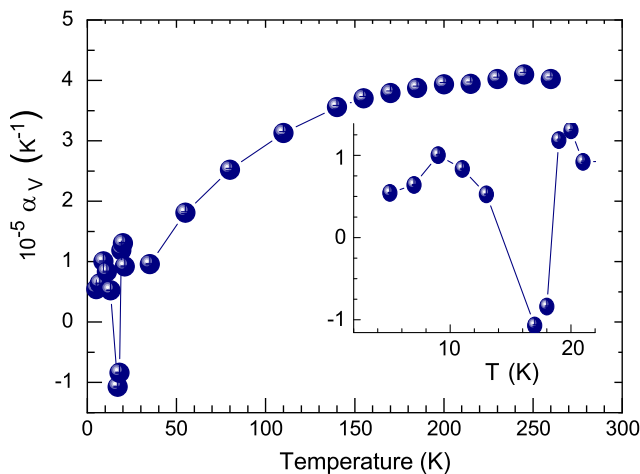


FIG. 9. Thermal expansion coefficient for the unit cell volume of PuCoGa_5 (on an expanded scale around T_c in the inset). Error bars have been estimated as 5 times the statistical error provided by the Rietveld refinement and are smaller than the data symbol size. Adapted from Eloidri *et al.*, 2017.

occurrence of critical valence fluctuations at T_c (Miyake and Watanabe, 2014), where the volume thermal expansion coefficient α_V has a jump larger by a factor of ~ 20 than the value predicted by the Ehrenfest relation.

Diffraction experiments on other transuranium samples, such as NpFeAsO , have also benefited from the additional intensity and resolution of synchrotron beamlines (Klimczuk *et al.*, 2012). Since the structure of the Np compound was understood by performing both synchrotron and neutron experiments on polycrystalline samples, there was no need to use synchrotron x rays for the Pu analog (Klimczuk, Shick *et al.*, 2012).

In addition to looking at polycrystalline samples of complex materials, it is also possible to perform new experiments with synchrotron beams that are almost impossible to perform with conventional x-ray sources. A good example of such a study is that examining the change in the surface morphology of a UO_2 single crystal by measuring the so-called truncation rods as a function of time while the sample is exposed to oxygen. The work of Stubbs *et al.* (2015) showed the power of this technique. Figure 10, from Stubbs *et al.* (2015), shows a modulation of the layers that incorporate the extra oxygen such that they are organized to appear in every third layer down, in the case of the (111) surface. The arrangement is modeled from the intensity of the truncation rods measured in the Advanced Photon Source (APS) at the Argonne National Laboratory (ANL). A similar situation was found in the case of the UO_2 (001) surface (Stubbs *et al.*, 2017).

Another experiment demanding intense SR was that performed at APS on molten UO_2 that was levitated and then heated with a laser beam to determine the structural changes near the melting temperature (3138 K) (Skinner *et al.*, 2014). The hot solid shows a substantial increase in oxygen disorder around the λ transition (2670 K) but a negligible U-O coordination change. On melting, the average U-O coordination drops from 8 to 6.7 ± 0.5 . Molecular dynamics

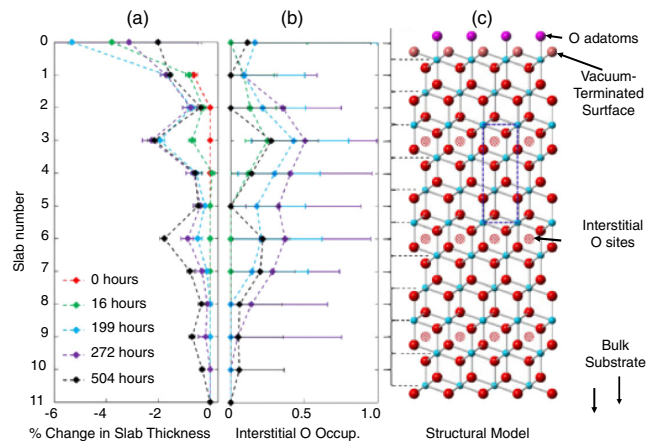


FIG. 10. (a) Refined slab contractions and (b) interstitial occupancies vs depth and three-layer periodicity. (c) Proposed model for an oxidized UO_2 (111) surface. U, cyan; structural O, red; surface O adatoms, magenta; interstitial O, hatched red. The surface is oxygen terminated. The YZ projection of the surface unit cell is indicated by the blue dashed lines. From Stubbs *et al.*, 2015.

models refined to this structure predict higher U-U mobility than in eight-coordinated melts.

Finally, in this section we cover a study attempting to use nonresonant scattering to determine the individual spin and orbital moments in the uranium mononictide (with the simple NaCl crystal structure) UAs. That x-ray scattering has a “magnetic” component was known many years ago, and pioneering experiments had already shown such weak magnetic scattering from a conventional x-ray source with the antiferromagnet Fe_2O_3 (Brunel and de Bergevin, 1981; de Bergevin and Brunel, 1981). However, the signal was weak, as it is many orders of magnitude smaller than any charge contribution. With the much higher intensity available from a synchrotron beam together with a new formulation of the theory (Blume and Gibbs, 1988), an attempt was made at the ESRF on the actinide system UAs (Langridge *et al.*, 1997). Five different antiferromagnetic satellites were observed, and the final value of the ratio of the orbital-to-spin moment was found to be $\mu_L/\mu_S = -2.0 \pm 0.5$. The expected values for simple $5f^2$ or $5f^3$ configurations are -3.30 and -2.6 , so the result suggested a $5f^3$ configuration, as is generally accepted. Despite using SR, this experiment turned out to be difficult, requiring accurate intensity measurements of weak satellite reflections using photons of 8.1 keV. To our knowledge, these types of experiments have not been repeated on any actinide system, perhaps because of the development of another technique, XMCD, which is discussed in Sec. VI.C. However, XMCD cannot be used for antiferromagnetic materials.

C. Experiments at high magnetic fields

A number of experiments using pulsed magnetic fields have been performed with SR (Detlefs, Duc *et al.*, 2008), but the first one on an actinide system was reported from the APS on UO_2 (Antonio *et al.*, 2021). The results are shown in Fig. 11.

As discussed later, UO_2 is an antiferromagnet with $T_N = 30.8$ K and orders with a so-called $3\mathbf{k}$ antiferromagnetic (AFM) structure, as determined many years ago. Recently work at high magnetic fields at Los Alamos National Laboratory has shown that interesting magnetoelastic effects occur when high magnetic fields are applied along the $\langle 111 \rangle$ direction with the samples in the AFM state (Jaime *et al.*, 2017). Further information on these effects was obtained by performing an experiment at the APS synchrotron with applied magnetic fields up to 25 T (Antonio *et al.*, 2021). Because of the constraints of the experiment, only one reflection [the (888) one] could be measured. For $T > T_N$, it was a single reflection. However, as shown in Fig. 11, in the AFM state two reflections were observed, and the process was reversible. Antonio *et al.* (2021) discussed this in terms of piezomagnetic domains, although they did not explain how such domains with different d spaces give the two reflections. A simpler quantitative explanation exists if one assumes that the crystal undergoes a rhombohedral distortion along a domain with its $[111] \parallel \mathbf{H}$. Other $\langle 111 \rangle$ -type directions in the crystal (which are not parallel to \mathbf{H}) will have a d space inequivalent to those with $\mathbf{H} \parallel [111]$. This hypothesis, which was described by Lander and Caciuffo (2021), explains the presence of two reflections (Fig. 11) as well as their relative slopes and intensities as a function of the applied H .

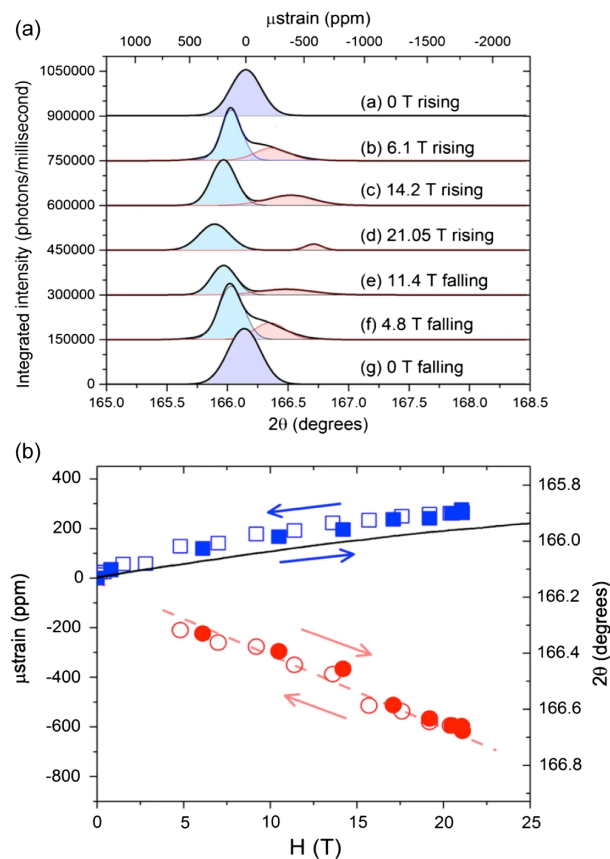


FIG. 11. (a) Waterfall plot of fits to the integrated intensity along the full diffraction angle 2θ of selected fields at 15 K. The peak at lower 2θ (blue) corresponding to expansion is much larger than the peak at higher 2θ (red). (b) Peak positions of the two peaks at 15 K, with filled symbols corresponding to a rising field and open symbols to a falling field. The red circles represent the smaller peak and blue squares indicate the larger one. The blue peak and its positive magnetostriction can be seen to match magnetostriction measurements using the fiber Bragg grating technique (black line), with an ~ 150 ppm expansion at the maximum 21.1 T applied field. The red dashed line is a guide for the eye. From Antonio *et al.*, 2021.

A complete understanding of this effect and how it relates to earlier work remains to be determined.

D. Materials science and microstructural studies

The intensity and micron dimensions of the x-ray beams has also allowed a multitude of experiments to be performed in what might be loosely called materials science. We give four examples in this section, and there is little doubt that other experiments will be done in the future. Normally, these experiments use high-energy x rays to ensure deep penetration into the material being examined. There is also use of tomography techniques that we mention here (although they are not related to diffraction) for determining the pore (or impurity) structure inside the sample; i.e., the method is nondestructive.

An interesting experiment performed on thin films and following the diffraction pattern as a function of time (and hydrogen dose) was conducted by Darnbrough *et al.* (2018) at

the ESRF. The sample started with an epitaxial film of α -U and then either a layer of polycrystalline UO_2 was deposited on top of the epitaxial metal film or an oxide film was allowed to grow naturally by exposing the film to air. After this, the diffraction pattern was taken over a period of time when hydrogen was bled into the chamber, with the sample also being heated. The U-H reaction is known to be strongly exothermic, and these experiments also exhibit an anisotropy; certain faces in the U metal react more rapidly with H_2 than others. The entry of hydrogen is seen to reduce the UO_2 lattice and expand that of the metal. It appears that the reaction is strongly localized at grain boundaries, so amorphous or nanocrystalline UH_3 is formed at such boundaries and no diffraction peaks from this material are observed. More experiments need to be performed, but this represents an interesting first test.

Tomography has turned out to be a key feature that can be performed with high-energy synchrotron beams and can achieve micron-size resolution. With the new optic features of recent synchrotron upgrades, this resolution will reach submicron size. We next feature three papers that have been exemplary in opening up new areas in materials science. In the first, [Bonnin *et al.* \(2014\)](#) explored the impurities (normally around the 1% level) in the atomization process that is used to prepare U-Mo droplets, from which pellets are prepared for the new generation of low-enriched-uranium fuels for research reactors. The impurities are UO_2 and grains of $\text{U}(\text{C}, \text{O})$. The experiments, which were done on ID11 at the ESRF, used a beam of ~ 30 keV and a focal-spot size of $0.11 \times 0.14 \mu\text{m}^2$. The results showed that the UO_2 deposits on the surface of the droplets (as expected), but the $\text{U}(\text{C}, \text{O})$ impurity phases, which have the face-centered-cubic (fcc) NaCl structure, grow directly from the body-centered-cubic (bcc) U-Mo main component. For example, it was found that the diameter of the bcc U-Mo particles is much larger in the regions where $\text{U}(\text{C}, \text{O})$ impurities were found. Evidence shows that the onset of $\text{U}(\text{C}, \text{O})$ grain crystallization can be described using a precipitation mechanism since a single U-Mo grain has a direct orientation relationship with more than one surrounding $\text{U}(\text{C}, \text{O})$ grain. In addition, the porosity could be directly observed, and the relationship with the outer UO_2 coating could be determined.

The second example examined an irradiated U-Zr fuel ([Thomas *et al.*, 2020](#)). The sample had a volume of $\sim 125 \times 90 \times 100 \mu\text{m}^3$ and was prepared using the focused-ion-beam (FIB) method from a sample of U-Zr 10 wt % fuel pin that was irradiated to 5.7 at. % burnup in a reactor. The experiments were performed on beamline 1-ID-E at the APS with a beam of incident energy of 71.68 keV. The total radiation inventory was not given, but the safety conditions included the specification that the sample had to give less than 5 mR/h at 30 cm, which was achieved. On contact the sample measured 40 mR/h. The principal result is a detailed mapping of the U concentration and the pores in this irradiated material, as shown in Fig. 12.

A clear indication of the pore structure in such an irradiated fuel has not yet been obtained, so there is much to analyze here and compare with estimates of such pore sizes using numerical methods. The localized microscopic swelling of the

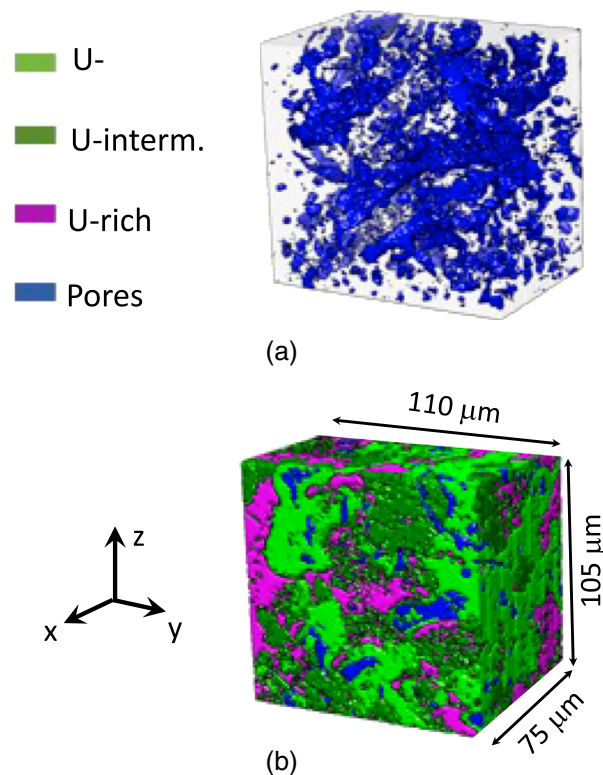


FIG. 12. Three-dimensional segmentation of the propagation-based phase contrast enhanced tomography images of a U-10Zr FIB cuboid indicating (a) the pores and (b) a composite image of pores and all three phase regions. From [Thomas *et al.*, 2020](#).

fuel was estimated from these results as just under 8%, whereas the macroscopic swelling has been measured as a function of burnup and has been found to be about twice this value, i.e., $\sim 16\%$. This large discrepancy is not completely understood, but [Thomas *et al.*](#) gave a number of reasons that may play a role.

The third example is an x-ray tomography experiment conducted at room temperature and 1000°C on unirradiated tristructural isotropic (TRISO) nuclear fuel particles under uniaxial compression ([Liu *et al.*, 2020](#)). The TRISO particles were part of a neutron irradiation experiment ([Knol *et al.*, 2012](#)) made at the High Flux Reactor in Petten, Netherlands, to study the impact of high-temperature fast neutron irradiation on the thermomechanical properties of TRISO particles with various coating materials. X-ray tomography measurements were performed at the beamline 8.3.2 of the Advanced Light Source (ALS) at the Lawrence Berkeley National Laboratory in Berkeley, CA, using a monochromatic beam of 25 keV. The results allowed [Liu *et al.* \(2020\)](#) to correlate the microstructure and dimensions of the individual layers of each particle to the load-displacement behavior and provided real-time information on the evolution of porosity, crack formation, and layer thickness as a function of stress and temperature.

These three experiments use tomography, a technique requiring vast arrays of data, so capabilities go hand in hand with advances in image reconstruction. We can expect more of these types of experiments that feed directly into questions of importance to the nuclear industry in terms of fuel fabrication,

utilization, and later no doubt fuel treatment and waste disposal. In this field it is clear that the advances in synchrotron lattice upgrades, optics, and resolution will further enhance capabilities, and when using free-electron lasers the beams will be even smaller.

Another technique that we do not describe in detail in this review but that has considerable potential in the study of colloidal and nanostructured materials is small angle x-ray scattering (SAXS), i.e., diffuse scattering produced around the incident beam by sample inhomogeneities (scattering length fluctuations) with sizes several times larger than the nearest-neighbor interatomic distances. A SAXS experiment is sensitive to microstructural details up to a few thousand angstroms and provides information on the surface, volume, and shape of the inhomogeneities, on the distribution of their sizes, and on the interparticle correlation. In actinide science, SAXS has been used to study the formation of atomic clusters (Burns *et al.*, 2005), polynuclear colloidal particles (Zhai *et al.*, 2022), the interactions between natural colloidal organic matter and actinides in solutions (Tian *et al.*, 2020), and the solution speciation of metal-oxo clusters (Nyman, 2017).

V. REXS EXPERIMENTS

A. Electric-quadrupole order

REXS occurs when a photon is absorbed, promoting a core electron to an empty state, and is subsequently reemitted when the electron and the core hole recombine. The process can introduce an anisotropic contribution to the x-ray susceptibility tensor, whose amplitude strongly increases when the photon energy is tuned to an atomic absorption edge. The scattering amplitude also depends on the initial and final polarization of the photons. Measurements are usually performed with incident photons linearly polarized along the direction perpendicular to the scattering plane (σ polarization), while optionally a polarization analyzer is used to detect photons linearly polarized either along the same direction ($\sigma\sigma$ channel) or parallel to the scattering plane ($\sigma\pi$ channel). In REXS experiments performed without energy analysis of the scattered photons, a careful check of the inelastic background should be performed, particularly when dealing with weak and broad peaks in the reciprocal space.

The first REXS measurements were performed with photons tuned to the L edges of holmium metal (Gibbs *et al.*, 1988), and it was soon realized that to observe the maximum magnetic effects one has to tune to energies that are associated with empty states of the spin-polarized electrons, i.e., $L_{2,3}$ edges for $3d$ systems, and $M_{4,5}$ edges for $4f$ and $5f$ systems. At the M_4 edge of uranium in UAs, an antiferromagnetic compound with the rocksalt fcc crystal structure, an increase in intensity of 6 orders of magnitude was observed for the magnetic Bragg peak in the ordered phase (Isaacs *et al.*, 1989).

For an $E1$ transition involving the excitation $3d_{3/2,5/2} \rightarrow 5f$ at the $M_{4,5}$ absorption edges of an actinide atom, the resonant x-ray scattering amplitude contains a scalar term probing the electric charge, a rank-1 tensor odd in time-reversal symmetry probing the magnetic-dipole moment, and a rank-2 tensor even under time reversal probing the electric-quadrupole moment,

$$f_{E1} = \frac{2}{3}(\mathbf{e}'^* \cdot \mathbf{e})[F_{11} + F_{1-1} + F_{10}] - i(\mathbf{e}'^* \times \mathbf{e}) \cdot \mathbf{z}[F_{11} - F_{1-1}] + \frac{1}{3}(\mathbf{e}'^* \cdot \mathbf{T} \cdot \mathbf{e})[2F_{10} - F_{11} - F_{1-1}], \quad (66)$$

where \mathbf{e} (\mathbf{e}') are unit polarization vectors of the incident (scattered) photons, \mathbf{z} is the direction of the magnetic-dipole moment, \mathbf{T} is a rank-2 tensor proportional to the electric-quadrupole operators or arising from an intrinsic asymmetry of the crystal lattice, and F_{1q} ($q = 0, \pm 1$) are resonant energy factors (Hill and McMorro, 1996). In resonant scattering, where the excitation is from core states that are close to the nucleus, the scatterers can be taken as points in space. This implies that the scattering will have almost no Q dependence, unlike nonresonant x-ray scattering with an atomic form factor. In this sense there is an analogy with neutron scattering from the nucleus, which can also be regarded as a point source.

If magnetic-dipole or electric-quadrupole moments exhibit long-range order and the photon energy is large enough for diffraction to occur, the interference of the anomalous scattering amplitudes lead to the appearance of Bragg peaks at positions \mathbf{Q} forbidden by the crystallographic space group. Their intensity depends on the incident photon energy across the $M_{4,5}$ actinide absorption edge (see Fig. 13), the polarization of the incident and diffracted photons, and the sample rotational orientation around the scattering vector \mathbf{Q} (azimuthal angle ρ).

In the case of electric-quadrupole order, the structure factor is obtained from the electric-quadrupole operators in Cartesian components $\mathbf{T}_n = (J_i J_j + J_j J_i)/2$, with $ijk = xyz$ and J the angular momentum operator, as

$$\mathbf{F}'(\mathbf{Q}) = \sum_n \mathbf{T}_n \exp(i\mathbf{Q} \cdot \mathbf{r}_n), \quad (67)$$

where the sum runs over all the atoms in the unit cell at positions \mathbf{r}_n and the scattering amplitude at resonance conditions is $F(\mathbf{Q}) = \mathbf{e}' \cdot \mathbf{F}'(\mathbf{Q}) \cdot \mathbf{e}$.

The capability of the REXS technique to detect higher-order electric multipoles has attracted great interest; some examples were given by Santini *et al.* (2009). Important early work was done on UPd₃ (McMorro *et al.*, 2001; Walker *et al.*, 2006, 2008; Walker, Le *et al.*, 2011), and extended experiments were carried out to investigate the ordered ground state of actinide dioxides. Notably, REXS experiments have provided direct evidence for the ordering of electric-quadrupole moments in UO₂ (Wilkins *et al.*, 2006), NpO₂ (Paixão *et al.*, 2002; Caciuffo *et al.*, 2003), and in mixed U_{1-x}Np_xO₂ solid solutions (Wilkins *et al.*, 2004). These oxides crystallize in the fcc fluorite structure, but in the ordered phase resonant superlattice Bragg peaks appear at positions that are forbidden in the $Fm\bar{3}m$ space group, such as $\mathbf{Q} = (00\ell)$, $\ell = 2n + 1$. The nature of the order parameter can be established by analyzing the azimuthal angle dependence of their intensity in different polarization channels. As shown in Eq. (66), the term probing magnetic dipoles rotates the photon polarization by $\pi/2$. If measurements are performed with σ -polarized incident photons, magnetic scattering appears only in the $\sigma\pi$ channel, whereas quadrupole scattering will contribute to both the $\sigma\pi$ and $\sigma\sigma$ channels. The intensity modulation of the forbidden

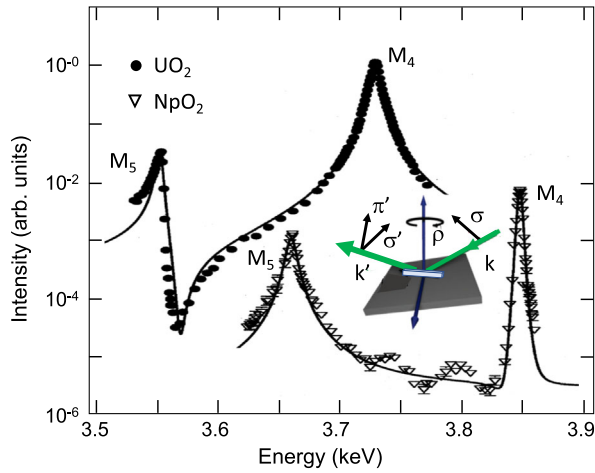


FIG. 13. Integrated intensity of the (003) superlattice Bragg peak as a function of the photon energy around the M_5 and M_4 absorption edge of U and Np in UO_2 and NpO_2 , respectively. Data were collected in the ordered phase, with the incident beam polarized perpendicularly to the diffraction plane (σ) and the scattered photon beam polarized in the diffraction plane (π). The intensity data are corrected for self-absorption. The maxima of the intensity enhancement occur at the electric-dipole transition threshold energy and are associated with $3d_{3/2,5/2} \rightarrow 5f$ transitions. Note that the shape of the M_4 resonance in NpO_2 is a Lorentzian squared, as predicted by Nagao and Igarashi (2005). Inset: sketch of the scattering geometry used to measure the integrated intensity as a function of the azimuthal angle ρ describing the rotation of the sample about the scattering vector. The arrows $\varepsilon(\sigma, \pi)$ correspond to the polarization direction of photons polarized perpendicularly (σ) or parallel (π) to the scattering plane. Adapted from Caciuffo and Lander, 2021.

peaks provides information on the relative orientation of the moments carried by the atoms in the base of the unit cell.

UO_2 orders at $T_N = 30.8$ K. The primary order parameter is the magnetic dipole, while electric quadrupoles act as secondary order parameters. A $3\mathbf{k}$, type-I, transverse antiferromagnetic structure with propagation vector $\mathbf{k} = (001)$ becomes stable below T_N (Burlet *et al.*, 1986; Blackburn *et al.*, 2005). The symmetry of the lattice is reduced to $Pa\bar{3}$, and the uranium sublattice becomes simple cubic. Each of the four atoms in the base (C_{2h} point group) carries an electric-quadrupole moment given by a linear combination of the three Γ_5 quadrupoles transforming as xy , xz , and yz . The resulting order is also transverse $3\mathbf{k}$. The two possible symmetry-equivalent S domains are shown schematically in Figs. 14(b) and 14(c). A visual inspection of the figure makes it immediately evident that, for a transverse configuration [Figs. 14(b) and 14(c)] and not for the longitudinal configuration [Fig. 14(a)], the order of the electric quadrupoles must be accompanied by an internal distortion of the oxygen sublattice as a consequence of the perturbed electrostatic interaction between the oxygen anions and the asymmetric $5f$ electronic cloud around the uranium ions. This distortion of the oxygen atoms in UO_2 was first reported in 1975 with the use of neutron scattering (Faber, Lander, and Cooper, 1975), but the reason for the distortion was not understood at the time. Neutrons cannot observe the electric quadrupoles.

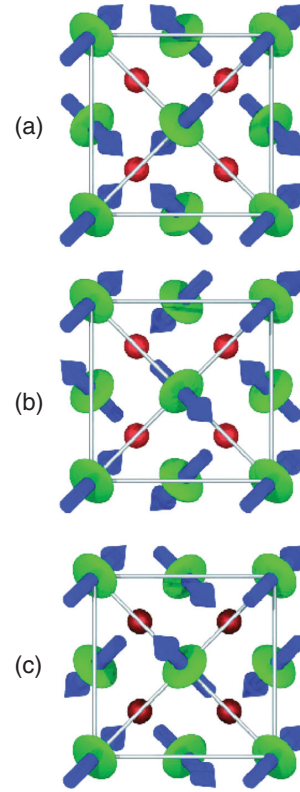


FIG. 14. Schematic representation of the projection onto the a - b plane of the $3\mathbf{k}$ magnetic-dipole and electric-quadrupole ordering for (a) the longitudinal configuration and (b),(c) the two S domains of the transverse configuration. The magnetic-dipole moments are represented by blue arrows, whereas the electric-quadrupole moments are shown as green ellipsoids. The red spheres represent oxygen atoms. UO_2 adopts the transverse structure, whereas the electric-quadrupole longitudinal order is realized in NpO_2 with zero magnetic-dipole moment. Adapted from Wilkins *et al.*, 2006.

In NpO_2 , a second-order phase transition is observed at $T_0 = 25$ K. In this case, the crystallographic structure is preserved, and neither external nor internal distortions are observed (Boeuf *et al.*, 1983; Caciuffo *et al.*, 1987). The crystal-field potential was established by inelastic neutron scattering experiments, indicating a Γ_8 quartet ground state (Fournier *et al.*, 1991; Amoretti *et al.*, 1992). The Ψ dependence of the (001) and (003) Bragg peak intensity has been measured with the sample kept at $T = 10$ K at the maximum of the M_4 absorption edge ($E = 3.846$ keV) (Mannix, Lander *et al.*, 1999; Paixão *et al.*, 2002). Data collected in the $\sigma\pi$ and $\sigma\sigma$ channels have been used to obtain the Stokes parameters

$$P_1 = \frac{|F_{\sigma\sigma}|^2 - |F_{\sigma\pi}|^2}{|F_{\sigma\sigma}|^2 + |F_{\sigma\pi}|^2},$$

$$P_2 = \frac{|F_{\sigma\sigma} + F_{\sigma\pi}|^2 - |F_{\sigma\sigma} - F_{\sigma\pi}|^2}{|F_{\sigma\sigma} + F_{\sigma\pi}|^2 + |F_{\sigma\sigma} - F_{\sigma\pi}|^2}. \quad (68)$$

Figure 15 shows the experimental results. The lines in the figure correspond to calculations assuming the longitudinal $3\mathbf{k}$ order of Γ_5 electric quadrupoles shown in Fig. 14(a) and

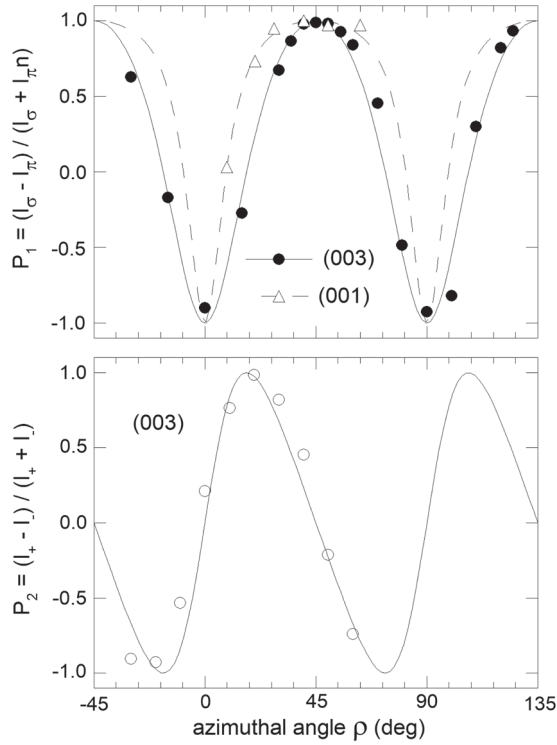


FIG. 15. Azimuthal angle dependence of the Stokes parameters P_1 and P_2 for the (001) and (003) superlattice reflections measured in NpO_2 at 10 K with $E = 3.846$ keV. The origin of the azimuthal angle ρ corresponds to the a axis lying in the scattering plane. The lines are calculations based on a longitudinal $3k$ order of Γ_5 electric quadrupoles with an ordered magnetic-dipole moment equal to zero. No fitting parameters are involved. Adapted from Caciuffo *et al.*, 2003.

assuming an ordered magnetic-dipole moment equal to zero (Caciuffo *et al.*, 2003).

For a $\mathbf{Q} = (00\ell)$ reflection, choosing $\rho = 0$, where the $[100]$ vector is in the scattering plane with a component parallel to the incident photon beam, the azimuthal and polarization dependences of the REXS amplitude for the considered structure are

$$\begin{aligned} F_{\sigma\sigma} &= 4\Phi \sin 2\rho, \\ F_{\sigma\pi} &= 4\Phi \sin \theta \cos 2\rho, \end{aligned} \quad (69)$$

where Φ is the quadrupole-order parameter. Therefore,

$$\begin{aligned} P_1 &= \frac{\sin^2 2\rho - \sin^2 \theta \cos^2 2\rho}{1 - \cos^2 \theta \cos^2 2\rho}, \\ P_2 &= \frac{\sin \theta \sin 4\rho}{1 - \cos^2 \theta \cos^2 2\rho}. \end{aligned} \quad (70)$$

The agreement between the experimental and calculated data in Fig. 15 is good considering that no fitting parameters are used. As a consequence of the quadrupole order, the point symmetry at the Np site is reduced to D_{3d} and the space group is lowered to $Pn\bar{3}m$. However, with Np ions on $4b$ and O ions on $2a$ and $6d$ Wyckoff positions, the crystallographic extinction rules remain the same as those of the $Fm\bar{3}m$ space group. In addition, for NpO_2 quadrupoles are not the primary order

parameter. Indeed, by probing the dynamics of the ordered state by inelastic neutron scattering, it appears that the driving order parameter is provided by the rank-5 magnetic trikonadipoles (Santini *et al.*, 2006; Magnani *et al.*, 2008).

Searches for quadrupolar order by REXS experiments have also been performed on URu_2Si_2 . This intermetallic compound has been widely investigated in an attempt to explain the nature of its phase transition at $T_0 = 17.5$ K (Mason *et al.*, 1990; Broholm *et al.*, 1991; Walker *et al.*, 1993; Santini and Amoretti, 1994; Santini *et al.*, 2000; Amitsuka *et al.*, 2010; Mydosh and Oppeneer, 2011; Oppeneer *et al.*, 2011; Walker, Caciuffo *et al.*, 2011; Chandra, Coleman, and Flint, 2015; Wang *et al.*, 2017; Mydosh, Oppeneer, and Riseborough, 2020). The puzzle arises from the difficulty in reconciling the minute value of the ordered magnetic moment ($\mu_0 = \sim 0.03\mu_B$ along the c axis of the tetragonal unit cell) with the large macroscopic anomalies observed at T_0 (Mason *et al.*, 1990; Broholm *et al.*, 1991; Walker *et al.*, 1993). For instance, if the order parameter were the magnetic-dipole moment, the anomaly in the specific heat should be ~ 30 times smaller. This indicates that macroscopic anomalies are associated not with μ_0 but with a hidden order parameter not directly coupled to scattering probes. Among a number of theoretical models (Oppeneer *et al.*, 2011; Mydosh, Oppeneer, and Riseborough, 2020), a staggered ordering of electric quadrupoles have also been suggested to occur in URu_2Si_2 (Santini and Amoretti, 1994; Santini *et al.*, 2000).

REXS experiments at the UM_4 absorption edge have not confirmed this hypothesis (Amitsuka *et al.*, 2010; Walker, Caciuffo *et al.*, 2011). Data have been collected on high-quality single crystals of URu_2Si_2 with low residual stress, cut with a plane face perpendicular to the $[101]$ direction, spanning an extended region of the reciprocal space plane $[HOL]$, including the nesting vector $(1.4, 0, 0)$ suggested by neutron scattering experiments. The results of both studies (Amitsuka *et al.*, 2010; Walker, Caciuffo *et al.*, 2011) exclude electric quadrupoles of any symmetry as a hidden order parameter with a propagation vector in the explored region. Indeed, as shown in the top panel of Fig. 16, forbidden Bragg peaks emerging in the ordered state have nonzero intensity only in the $\sigma\pi$ polarization channel, with an azimuthal angle dependence corresponding to an ordered magnetic-dipole moment along the crystallographic c axis. The bottom panel of Fig. 16 shows that the ρ dependence of the superlattice peak intensity is sensitive to the inclusion of a component of the ordered magnetic moment in the a - b plane, whose estimated upper limit is $\sim 0.003\mu_B$. This experimental result essentially eliminates the idea of hastatic order proposed by Chandra, Coleman, and Flint (2015).

An attempt to detect multipolar order parameters in URu_2Si_2 with REXS measurements at the UL_3 edge with the $E2$ electric-quadrupole transition was performed on the 6-ID-B beamline at the APS (Wang *et al.*, 2017), but no evidence of multipolar moments was found within the experimental uncertainty.

B. General trends in REXS studies

The large enhancement of the magnetic signal at the actinide M edges has also been of interest in many actinide

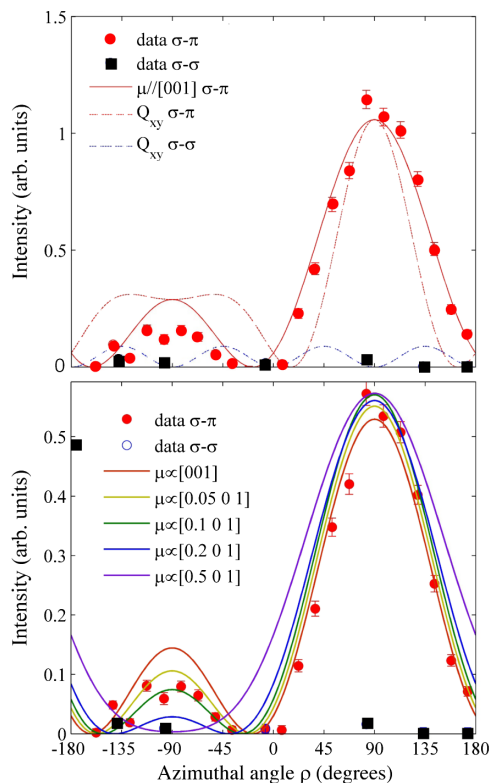


FIG. 16. Top panel: azimuthal dependence of the (201) Bragg reflection in URu_2Si_2 . Solid (red) circles, $\sigma\pi$ channel; black squares, $\sigma\sigma$ channel. The solid (red) line is the theoretical intensity variation for magnetic dipoles ordered along [001]. The dashed red (dashed blue) line is the $\sigma\pi$ ($\sigma\sigma$) ρ dependence of the intensity expected for xy quadrupole order. Bottom panel: experimental data compared with theoretical predictions for a dipole magnetic moment with an increasing component in the a - b crystallographic plane. Adapted from Walker, Caciuffo *et al.*, 2011.

materials for learning more about the magnetic structure itself. Early work determined in greater detail the nature of the multi- \mathbf{k} structures found in materials with transuranium ions (Langridge *et al.*, 1994a, 1994b; Lidström *et al.*, 2000; Normile *et al.*, 2002a, 2002b), as well as those with uranium (Longfield *et al.*, 2002; Bernhoeft, Paixão *et al.*, 2004), and thin films (Bernhoeft *et al.*, 1998; Bao *et al.*, 2013).

Some important progress was made with REXS on the question of multi- \mathbf{k} magnetic configurations, which are frequently found in actinide systems. Experiments showed that for more than a single \mathbf{k} vector a satellite related to the third term in Eq. (66) occurred in the magnetic diffraction pattern at the positions described by the vectors $\langle k_1, k_2, 0 \rangle$ added to any allowed magnetic lattice point, thus uniquely identifying either a $2\mathbf{k}$ or $3\mathbf{k}$ magnetic configuration with a term that is quadrupole in nature representing the coupling of components (Longfield *et al.*, 2002). For the $3\mathbf{k}$ systems additional satellites were found at the positions $\langle k_1, k_2, k_3 \rangle$ added to any allowed lattice point, but the scattering process giving rise to these peaks, which appears to be dipole in nature, is not completely clear (Bernhoeft, Paixão *et al.*, 2004; Detlefs *et al.*, 2007). These weak magnetic peaks, which have been called $\langle kkk \rangle$ peaks, were also observed in a landmark experiment using neutrons. Such experiments prove the

existence of the $3\mathbf{k}$ magnetic configuration and confirm the dipole nature of the scattering, although the momentum dependence is not presently understood (Blackburn and Bernhoeft, 2006; Blackburn *et al.*, 2006). Such weak peaks cannot be observed in systems such as UO_2 or USb , which both have $3\mathbf{k}$ configurations with $|k| = 1$, because they are superimposed on strong lattice reflections.

The large intensity also allowed experiments to show that the magnetic ordering in URu_2Si_2 was not fully long-range (Isaacs *et al.*, 1990), and to probe surface magnetism in UO_2 showing new examples of surface ordering not previously measured (Watson *et al.*, 1996, 2000; Langridge *et al.*, 2014).

An experiment was also performed early on at the Synchrotron Radiation Source (SRS) at Daresbury Laboratory in England, showing that there is enough intensity at the resonant $\text{U } M_4$ energy to observe the antiferromagnetic peaks in a polycrystalline sample of UO_2 (Collins, Laundy, Tang, and Cernik, 1995). This technique has not been used for other actinide antiferromagnets, perhaps because the moment cannot be reliably determined by this method, or because the momentum resolution is necessarily poor to obtain the intensity needed to observe the peaks. An attempt to use this method was made with Cm (Lander *et al.*, 2019) but failed, as the sample had lost its crystallinity due to self-radiation. One scattering experiment has also been performed at the uranium $L_{2,3}$ edges, where the enhancement is relatively weak (Wermeille *et al.*, 1998).

Similarly, the large intensity led to the discovery of an interesting effect that appears to occur when a magnetic material disorders, namely, a small apparent shift in the position of the peak arising from the disordered diffuse scattering. This is not caused by the diffuse scattering becoming incommensurate, which would result in the appearance of two peaks at about the commensurate position. No satisfactory explanation of this effect has yet been proposed (Bernhoeft, Lander *et al.*, 2004). After considerable effort this small effect was also seen with neutrons in the antiferromagnet MnF_2 , showing that it is not limited to actinides and is not related to a surface effect (Prokeš, Lander, and Bernhoeft, 2009).

Resonant scattering effects also occur in other atoms whose electrons interact with the magnetic dipoles (or electric quadrupoles) of the actinide ions. This was first observed in the relatively simple antiferromagnets UGa_3 and UAs (Mannix *et al.*, 2001). Below the ordering temperature T_N when the x-ray energy is tuned to the K edge of Ga or As, a large signal is present and disappears at T_N . Similar observations were made at the Ga K edges in UTGa_5 ($T = \text{Ni, Pd, and Pt}$) (Kuzushita *et al.*, 2006), as well as in NpRhGa_5 and NpCoGa_5 (Detlefs, Wilkins *et al.*, 2008).

Figure 17 shows the azimuthal dependence of the signal at the As K edge in UAs . It completely agrees with the known magnetic structure for UAs , and thus suggests that a small moment appears on the As ions. The signal arises from the hybridization of the actinide $5f/6d$ and anion $2p$ states and results in a small polarization of the $2p$ anion electrons, thus appearing as a “magnetic moment.” This would not occur if the $5f$ states were fully localized. It is not yet possible to relate the size of the signal to any magnetic moment, either for the active ions themselves or for induced effects such as those

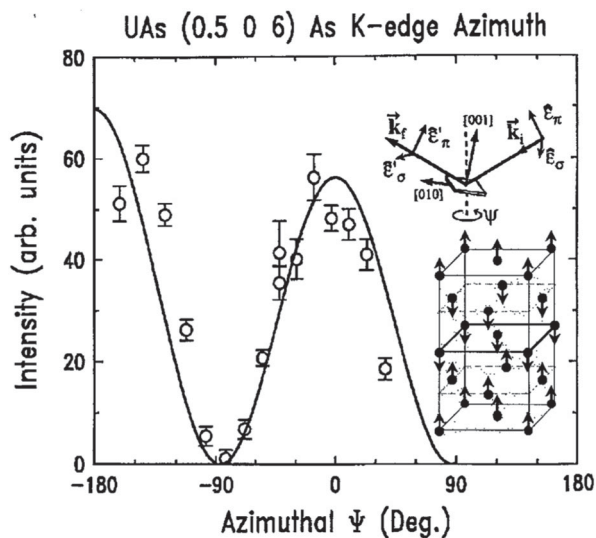


FIG. 17. Measurements at the As K edge of the integrated intensity in the $\sigma\pi$ channel of the $(0.5, 0, 6)$ reflection in UAs at $T = 20$ K as a function of the azimuthal angle around the normal to the $[001]$. Insets: geometry and schematic of the Fourier component of the magnetic structure of UAs giving rise to this reflection, where the propagation vector of the structure is $[100]$. The azimuthal angles $\Psi = 0^\circ$ and 180° correspond to the $[100]$ axis lying in the scattering plane, which are defined by incident and scattered wave vectors \mathbf{k} and \mathbf{k}' , respectively. From Mannix *et al.*, 2001.

measured here. Sanchez *et al.* (2000) used Mössbauer spectroscopy to suggest that the induced polarizations of the $2p$ electrons give a net moment of the order of $0.02\mu_B$ at the Ga site in UGa_3 . There have also been theoretical papers explaining these large resonances on nonmagnetic ions (van Veenendaal, 2003; Usuda, Igarashi, and Kodama, 2004).

At resonant energies additional scattering effects can be observed that are not connected to magnetism. An early example was reported by Templeton and Templeton (1994), followed by observations in other systems, as summarized by Kokubun and Dmitrienko (2012). Resonant scattering depends on the energy as well as the x-ray polarization, where the scattering factor must be treated as a tensor quantity. The effects can be observed in crystals with screw axes or glide planes, but are not observable in higher symmetry systems such as UO_2 . Thus far almost all the effects have been observed at transition-metal K edges, but these are often difficult to understand, as the absorption process involves both an $s \rightarrow p$ transition in the dipole channel ($E1$) and an $s \rightarrow d$ transition in the quadrupole channel ($E2$), complicating the interpretation. However, in the cubic compound U_2N_3 Lawrence Bright *et al.* (2019) found the first example of Templeton scattering involving the M_4 U resonance. This transition is $3d \rightarrow 5f$ and is certainly an $E1$ transition, as the quadrupole transition is to possible g states with a small matrix element. These forbidden reflections are independent of temperature and give information about the bonding in the system.

The large enhancement of the magnetic scattering at the U M_4 edge allows one to measure magnetic Bragg peaks with good statistics even when a pinhole aperture is used to

increase the transverse coherence length of the beam up to tens of micrometers. This is necessary to perform speckle spectroscopy, i.e., x-ray photon correlation spectroscopy (XPCS). This technique uses the intensity-intensity time correlations between coherently diffracted x rays to access dynamics on the $10^{-6} - 10^3$ s timescales (Grübel and Zontone, 2004). Pioneering studies were performed at the ESRF on UAs (Yakhou *et al.*, 2001) and at the Diamond Light Source on the isostructural compound USb (Lim *et al.*, 2014). The latter is a longitudinal $3k$ antiferromagnet, with $T_N = 218$ K and spins pointing along local $\langle 111 \rangle$ -type directions, with three equivalent wave vectors of the form $[001]$ (Jensen and Bak, 1981; Caciuffo *et al.*, 2007). Inelastic neutron scattering experiments showed that the spin-wave energy in USb softens when a temperature $T^* = 160$ K is approached, and no collective excitations are observed for $T^* < T < T_N$ (Hagen, Stirling, and Lander, 1988; Lim *et al.*, 2013), although the magnetic Bragg peaks appear to be unaffected by the change in dynamics. The XPCS results reported by Lim *et al.* (2014) reveal a change in the static and dynamical speckle patterns that show an increase in fluctuations and decrease in domain size around T^* , suggesting that changes in the magnetic domain structure can be at the origin of the observed anomalous behavior.

VI. XAS EXPERIMENTS

XAS of actinides at SR sources started in the late 1980s and have explored both the $L_{2,3}$ ($2p \rightarrow 6d$) (Kalkowski, Kaindl, Bertram *et al.*, 1987; Bertram *et al.*, 1989) and the $M_{4,5}$, $N_{4,5}$, and $O_{4,5}$ ($nd \rightarrow 5f$; $n = 3, 4, 5$) (Kalkowski, Kaindl, Brewer, and Krone, 1987) absorption edges. The potential of XAS for elucidating the electronic structure of actinides was immediately recognized, and a number of studies on actinide speciation in compounds and minerals followed (Silva and Nitsche, 1995; Conradson *et al.*, 1998; Denecke, 2006).

XAS experiments have provided important information about the oxidation state of actinide elements in minerals and molecular compounds, their coordination with neighboring atoms, and the structure of their local environment. The technique can be applied to samples in solid or liquid forms, including nanoparticles (Gerber *et al.*, 2020) and colloidal forms (Micheau *et al.*, 2020), with element sensitivity down to tens of ppm. In combination with SAXS measurements, XAS provides detailed information on the local structure, size, shape, and interfacial properties of atomic clusters and intrinsic colloidal particles (Nyman, 2017; Micheau *et al.*, 2020; Tian *et al.*, 2020; Zhai *et al.*, 2022).

Besides the scientific importance, actinide speciation studies are key to understanding extraction mechanisms and separation processes in fuel reprocessing (Moeyaert *et al.*, 2021; Dressler *et al.*, 2022; Pruessmann *et al.*, 2022), the corrosion and the reduction-oxidation behavior of nuclear waste forms in storage facilities (Glasauer *et al.*, 2022; Husar *et al.*, 2022), the mechanisms by which actinides can contaminate the biosphere (Pidchenko *et al.*, 2020; Vitova *et al.*, 2020; Cot-Auriol *et al.*, 2021; Estevenon *et al.*, 2021), their mobility in contaminated sites, and how they can be best removed from the environment (Le Pape *et al.*, 2020; Dumas *et al.*, 2022; Jegou *et al.*, 2022). The cleanup of the Rocky Flats Nuclear Weapons Plant near

Denver, CO, exemplifies the practical importance of these studies (Clark, Janecky, and Lane, 2006). Redox–solid-liquid interface reactions can be studied at metal ion concentrations of specific relevance for contaminated sites, as shown by Schacherl *et al.* (2022) and Schacherl, Prüssmann *et al.* (2022) who reported M_5 XAS spectra for 1 ppm Np adsorbed on clay.

Current XAS experiments at state-of-the-art spectrometers have been extended to the heaviest actinides available in macroscopic quantities, as recently demonstrated in a study of a coordination complex of ^{254}Es that used less than 200 nanograms of this highly radioactive isotope (half-life of ~ 275.7 days) (Carter *et al.*, 2021). XAS techniques, in combination with other chemical physics methods, are also assuming growing importance in the nuclear toxicology field and are enabling the development of effective actinide decorporation agents with high complexation affinity, high tissue specificity, and low biological toxicity (Ye *et al.*, 2021; Zurita *et al.*, 2021, 2022). In a recent study, XANES and x-ray fluorescence chemical imaging have been used to characterize trace impurities in fuel pellets and assess the potential of these techniques as a forensic tool for the investigation of interdicted special nuclear materials (van Veelen *et al.*, 2022).

From the point of view of physics, XAS experiments at the $M_{4,5}$ and $N_{4,5}$ absorption edges of actinides have been important to probe the relativistic nature of the $5f$ electrons, thanks to the application of simple spin-orbit sum rules relating the branching ratio of the core-valence transitions to the expectation value of the angular part of the $5f$ spin-orbit interaction per hole (Thole and van der Laan, 1988; van der Laan *et al.*, 2004; Shim, Haule, and Kotliar, 2009; Caciuffo, Buck *et al.*, 2010). The information obtained is analogous to that provided by electron-energy-loss spectroscopy (EELS) (Moore and van der Laan, 2009), a technique that has proven to be useful in elucidating the change between α and δ plutonium (Moore *et al.*, 2006), examining the magnetic stabilization in curium metal (Moore *et al.*, 2007), and studying rare metals that are available only in small quantities (Dieste *et al.*, 2019).

We now emphasize the importance of self-absorption corrections in XAS studies of actinides. These corrections should take into account the chemical composition, the density, the practically infinite thickness of the bulky sample if the fluorescence-detection mode is used, the various background contributions (fluorescence of the subshells and matrix as well as coherent and incoherent scattering), the angle of incidence of the x-ray beam, and finally the solid angle of the detector (Goulon *et al.*, 1982; Tröger *et al.*, 1992; Pfalzer *et al.*, 1999). The actinide edge–jump intensity ratio M_5/M_4 (defined as the ratio between the occupation numbers for the two spin-orbit-split core levels $j = 3/2$ and $5/2$) must be normalized according to the statistical edge-jump ratio. This ratio is equal to 1.5, which is close to the value tabulated in the XCOM tables given by Berger *et al.* (2010). A deviation of $\pm 10\%$ in the M_5/M_4 XAS edge-jump normalization would affect the branching ratio B and the $5f$ occupation numbers of the $j = 5/2$ and $7/2$ subshells by $\sim \pm 2.5\%$. A discussion of the importance of making accurate self-absorption corrections at the actinide M edges was given by Janoschek *et al.* (2015).

Calculations of attenuation lengths based on isolated-atom models (Parratt and Hempstead, 1954; Cromer and Liberman, 1970) are available for most of the elements in the periodic table, including actinides. Table I gives the attenuation length at different absorption edges of uranium. Notice, however, that data for bare atoms reproduce the gross spectral features but neglect the local environment around the resonant atom, and therefore fail to reproduce important effects such as the appearance of a large white line at the resonance energy (Bohr, Gibbs, and Huang, 1990). In actinides, these effects are dramatically large, as at the M_4 edge of uranium, where the white line is about 7.5 times larger than the step height (Cross *et al.*, 1998). For the $M_{4,5}$ edges, where the transitions involve the partially occupied $5f$ states, Cross *et al.* (1998) suggested that the attenuation length including the white line is ~ 100 nm for the M_4 , and only ~ 50 nm for the M_5 edge. Similar reductions would be expected for the $N_{4,5}$ and $O_{4,5}$ edges listed in Table I, with an attenuation length at the U $N_{4,5}$ edges of the order of 10 nm, as provided by calculations based on the COWAN code (Cowan, 1981). Computer codes for general-purpose *ab initio* calculations of the attenuation lengths for embedded atoms are available. An example is the FEFF code (Rehr *et al.*, 1991; Zabinsky *et al.*, 1995), which takes into account both atomic and photoelectron scattering contributions from the neighboring atoms, providing a dramatic improvement in the simulation of the resonant spectral features for actinides (Cross *et al.*, 1998).

A. Examples of XAS studies on actinide systems

An example of work at the Pu L_3 edge, which is far easier to work at than at the lower energy M edges (given that the samples must be at least doubly encapsulated), is shown in Fig. 18 (Conradson *et al.*, 2004a; Joyce and Lander, 2019).

The L_3 absorption edge involves a transition from the $2p$ core states to the unoccupied $6d$ states around the Pu atom. The energy sensitivity of the observed spectra comes because the screening of the $6d$ hole depends on the number of $5f$ electrons in the partially occupied $5f$ shell. In Fig. 18(a) there are no $6d$ electrons present in any of the ionic materials, so this gives a simple interpretation of the energy shift of the Pu L_3 maximum. On the other hand, in Fig. 18(b) we show a number of spectra from the metal and other semimetallic compounds, and within experimental error they all have approximately the same peak value. This shows that the simple interpretation of ionic complexes [Fig. 18(a)] cannot be used for the intermetallics [Fig. 18(b)], as the presence of a conduction band containing *spd* partially occupied states complicates the simple interpretation that is useful in Fig. 18(a). One can also observe in Fig. 18 that the spectral linewidths are considerable. This arises from the short core-hole lifetime of the $2p_{3/2}$ state, which results in spectral full width at half maximum (FWHM) of at least 7.5 eV.

There are two ways to improve this resolution. The first is to move to the actinide M edges, which directly involve the $5f$ electrons and is where the intrinsic lifetimes give a resolution of FWHM ~ 3.3 eV. A difficulty with working at these energies is that the x-ray beam is strongly absorbed in air. The second way to improve the resolution is to construct a spectrometer that analyzes specific emission lines, for

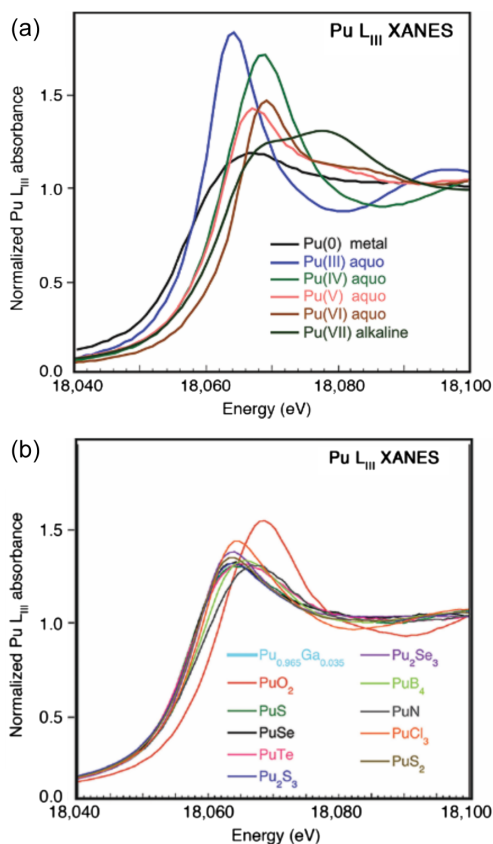


FIG. 18. Pu L_3 edge XANES (normalized absorbance) for a series of plutonium molecules and compounds in different formal oxidation states. (a) Gallium stabilized δ -Pu metal compared to the plutonium aqua ions in oxidation states III–VI and the Pu(VII) oxohydroxide. The spectra of Pu(0)–Pu(VI) are replotted from the original data reported by [Conradson *et al.* \(2004a\)](#), and data for Pu(VII) in a 2M NaOH solution are courtesy of M. Antonio of ANL. (b) The peak amplitude of the δ -Pu alloy is suppressed by self-absorption in this opaque sample. The XANES spectra of gallium stabilized δ -Pu metal is compared to a number of binary plutonium compounds, including PuO_2 , which represents Pu(IV). Adapted from [Conradson *et al.*, 2004a](#), and [Joyce and Lander, 2019](#).

instance, the M_β ($4f_{5/2} \rightarrow 3d_{3/2}$) one. The total spectral width may then be reduced to below 1 eV, as shown by [Kvashnina *et al.* \(2013\)](#) and [Kvashnina and Butorin \(2022\)](#). The resulting spectra are then referred to as HERFD XANES and are shown in Fig. 19 for some of the oxides of uranium. Notice that conventional XAS essentially integrates over all outgoing channels. By selectively detecting outgoing channels with a limited opening angle to gain a linewidth narrowing, one measures something other than XAS, and the results will depend on the specific edges used because of selection rules and final-state effects ([Carra, Fabrizio, and Thole, 1995](#)). For instance, for most actinide dioxides, good agreement between XAS and HERFD spectra is found at the M_4 edge, whereas additional transitions at the M_5 edge produce different spectral profiles for XAS and HERFD measurements ([Butorin, 2020](#)). An M_4 edge demonstrates better overall agreement between the HERFD and XAS spectra.

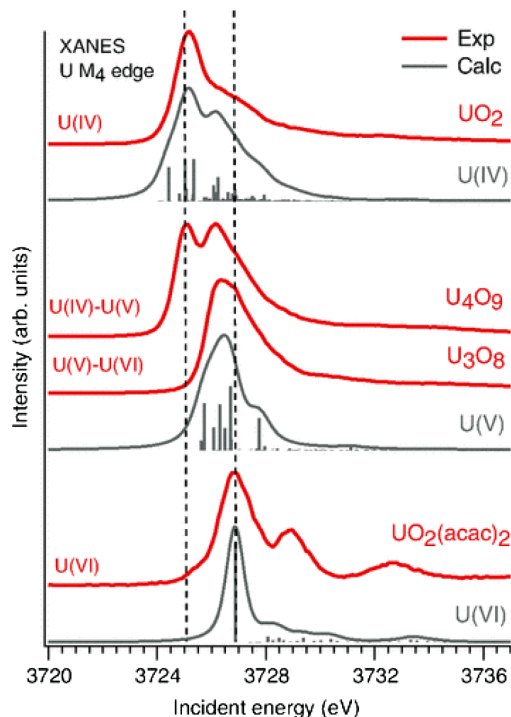


FIG. 19. Experimental and calculated HERFD-XANES spectra at the U M_4 edge of U_4O_9 and U_3O_8 compared to those of the reference systems UO_2 and $\text{UO}_2(\text{acac})_2$. The dashed lines indicate the energy position of the main peaks corresponding to uranium(IV) and uranium(VI), respectively. From [Kvashnina *et al.*, 2013](#).

This work shows a clear shift of ~ 2 eV from U(IV) to U(VI) with a resolution of ~ 1 eV ([Kvashnina *et al.*, 2013](#)). Somewhat more information may be obtained by multiedge measurements ([Bes, Leinders, and Kvashnina, 2022](#)) and by examining the full diagram of the incident energy versus the emitted energy ([Kvashnina and Butorin, 2022](#)), but for intermetallic systems the same problems arise, as evident in the early work on Pu systems (see Fig. 18), despite the much higher resolution now achieved with better M -edge spectrometers ([Kvashnina *et al.*, 2017](#)). Notably these results for uranium oxides agree well with an alternative technique used in x-ray photoelectron spectroscopy at the core $4f$ emission lines ([Ilton and Bagus, 2011](#); [Gouder, Eloidri, and Caciuffo, 2018](#)).

The high sensitivity of HERFD XANES to the arrangement of atoms around the absorber is demonstrated by measurements at the U M_4 edge in hexavalent uranium in various local configurations ([Amidani, Retegan *et al.*, 2021](#)) and at the thorium M_4 edge in ThO_2 nanoparticles (NPs) ([Amidani, Vaughan *et al.*, 2021](#)). These experiments indicate the possibility of correlating spectral details with local symmetry breakdowns around the absorbing atoms sitting close to the NP surface.

Absorption spectroscopy may also give valuable information if performed at the anion K edges, for instance, oxygen, carbon, or chlorine. At the oxygen K edge (532 eV), polarized x-ray absorption and emission spectra have been reported for a single crystal of $\text{Cs}_2\text{UO}_2\text{Cl}_4$ ([Denning *et al.*, 2002](#)). The absorption data led to the assignment of the relative energies

of the empty molecular orbitals and of their character (mainly uranium $5f$ and $6d$). The emission spectra provided the energy of excitations to these orbitals from filled valence-shell orbitals, showing that valence excitations from the σ_u occupied valence orbitals occur at substantially lower energies than those from the σ_g , π_g , and π_u orbitals. The presence of a charge-transfer transition in emission established the participation of the pseudocore $6p$ shell in the covalent bonding, with a strong hybridization between the $5f_\sigma$ and $6p_\sigma$ states. Other examples at the oxygen K edge were reported for PuO_2 (Modin *et al.*, 2011) and for uranium systems (Kvashnina and Butorin, 2022). At the chlorine K edge (2822 eV), Minasian *et al.* (2012) studied the relative f and d orbital contributions to the U-Cl covalency in UCl_6^{2-} and UOCl_5^- . An example at the carbon K edge (284 eV) was given in the study of $5f$ covalency in $[\text{U}(\text{C}_7\text{H}_7)_2]^-$ reported by Qiao *et al.* (2021). These spectra are complex and cannot be interpreted without substantial modeling, but they give important information on covalency (Ganguly, Sergentu, and Autschbach, 2020; Sergentu and Autschbach, 2022).

Tobin, Yu, Booth *et al.* (2015) used spectroscopy at the L_3 edge and also measured branching ratios at the $N_{4,5}$ edges using soft x rays at the ALS and found that UO_2 has an f^2 configuration (which is expected) and UO_3 has an f^1 configuration (which is unexpected), as a straightforward valence argument would expect a U(VI) valency, and hence f^0 . Although UO_3 was not specifically examined in the HERFD work of Kvashnina *et al.* (2013), a number of such oxides were examined by x-ray core-hole photoemission, and there appears to be strong evidence that UO_3 consists of hexavalent U atoms (Ilton and Bagus, 2011). Work has also been reported on the branching ratios of UF_4 , UO_2 , and UCd_{11} systems at the $M_{4,5}$ edge, with a view to determining the occupied and unoccupied densities of states (Yu *et al.*, 2011; Tobin, Yu, Qiao *et al.*, 2015; Tobin *et al.*, 2019, 2021).

Absorption spectroscopy has also played an important role in probing the electronic structure of Pu metal. Terry *et al.* (2002) reported on early experiments on the absorption at the $O_{4,5}$ edge (involving $5d \rightarrow 5f$ transitions) in both the α -Pu and δ -Pu forms, which were taken at the ALS using soft x rays. These experiments have been analyzed in different ways through discussions of the electronic structure of Pu (Tobin *et al.*, 2003, 2005, 2008). This is a complex subject that needs the results of experiments using photoemission, EELS, XPS core-level spectroscopy, and even neutron inelastic scattering. Moore and van der Laan (2009) and Joyce and Lander (2019) covered this subject in depth.

High-energy-resolution XANES spectra have been measured at the Pu M_5 edge in PuO_2 (Vitova *et al.*, 2013, 2018; Bahl *et al.*, 2017; Bagus, Schacherl, and Vitova, 2021) at the CAT-ACT wiggler beamline at KARA (Zimina *et al.*, 2017) and the Pu $M_{4,5}$ edges at the ESRF (Kvashnina *et al.*, 2019). Bagus, Schacherl, and Vitova (2021) used fully relativistic quantum chemical computations of the electronic structure of the isolated Pu^{4+} cation and some for Pu^{4+} in PuO_2 for an interpretation of the experimental spectra, thereby giving insight into the level of covalency of the Pu $5f$ valence orbitals and their role in chemical bonding. Bagus, Schacherl, and Vitova emphasized the need to take many-body effects

into account to properly describe the wave functions for both the initial and excited states of the XANES transitions. They showed that a single-determinant representation of the Pu states is not a sufficient approximation for calculating the Pu $M_{4,5}$ XANES spectra, which implies that dipole-selection rules must be applied between the total wave functions for the initial and excited states. The spectral broadening due to the angular momentum coupling of the open-shell electrons dominates over spin-orbit and ligand field splittings of the $5f$ shell orbitals. As a consequence, energy splittings and energy shifts of the excited multiplets in PuO_2 are similar to those calculated for the isolated Pu^{4+} cation, and the predicted $M_{4,5}$ edges for the two cases are similar. Furthermore, it appears that both the M_4 - and M_5 -edge XANES spectra probe mainly $J = 7/2$ states, and that the Pu-O bond covalency does not change between the ground and excited configurations (Bagus, Schacherl, and Vitova, 2021). The possibility of exploiting HERFD XANES to probe crystal fields and covalency effects in actinide compounds was discussed by Butorin, Kvashnina, Smith *et al.* (2016), Butorin, Kvashnina, Vegelius *et al.* (2016), and Butorin (2020). Many of the techniques proposed are interesting, but they probably need better resolution before they can match standard RIXS techniques at the M and N edges (Butorin, Modin *et al.*, 2016; Kvashnina and Butorin, 2022).

Recently HERFD-XANES measurements at the Pu M_4 and L_3 absorption edges, combined with theoretical calculations, were used to investigate the formation of PuO_2 NPs from oxidized Pu(VI) under alkaline conditions, revealing the formation of a stable intermediate Pu(V) solid phase similar to $\text{NH}_4\text{PuO}_2\text{CO}_3$ (Kvashnina *et al.*, 2019). Further studies reported on by Gerber *et al.* (2022) showed that the Pu(IV) oxidation state dominates in all NPs formed at pH 1–4, with Pu(III) and Pu(VI) present in addition to Pu(IV) due to the redox dissolution of PuO_2 NPs under acidic conditions. The results of these studies are important for a better understanding of the colloid-facilitated transport governing the migration of plutonium in a subsurface environment.

B. Examples of EXAFS studies on actinides

EXAFS has been useful to the actinide community as a tool for probing *in situ* gas, solution (liquid), or solid phases. An extensive review on earlier studies was given by Shi *et al.* (2014). As mentioned, beamlines at synchrotrons have been constructed to exploit this technique for actinide materials (Dardenne *et al.*, 2009; Solari *et al.*, 2009; Zimina *et al.*, 2017; Scheinost *et al.*, 2021). An example of the power of the technique was given by Clark, Janecky, and Lane (2006). The main reason for its success is that the actinides, with so many electrons, give a strong signal, so small quantities can be successfully examined (Carter *et al.*, 2021). For the most part, EXAFS tackles materials that are of interest to chemistry and materials science problems concerning nuclear fuel and nuclear waste disposal (Richmann *et al.*, 2001; Hubert *et al.*, 2006; Walter *et al.*, 2008; Nastren *et al.*, 2009; Degueldre *et al.*, 2011, 2013; Gaona *et al.*, 2013; Prieur *et al.*, 2013; Ding *et al.*, 2021), molten salts (Volkovich *et al.*, 2005; Smith *et al.*, 2019), and extraction chemistry (Antonio *et al.*, 2001; Bolvin *et al.*, 2001; Skanthakumar *et al.*, 2007; Ikeda-Ohno *et al.*,

2008; Boubals *et al.*, 2017; Ferrier *et al.*, 2018; Bhattacharyya and Mohapatra, 2019). Nevertheless, studies of interest to condensed-matter physics are not rare. For instance, Bridges *et al.* (2020) reported the results of an EXAFS investigation of the local structure of Fe-doped URu_2Si_2 , suggesting the occurrence of a local orthorhombic distortion with B_{1g} -like symmetry below 80–100 K, and Booth *et al.* (2007) used EXAFS to characterize the structural damage from self-irradiation in the plutonium unconventional superconductor PuCoGa_5 . A history of the early years (Lytle, 1999) showed that all original work dating back to the 1920s has relied on physics, but (as is so often the case) once the technique and analysis are developed, the main applications are in other condensed-matter subfields.

Here we consider an important question that has concerned the actinide community for at least 50 years. What is the distribution of oxygen and uranium atoms in the series of materials characterized by the formula UO_{2+x} (where $0 < x < 1$)? Although there were earlier papers on this subject, the best summary of earlier work was given by Willis (1987). Since no new diffraction peaks are observed for samples up to $x = 0.25$, these samples have disordered oxygen atoms, and the subsequent short-range order of these O atoms (and any accompanying relaxation of the nearest U atoms) are then ideal problems for the EXAFS technique. Willis had previously proposed a series of clusters (the so-called 2:2:2 cluster proposed for $x = 0.12$ being the most famous); this was discussed in a more recent paper using theoretical modeling (Wang, Ewing, and Becker, 2014). At $x = 0.25$ the compound U_4O_9 is formed, and that structure was reported on by Bevan, Grey, and Willis (1986) and in a second modification by Cooper and Willis (2004). None of these structures have a U–O distance less than ~ 2.2 Å, whereas in the cubic fluorite structure (UO_2 , $x = 0$) the shortest U–O distance is 2.37 Å.

In a series of papers using EXAFS (at the actinide L_3 edges) and pair distribution function methods (using data taken with neutron diffraction) as the primary analysis technique, Conradson *et al.* (2004b, 2005, 2013) and Conradson, Manara *et al.* (2004) claimed that there are unusual aspects of the UO_{2+x} and PuO_{2+x} systems that had not been previously observed. There is much in these papers that is beyond the scope of this review, but (for $x > 0$) essential features on which we concentrate here are the proposed U–O bond of < 2 Å and the amorphouslike nature of a part of the sample. Since the U–O distance in UO_2 is $\sqrt{3}a_0/4 = 2.37$ Å (where a_0 is the lattice parameter), a U–O distance of < 2 Å represents a major structural change and was not reported for any previous work on the UO_{2+x} system; see the recent modeling work given by Wang, Ewing, and Becker (2014). This short bond was ascribed to some U atoms having a f^0 (U^{6+}) configuration, as the uranyl-type U–O bond is 1.97 Å. In addition, for PuO_{2+x} (Conradson *et al.*, 2004b) the nearest-neighbor O atoms were found in a multisite distribution, with the excess O at Pu–O distances < 1.9 Å. This was attributed to multiply bound oxo-type ligands, such as those found in molecular complexes of Pu(V) and Pu(VI) (Conradson *et al.*, 2004b).

More recent work has questioned both of the premises emerging from the previously discussed EXAFS work. First, recall that in the range $0 < x < 0.20$ the samples are only single phase at temperatures above ~ 673 K, and that below this temperature the sample will consist of mixtures of UO_2 and U_4O_9 ($x = 0.25$). Second, using neutron diffraction Garrido *et al.* (2006) showed that by carefully analyzing a sample of U_4O_9 neither of these two premises was correct. Further evidence comes from Palomares *et al.* (2019), who again used neutron diffraction of $\text{UO}_{2.07}$, with data taken at between 873 and 1273 K, showing that, although the O–O distance does approach 2 Å for the solid solutions, the closest U–O distance remains above 2 Å and is close to that in UO_2 . These short O–O distances are key features of the Willis clusters (Willis, 1987). In the case of PuO_{2+x} , the short Pu–O distance (< 1.9 Å) has been attributed to multielectron excitation effects in the EXAFS spectra (Rothe *et al.*, 2004).

Leinders *et al.* (2020) published an exhaustive study of U_3O_7 ($x = 0.33$) using HERFD XANES at both the L and M edges, as well as EXAFS at the L edges. They were able to determine the different uranium valencies in these materials with $x > 0$, and that the U–O bonds were spread over values ranging from 2.25 to 2.80 Å; see Fig. 20. The valencies for the U atoms are almost 50% each of U^{4+} and U^{5+} for $x = 0.33$, and there is no sign of U^{6+} . These results are in agreement with those given by Kvashnina *et al.* (2013); see Fig. 19, where it is clear that the U^{6+} state first appears in U_3O_8 ($x = 0.67$).

Finally, various EXAFS studies have been dedicated to the characterization of the local structure in actinide NPs and colloids (Hudry *et al.*, 2014; Dalodière *et al.*, 2017; Plakhova *et al.*, 2019; Bonato *et al.*, 2020; Gerber *et al.*, 2020, 2021; Micheau *et al.*, 2020). EXAFS spectra on PuO_2 and CeO_2 NPs, measured at the Structural Materials Science beamline (Chernyshov, Veligzhanin, and Zubavichus, 2009) of the Kurchatov Synchrotron Radiation Source (Moscow, Russia), were reported on by Romanchuk *et al.* (2022), who

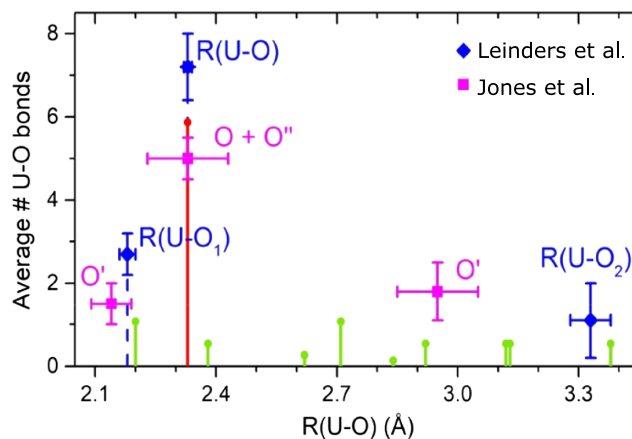


FIG. 20. Distribution of U–O bonds in the average unit cell of U_3O_7 at 18 K. The structural model assumes a regular geometry of cubo-octahedral oxygen clusters. The histograms in red and green correspond to fluorite-type and additional U–O bonds, respectively. The blue diamonds and magenta squares are EXAFS results reported on by Leinders *et al.* (2020) and Jones *et al.* (1986), respectively. From Leinders *et al.*, 2020.

discussed a new core-shell model for NPs and studied size effects on oxygen disorder and the metal-metal coordination number.

C. Examples of XMCD studies on actinides

XMCD is associated with time-reversal symmetry breaking by a magnetic field and involves electric-dipole or electric-quadrupole transitions promoting an electron in a spin-orbit split core state to an empty valence state of the absorbing atom. The technique provides an element- and shell-specific probe for studying the electronic structure of a wide range of materials (van der Laan, 2013; van der Laan and Figueroa, 2014; Rogalev and Wilhelm, 2015). In actinide materials, XMCD spectra are conveniently measured at the $M_{4,5}$ ($3d_{3/2,5/2} \rightarrow 5f$) absorption edges that directly interrogate the $5f$ shell. The XMCD signal is obtained as the difference $\Delta I_{M_{4,5}} = \mu^-(E) - \mu^+(E)$ of the absorption spectra of circularly polarized photons with helicity parallel [$\mu^+(E)$] and antiparallel [$\mu^-(E)$] with respect to a magnetic field applied along the incident beam direction. The spectra must be corrected for self-absorption effects and for the incomplete polarization of the incident beam emerging from the crystal monochromator. Standard protocols have been developed for performing such corrections (Goulon *et al.*, 1982; Tröger *et al.*, 1992; Pfalzer *et al.*, 1999).

The power of the technique comes from the simplicity of the sum rules relating orbital $\langle L_z \rangle$ and spin $\langle S_z \rangle$ moments of the absorbing atoms to linear combinations of the dichroic signals integrated over the spin-orbit-split absorption edges, normalized to the isotropic x-ray absorption spectrum (Thole *et al.*, 1992; Carra *et al.*, 1993; van der Laan and Thole, 1996; van der Laan *et al.*, 2004). The orbital and spin sum rules are given in Eqs. (29) and (30), respectively. The orbital and spin components of the total magnetic moment of the $5f$ shell $\mu = -(\langle L_z \rangle + 2\langle S_z \rangle)$ can then be obtained from XMCD spectra, together with an estimate of $\langle T_z \rangle$, if the value of the total moment μ and the occupation number of the $5f$ shell are known.

Furthermore, the expectation value of the angular part of the valence states' spin-orbit operator ($\langle \psi | \boldsymbol{\ell} \cdot \mathbf{s} | \psi \rangle$) can be obtained from the XAS branching ratio $B = \rho_{M_5} / (\rho_{M_5} + \rho_{M_4})$, using Eq. (28), as (Thole and van der Laan, 1988)

$$\frac{2\langle \boldsymbol{\ell} \cdot \mathbf{s} \rangle}{3n_h} - \Delta = -\frac{5}{2} \left(B - \frac{3}{5} \right), \quad (71)$$

where Δ is a correction factor dependent on the electronic configuration (van der Laan *et al.*, 2004) (for Np^{3+} , for instance, $\Delta = -0.005$). Equation (71) has also been used to determine the f counts of various actinides (Moore and van der Laan, 2009).

The presence of orbital moments in actinide systems was recognized many years ago, but the coupling scheme between the spin and orbital components was controversial for many years. Whereas this is known to follow Russell-Saunders coupling for the lanthanide $4f$ systems, there was some question as to whether this would be the case for the $5f$ states in the actinides, where the spin-orbit coupling is larger than in the lanthanides, or whether it would follow the

intermediate regime or even the jj scheme. XMCD promised to be a tool that would be able to resolve this question, so relatively early on a number of experiments were undertaken. At that time, the only experimental method that could give information on the orbital and spin contributions was neutron scattering, and it relied on a model (for the magnetic form factor) to resolve the components (Lander, 1993). The XMCD method is certainly more direct and does not require single crystals, as is the case with neutron scattering, but it does have the drawback that, although the orbital moment can be determined directly, the deduction of the spin moment requires the value of $\langle T_z \rangle$ [see Eq. (30)], which can in principle be determined by measuring the angular dependence of the XMCD (Stöhr and König, 1995; van der Laan, 1998a).

The first XMCD experiments on actinides were done on ferromagnetic US at the Daresbury SRS and discussed by Collins, Laundry, Tang, and van der Laan (1995). They showed results consistent with those obtained with neutron scattering, but it was not easy from either measurement to determine whether the configuration was $5f^2$ or $5f^3$. Earlier neutron results had shown a peculiar situation for the U atom in the compound UFe_2 (cubic Laves phase), where there appeared to be an almost complete cancellation between the orbital and spin moments of the $5f$ states, so the resulting moment was small (Wulff *et al.*, 1989). This spurred a number of XMCD efforts, but work at both the $M_{4,5}$ (Finazzi *et al.*, 1997) and $N_{4,5}$ edges (Okane *et al.*, 2004, 2006a) confirmed the neutron results. The effect is thought to occur via a strong mixing of the Fe $3d$ and U $5f$ states, and a consequent reduction in both the iron and uranium moments, with the U orbital moment severely suppressed (Antonov, Harmon, and Yaresko, 2003).

Many other U ferromagnets have been examined (Dalmas de Réotier *et al.*, 1997; Dalmas de Réotier, Sanchez, and Yaouanc, 1998; Kernavanois, Dalmas de Réotier *et al.*, 2001; Butchers *et al.*, 2015; Taupin *et al.*, 2015), as have heavy-fermion compounds (Yaouanc *et al.*, 1998; Dalmas de Réotier *et al.*, 1999) and compounds of the formula 1:1:1, such as UTAl , with T = transition metal (Kučera *et al.*, 2002; Antonov *et al.*, 2003; Taupin *et al.*, 2015), and there was an effort to compare the observed orbital and spin moments, and their ratio, to results from band-structure calculations. Results were also reported using the $N_{4,5}$ edges from the SPring-8 synchrotron (Okane *et al.*, 2004, 2006a, 2006b, 2008). A major difficulty with using such low-energy photons (< 1 keV) is that the self-absorption corrections are larger than they are at the $M_{4,5}$ edges, and thus more difficult to make.

We show in Fig. 21 the results from the study of UGe_2 (a ferromagnetic superconductor at modest pressure) studied at SPring-8 (Okane *et al.*, 2006a). The results showed that the U ion was in an $5f^3$ state, in agreement with an extensive neutron investigation reported previously (Kernavanois, Grenier *et al.*, 2001). For more on UGe_2 see the discussion of the theory of XMCD given by Shick *et al.* (2004). Note that this use of the sum rules at the $N_{4,5}$ edges implicitly assumes that the spin-orbit splitting of the core $4d$ level, which is ~ 50 eV, is far larger than other interactions, including the core-valence Coulomb and exchange interactions. This is certainly the case with the $M_{4,5}$ edges, where the $3d$ core levels are split by ~ 200 eV, but Shick *et al.* showed that any correction at the N edges is less than 5%.

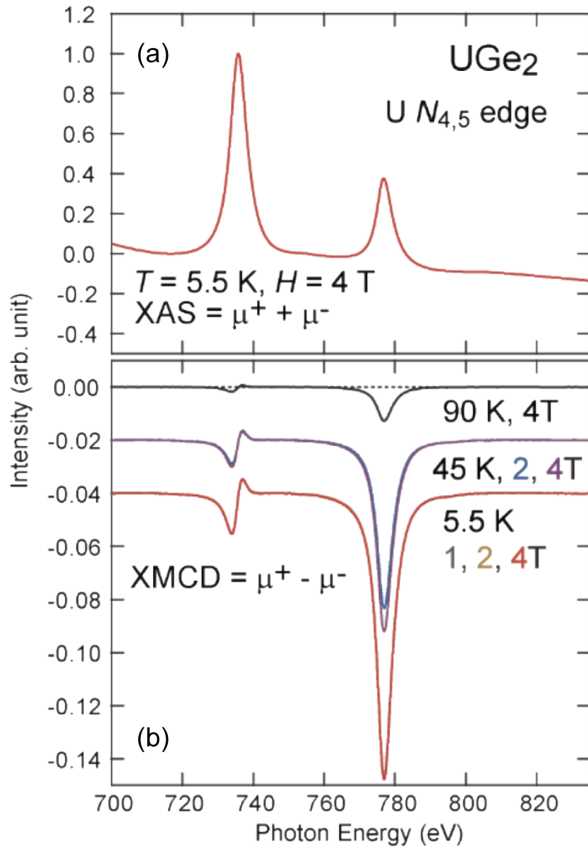


FIG. 21. (a) XAS spectra of UGe_2 measured at the U $N_{4,5}$ absorption edges at 5 K in a magnetic field of 4 T. (b) XMCD signal measured at different temperatures and applied magnetic fields. From Takeda *et al.*, 2018.

XMCD has been used as a general tool for understanding the magnetism in a number of actinide systems. Early work showed the sensitivity to small amounts of material in multilayers of U/ T , where $T = \text{Fe, Co, Ni, and Gd}$ (Wilhelm *et al.*, 2007; Springell *et al.*, 2008). An induced moment ($\sim 0.1\mu_B$) was found on the U atom in U/Fe multilayers, but an even smaller moment was found on the U atoms in the other ferromagnetic systems. This can be understood by considering the overlap of the bands of the T atoms with the uranium $5f$ density of states. In the case of U/Gd the induced

moment is small but shows oscillatory behavior, whereas in the transition-metal systems the induced U moment appears to decay rapidly as the distance from the U-Fe interface increases. Wilhelm, Sanchez, and Rogalev (2018) published a review on the XMCD on U compounds at the ESRF ID12 beamline and provided more information than given here.

One of the aspects of this XMCD work was the limitation of not knowing the value of $\langle T_z \rangle$. Thus, the orbital moment can be measured uniquely, but the $\langle T_z \rangle$ operator means that only an effective $\langle S_{\text{eff}} \rangle = \langle S_z \rangle + 3\langle T_z \rangle$ can be determined from the XMCD experiment. As shown in Table II, which gives some of these values for intermediate coupling, the values of $\langle T_z \rangle$ for $5f^n$ configurations of up to three electrons are large, so it became of interest to perform experiments on transuranium materials to see whether the predicted decrease in the effect of the $\langle T_z \rangle$ term was observed to be consistent with intermediate coupling, as shown in Table II (van der Laan and Thole, 1996). As later discussed, these results on transuranium materials were successful in showing that the theory for $\langle T_z \rangle$ in intermediate coupling can be assumed to apply whether the sample is ionic or bandlike.

The XAS and XMCD experiments reviewed later were carried out at the ID12 beamline of the ESRF using samples encapsulated in an Al holder with Kapton windows of $60 \mu\text{m}$ total thickness. The cryomagnet available at ID12 affords magnetic fields up to 17 T and a base temperature of ~ 2 K. The minimum mass of the sample depends on the magnetic susceptibility of the system. For elemental curium, data have been collected on a 0.55 mg sample of ^{248}Cm (Lander *et al.*, 2019), whereas a sample mass of $16 \mu\text{g}$ was sufficient for Am in a sample of AmFe_2 (Magnani *et al.*, 2015).

Figure 22 shows an overview of the XMCD signals measured at the M_5 and M_4 edges in ferromagnetic AnFe_2 ($\text{An} = \text{U, Np, Pu, Am}$) compounds (Wilhelm *et al.*, 2013; Magnani *et al.*, 2015). These spectra are compared with the XMCD signal measured for elemental curium (Lander *et al.*, 2019). For convenience, the photon energy is set to zero at the M_5 edge and the amplitude at the M_4 edge is normalized to unity. Notice that the spectral intensity at M_4 actually becomes smaller with increasing atomic number from uranium to americium, as the number of $5f$ holes in the $j = 5/2$ subshell decreases. Moreover, in absolute units the XMCD signal for AmFe_2 is smaller than for NpFe_2 , reflecting the difference

TABLE II. Values of orbital (μ_L) and spin (μ_S) moments per atom, their ratios, and the value of the magnetic-dipole term [see Eq. (30)] $3\langle T_z \rangle$. All values are in intermediate coupling; see Table VIII of van der Laan and Thole (1996). Note that by convention the total moment $\mu = \mu_L + \mu_S$. However, as shown in Sec. III $\mu_L = -\langle L_z \rangle$ and $\mu_S = -2\langle S_z \rangle$. Notice that all values correspond to the ground J state except for the f^6 configuration. Normally, all numbers would be zero for the f^6 ground state. However, in a strong magnetic field there is mixing with the $J = 1$ excited state, and these are the values calculated (and measured) for Am^{3+} in AmFe_2 .

f^n	Configuration	μ_L	μ_S	μ_L/μ_S	$3\langle T_z \rangle$	$3\langle T_z \rangle/\langle S_z \rangle$
1	U^{5+}	+2.856	-0.714	-4.00	-1.714	+4.80
2	$\text{U}^{4+}, \text{Np}^{5+}$	+4.698	-1.397	-3.36	-2.428	+3.48
3	$\text{U}^{3+}, \text{Np}^{4+}, \text{Pu}^{5+}$	-5.571	-2.140	-2.60	-1.978	+1.85
4	$\text{Np}^{3+}, \text{Pu}^{4+}$	+5.406	-2.810	-1.92	-0.781	+0.56
5	$\text{Pu}^{3+}, \text{Am}^{4+}$	+3.885	-2.767	-1.40	+0.302	-0.22
6	Am^{3+}	+0.47	-0.94	-0.50	-0.51	-1.1
7	Cm^{3+}	+0.330	+6.343	+0.052	-0.225	-0.071

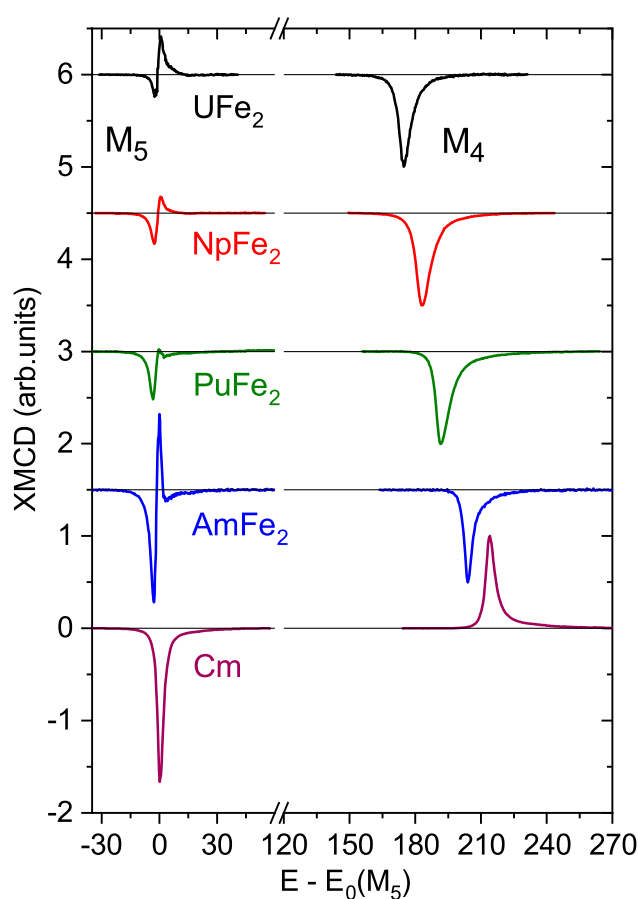


FIG. 22. XMCD spectra as a function of photon energy through the An $M_{4,5}$ edges in $AnFe_2$ ($An = U, Np, Pu, Am$) and elemental Cm. The spectra have been corrected for self-absorption effects and incomplete circular polarization of the incident beam. Adapted from Lander *et al.*, 2019.

between the magnetic moments in the two compounds, whereas the narrower linewidth of the M_4 line in $AmFe_2$ indicates the presence of localized $5f$ states, as observed in $PuSb$ (Janoschek *et al.*, 2015).

In the case of curium, a visual inspection of the XMCD spectra is sufficient to realize that the integrated intensity of the features at M_5 and M_4 , which are opposite in sign, are not equal. From the orbital sum rule, this means that the orbital moment is not zero. The value provided by the experiment at 70 K is $\mu_L = -\langle L_z \rangle = 0.10(1)\mu_B$, with a ratio $\mu_L/\mu_S = +0.06$ close to the calculated value of $+0.052$ for the f^7 configuration in intermediate coupling (van der Laan and Thole, 1996). The fact that μ_L and μ_S are parallel in Cm metal is the reason why the sign of the M_4 line suddenly changes in comparison to the earlier elements (Fig. 22).

Equation (30) shows that the spin component of the magnetic moment can be obtained only if the value of $\langle T_z \rangle$ is known. This quantity cannot easily be directly measured. However, it can be immediately obtained from an analysis of the XMCD spectra if an independent measurement of the total magnetic moment $\mu = \mu_S + \mu_L$ is available, for instance, from neutron diffraction experiments or, in the case of Np compounds, from ^{237}Np Mössbauer spectroscopy. Figure 23 shows the $3\langle T_z \rangle/\langle S_z \rangle$ ratio obtained for several compounds for

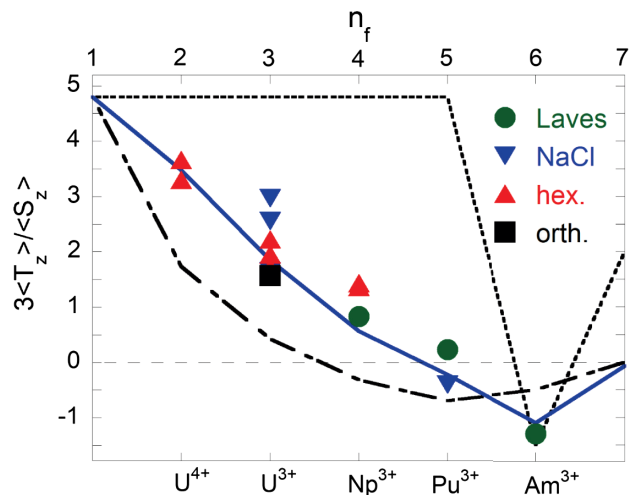


FIG. 23. The ratio $3\langle T_z \rangle/\langle S_z \rangle$ between the expectation values of the magnetic-dipole term and the spin moment along the quantization direction as a function of the $5f$ occupation number n_f . The symbols represent experimental data obtained from an analysis of XMCD spectra at the $M_{4,5}$ actinide edges for compounds with different physical properties and crystallographic structure (circles for C-15 cubic Laves phases, upside-down triangles for the NaCl-type structure, standard triangles for hexagonal lattice, and squares for orthorhombic cells). Theoretical estimates are shown for intermediate coupling (IC) (solid lines), Russell-Saunders (dashed line), and jj (dotted line) coupling approximations. All the calculated values refer to the free-ion ground state except for the f^6 configuration, where J mixing with the first excited state is taken into account; otherwise, the ratio cannot be determined, since all quantities would be zero for the ground state. Adapted from Magnani *et al.*, 2015.

which such information was available. By changing the $5f$ occupation number n_f , the ratio $3\langle T_z \rangle/\langle S_z \rangle$ varies, as predicted by atomic calculations in the intermediate coupling (IC) approximation. The correlation is convincing and suggests that $\langle T_z \rangle$ can be reliably estimated using IC calculations when the total magnetic moment μ is not known.

This is the case when the absorbing atom is located inside a vortex in a type-II superconducting compound. As an example, Fig. 24 shows XAS and XMCD spectra measured in

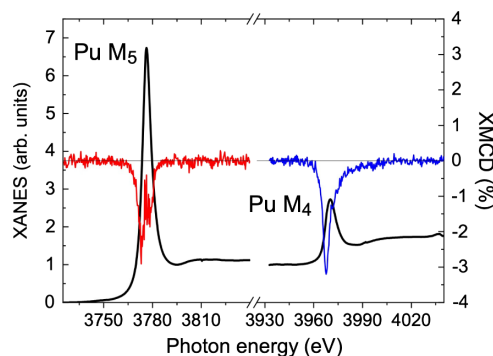


FIG. 24. XAS (solid black lines) and XMCD spectra as a function of photon energy through the Pu M_5 (red line) and M_4 (blue line) edges in $PuCoGa_5$. Adapted from Magnani *et al.*, 2017.

PuCoGa₅ (Magnani *et al.*, 2017), a tetragonal heavy-fermion superconductor with a critical temperature $T_c = 18.5$ K (Sarrao *et al.*, 2002). The origin of superconductivity in this compound remains puzzling, despite years of intensive investigations (Jutier *et al.*, 2008; Das, Zhu, and Graf, 2015; Ramshaw *et al.*, 2015). The Pu ground state is nonmagnetic (Hiess *et al.*, 2008), and the superconducting order parameter has d -wave symmetry (Daghero *et al.*, 2012).

XMCD spectra have been measured above and below T_c on a 2 mg single-crystal sample of ²⁴²PuCoGa₅ (99.99 wt % ²⁴²Pu) (Magnani *et al.*, 2017). The c axis of the crystal was oriented along the incident photon beam and is therefore parallel to the applied magnetic field. The critical field B_{c2} ($T = 0$) along the c axis is 63 T, so a vortex phase is present in an applied field smaller than 15 T. The $5f$ shell of the Pu atoms inside the vortex cores is polarized by the external field and the XMCD response is not zero. Applying the sum rules, the moments and their ratio can be extracted from the experimental data. The values obtained are in good agreement with dynamical mean-field theories (DMFT) predictions of a nonmagnetic ground state for Pu in PuCoGa₅; see Table I of Magnani *et al.* (2017). This unexpected result is the consequence of two effects: an intermediate valence driven by a $5f$ - $6d$ Coulomb interaction mixes a magnetic $5f^5$ sextet with a nonmagnetic $5f^6$ singlet, thereby reducing the magnetic moment; a complete quenching is then produced by a Kondo-like screening promoted by the hybridization between the $5f$ and conduction electron states (Pezzoli, Haule, and Kotliar, 2011; Shick *et al.*, 2013).

A good example of the utility of the XMCD technique in considering a complex material, about which little was known previously, is the study of Np₂T₁₇ ($T = \text{Co, Ni}$), where the unit cell contains two different Np sites and site-selective magnetic order can occur (Halevy *et al.*, 2012; Hen *et al.*, 2015). By combining XMCD with Mössbauer ²³⁷Np spectroscopy, magnetization measurements, and first-principles electronic structure calculations, deep insights on the ground state of these Np intermetallics were obtained. For the Ni analog, a nontrivial situation was observed below the ordering temperature T_N , where a large ordered moment ($2.25\mu_B$) appears in one Np site, while the other carries an induced moment of only about $0.2\mu_B$. Experiments were also performed on the Haucke intermetallic compound NpNi₅ (Hen *et al.*, 2014), showing a positive and large ratio between the expectation value of the magnetic-dipole operator and the spin magnetic moment, as predicted for localized $5f$ electrons, and an expectation value of the angular part of the spin-orbit interaction operator that is in good agreement with the value calculated in an intermediate coupling approximation for Np ions.

More recently a rather complete experiment including application of pressure up to 7 GPa was reported on the ferromagnet UGa₂ (Kolomiets *et al.*, 2021). This investigation also used absorption spectroscopy (HERFD XANES, as discussed in Sec. VII) as well as XMCD and includes considerable theory. This is an intermetallic system with a large ferromagnetic moment on the uranium of $3.0(2)\mu_B$, but Kolomiets *et al.* claimed through the spectroscopy that the $5f^3$ ground state is not localized, and that it should probably be

considered a band system. One of the long-standing challenges for theory on intermetallic actinide systems has been to get correct values for the orbital moments. Kolomiets *et al.* (2021) showed that when using the local-density approximation and dynamical mean-field theory (LDA + DMFT) they got a value for $\mu_L/\mu_S \approx -2.5$, which is close to the -2.6 value in Table II. There is also a cautionary tale from this study, as experimentally they found a moment of only $1.87\mu_B$, whereas both neutron and magnetization gave $3.0\mu_B$. Even though they had a single crystal, they ascribed this problem to surface contamination by UO₂. This again shows the surface sensitivity of this technique, even at the $M_{4,5}$ edges. Ironically, the experiments on transuranium samples (Wilhelm *et al.*, 2013; Janoschek *et al.*, 2015; Magnani *et al.*, 2015, 2017) have not suffered from this problem, as safety requirements demand airtight encapsulation.

Whereas the vast majority of XMCD experiments on actinide systems have used the $M_{4,5}$ edges, as we previously showed, a few studies (all at SPring-8) have been done at the $N_{4,5}$ edges (Okane *et al.*, 2006a, 2008), and a small number also at the $L_{2,3}$ edges (dos Reis *et al.*, 2017). The latter edges do not couple directly to the $5f$ electrons, as their electric-dipole contribution corresponds to $2p \rightarrow 6d$ transitions, whereas only the weaker electric-quadrupole term connects $2p \rightarrow 5f$ states. However, these transitions are known to be separated in energy by about 5 eV, so it is possible to measure both transitions. This was done at the Brazilian synchrotron (with additional measurements at the APS) by dos Reis *et al.* (2017) on the uranium intermetallic compounds UCu₂Si₂ and UMn₂Si₂; see Fig. 25. They showed a much larger quadrupolar peak in the case of UMn₂Si₂ and were able to model important differences between the $5f$ - $6d$ hybridization in the two different compounds. The experiments on these Mn compounds were taken at 300 K, but it is known from neutron work that the U moments order only at 100 K, whereas the Mn moments order at 377 K. On lowering the temperature below 100 K, a large increase was observed for the quadrupole transition, which was also observed at the uranium M_4 edge, proving that the assignment of the electric-quadrupole transition to the $5f$ states is correct. Although these interpretations do depend on modeling, it is perhaps surprising that more work at the L edges has not yet been reported.

As far as we know, there is no quantitative theory directly addressing the linewidths of the $M_{4,5}$ XMCD signals, but it is clear from an examination of Fig. 22 that the spectra are much sharper (there is a longer lifetime for the transitions) when the systems are localized. The spectra for localized AmFe₂ and Cm metal are both narrower than the other Laves-phase materials, which are bandlike. This is related to the transitions giving rise to the absorption edge into the unoccupied $5f$ states, so it is a measure of the $5f$ bandwidth above E_F , the Fermi level. In an itinerant system, the $5f$ hybridization with the conduction states will increase the bandwidth of the unoccupied states, so we expect a broader transition in energy. Lifetime effects will also broaden the transitions due to additional decay channels. The M_4 transition involves only the $3d_{3/2}$ core subshell, so there is only a single transition to the $5f_{5/2}$ subshell. The differences in some Pu materials are shown in Fig. 26. The M_4 lifetime is given as ~ 4 eV, so the

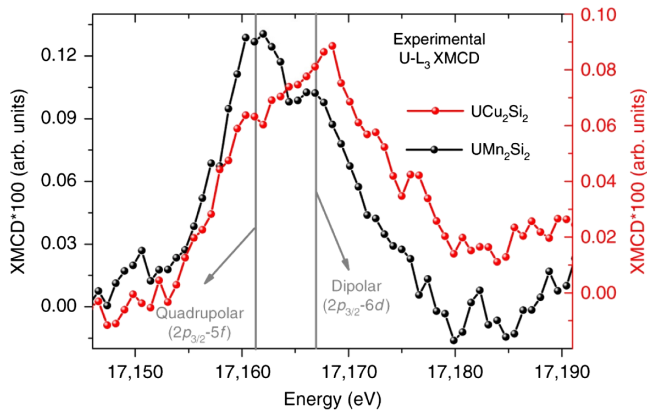


FIG. 25. XMCD measurements for UCu_2Si_2 and UMn_2Si_2 performed at temperatures of 10 and 300 K, respectively. The positions of the electric-dipole and quadrupolar transitions are marked. From *dos Reis et al., 2017*.

localized system PuSb (*Janoschek et al., 2015*) is close to this value. On the other hand, it is a surprise that the M_4 line shape for the heavy-fermion PuCoGa_5 superconductor (*Magnani et al., 2017*) is also so narrow. In contrast, the bandlike ferromagnet PuFe_2 (*Wilhelm et al., 2013*) has an energy full width at half maximum that is at least twice that of the intrinsic lifetime.

Such effects may also be observed at the M_5 edges, although there the situation is more complex, as both the $3d_{3/2} \rightarrow 5f_{5/2}$ and the $3d_{5/2} \rightarrow 5f_{7/2}$ transitions may be observed, and they differ in energy by a few eV. Therefore, for a localized system such as PuSb (*Janoschek et al., 2015*) two separate peaks may be observed, whereas the broadening of the spectra in PuFe_2 does not allow for the observation of two such peaks. The double-peak feature was first observed in

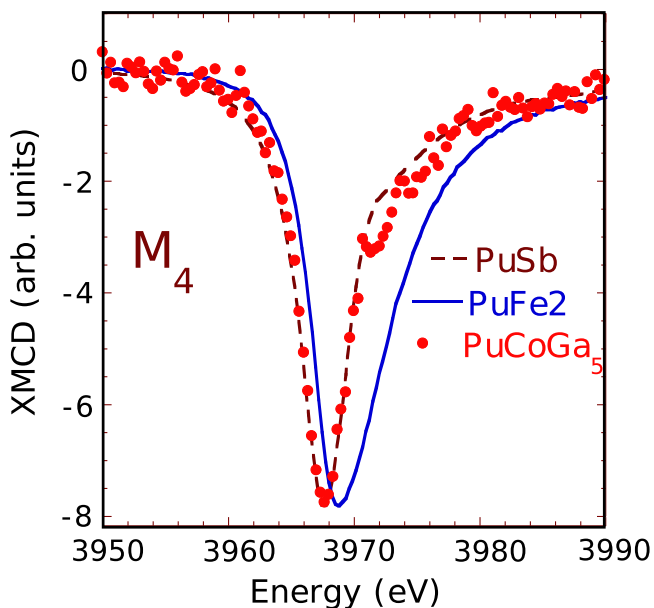


FIG. 26. XMCD signal at the M_4 edge from three different Pu materials: the localized system PuSb (*Janoschek et al., 2015*), the heavy-fermion superconductor PuCoGa_5 (*Magnani et al., 2017*), and the bandlike system PuFe_2 (*Wilhelm et al., 2013*).

resonance diffraction experiments on PuSb (*Normile et al., 2002a*) but was not understood at the time.

The case of AmFe_2 merits further discussion. For a localized Am^{3+} ion the ground state with six $5f$ electrons has the $j = 5/2$ subshell full, so the quantum ground state is $J_z = L_z + S_z = 0$. In AmFe_2 the Am ions are in a strong magnetic field induced by the surrounding magnetized Fe atoms, but $\langle J_z \rangle$ is still zero. The finite spin and orbital moments arise from mixing with the $J = 1$ excited state (*Magnani et al., 2015*). Since the orbital moment $\mu_L = -\langle L_z \rangle$, whereas the spin moment $\mu_S = -2\langle S_z \rangle$, and they are the opposite of each other, one can see that as the induced field is increased the μ_S moment begins to dominate the μ_L moment since the spin moment will be twice the orbital moment and of the opposite sign. We have the counterintuitive situation in which the spin moment is opposed to the molecular field induced by the Fe moments, which are easily aligned by an external field and increases with the applied field. This is a direct consequence of the quantum mechanics defining the $J_z = 0$ ground state. The actual value of the Am moment in AmFe_2 was found to be $-0.44(11)\mu_B$ (*Magnani et al., 2015*). This is in good agreement with the $\sim -0.4\mu_B$ result reported in an early experiment using polarized neutrons on polycrystalline samples, although the reason for the negative moment on the Am site was not understood at the time (*Lander et al., 1977*).

VII. RIXS AND RESONANT X-RAY EMISSION SPECTROSCOPY EXPERIMENTS

RIXS experiments consist in measuring the energy dependence of the emission line after creating a core hole by photons tuned around an atomic absorption edge (*Kotani and Shin, 2001; Ghiringhelli et al., 2004; Braicovich et al., 2010; Rueff and Shukla, 2010*). One of the main applications of RIXS is measuring the energy dependence of electronic and magnetic excitations and their tensorial character (*van Veenendaal, Carra, and Thole, 1996; Borgatti et al., 2004; Ament et al., 2011*), although this has not yet been applied to actinide materials.

In a RIXS experiment, the scattering cross section is measured by scanning the incident and emitted photon energy plane in a region around the selected absorption edge and emission transition. In the case of actinides, the combinations used in the majority of the experiments performed thus far are the $L_3 - L\alpha_1(L\beta_5)$ and the $M_{4,5} - M(\alpha, \beta)$ ones. The former, spanning the incident energy range ~ 17 – 19 keV and an energy transfer range ~ 3 – 4 keV, implies an absorption transition $26p^6d^n \rightarrow 2p^56d^{n+1}$ followed by the emission transition $3d^{10}(5d^{10})6d^{n+1} \rightarrow 2p^63d^9(5d^9)6d^{n+1}$. The latter, in the incident energy range ~ 3.5 – 4.3 keV and the energy transfer range ~ 0.3 – 0.4 keV, probes the $3d^{10}5f^n \rightarrow 3d^95f^{n+1}$ absorption followed by a $4f^{14}5f^{n+1} \rightarrow 3d^{10}4f^{13}5f^{n+1}$ emission.

As previously mentioned, incident energy scans at the maximum of the emission line are called HERFD-XANES spectra. On the other hand, measurements at a fixed incident energy and varying final energy are referred to as resonant x-ray emission spectroscopy (RXES) (*Rueff and Shukla, 2010; Vitova et al., 2010; Kvashnina, Kvashnin, and*

Butorin, 2014; Walshe *et al.*, 2014). Compared to conventional XANES, HERFD XANES offers the advantage of an increased resolution in the absorption process since the final transitions are from intermediate states with larger intrinsic core-hole interaction lifetimes. At the U L edge, for instance, the energy resolution is improved from ~ 8 to ~ 4 eV, while energy resolutions of 0.4–0.3 eV can be obtained at the U $M_{4,5}$ edges (Kvashnina, Kvashnin, and Butorin, 2014).

At the L_3 edge and the $L\alpha_1$ emission line, HERFD XANES and RXES (see Fig. 19 and the accompanying discussion) have been used to study the multiconfigurational nature of $5f$ orbitals in several thorium, uranium, and plutonium intermetallics and oxides (Rueff *et al.*, 2007; Böhler *et al.*, 2014; Booth *et al.*, 2014; Bao *et al.*, 2018; Honda *et al.*, 2020; Kawamura *et al.*, 2020), demonstrating that the edge position can be related to the density of states at the Fermi level, and that the contributions from different $5f$ electron configurations can be estimated from an analysis of the spectral features (Booth *et al.*, 2012, 2016; Tobin, Yu, Booth *et al.*, 2015).

As both incident and scattered photon energies are high in a RXES measurement at the L_3 edge of actinides, this technique has been applied to studying the evolution of $5f$ states upon compression. Being sensitive to final-state energy distributions in the presence of a core hole, RXES is a good probe of mixed valency (Rueff and Shukla, 2010). Experiments have been performed on localized systems (UPd₃) and heavy-fermion compounds (UPd₂Al₃), showing for the first a stable U⁴⁺ valence state and for the second a progressive transformation upon compression from a mixed valence U^{4- δ} state to a U^{4+ δ} configuration (Rueff *et al.*, 2007). This kind of measurement in diamond-anvil pressure cells requires a small amount of material, usually $\mathcal{O}(1 \mu\text{g})$. This is particularly welcome when working on transuranium materials because it eases the management of the safety risk. For instance, an experiment at the L_3 edge of elemental americium (18.518 keV) was performed using a wide-aperture, membrane-type diamond-anvil cell with an $\sim 5\text{-}\mu\text{m}$ -thick foil of ²⁴³Am metal (with a mass of ~ 600 ng) loaded into the hole (130 μm diameter) of an Inconel gasket (Heathman *et al.*, 2010). The energy dependence of the $L\alpha_1$ emission line (14.625 keV) was measured for pressure ranging from 4 GPa (double-hexagonal, closed-packed Am phase I) to 23 GPa, into the orthorhombic Am-IV phase; see Fig. 7. $5f$ electrons are supposed to be localized in Am I and itinerant in Am IV (Heathman *et al.*, 2000; Griveau *et al.*, 2005). Many-body electronic structure calculations based on the LDA + DMFT have suggested that the localization-delocalization edge is approached by a mixing of the nonmagnetic $5f^6$ Am ground state with the magnetic $5f^7$ configuration, combined with hybridization with the $6d$ valence band (Savrasov, Haule, and Kotliar, 2006). The experiment, however, does not support such a scenario, as no evidence of a mixed valence character emerges at high pressure (Heathman *et al.*, 2010). The experimental results seem rather in agreement with the predictions of a variant of the LDA + DMFT method that takes into account not only the correlations among the $5f$ electrons but also the feedback of these correlations on the rest of the system by means of an appropriate adjustment of the electronic charge density (Kolorenc, Shick, and Caciuffo, 2012).

RXES measurements at the $M_{4,5}$ edges have the advantage over measurements at the L edge of interrogating directly $5f$ states. The lower energies involved (a few keV), however, imply a reduced photon penetration depth (a few hundred nanometers; see Table I), and therefore attention must be paid to avoid any surface oxidation of the measured sample. Such experiments have been performed to study coordination complexes (Vitova *et al.*, 2010; Bès *et al.*, 2016), to study uranium intermetallic compounds (Gumenuik *et al.*, 2015, 2018; Kvashnina *et al.*, 2017), and to elucidate the gradual conversion of the U oxidation state in mixed uranium oxides (Kvashnina *et al.*, 2013).

Kvashnina *et al.* (2017) reported full core-to-core RXES maps for UPd₃, USb, USn₃, and URu₂Si₂. The experiment was performed at the ID26 beamline of ESRF (Glatzel *et al.*, 2021) by scanning the incident energy across the U $M_{4,5}$ edges at different emission energies around the $M\alpha$ and $M\beta$ emission lines. For UPd₃, a localized system with a $5f^2$ configuration, incident energy scans at the maximum of the emission lines showed a shift of the white line by ~ 0.2 eV compared to UO₂ (also a localized system with a $5f^2$ electron configuration but with an empty conduction band), and that the white line shift for $5f^2$ (UPd₃) and $5f^3$ (USn₃) in intermetallic compounds is smaller than it is in ionic compounds. For URu₂Si₂, where an itinerant character of the $5f$ electrons is expected, the spectral features observed at the M edges suggest almost tetravalent U atoms, with a $5f^2$ configuration. This is in contrast to the results of high-energy-resolution core-level and valence-band photoelectron spectroscopy studies (Fujimori *et al.*, 2012) and with the analysis of L_3 RXES data (Booth *et al.*, 2016) that give an n_f value close to 3 for the $5f$ occupation number, but in agreement with the conclusions of polarized-neutron scattering (Santini *et al.*, 2000; Ressouche *et al.*, 2012), NIXS experiments (Sundermann *et al.*, 2016), and high-resolution RIXS measurements at the U O edges (Wray *et al.*, 2015). The discrepancy with the L_3 RXES conclusions about n_f is probably due to $5f$ - $6d$ hybridization effects that are more relevant at the L_3 edge, where the $5f$ shell is interrogated only indirectly. The degree of $5f$ electron localization in URu₂Si₂ was examined by Jeffries *et al.* (2010) using a spin-orbit sum rule analysis of EELS spectra at the U $N_{4,5}$ edge.

As mentioned, experiments at the M edges require clean surfaces because of the small penetration depth of a few hundred nanometers; see Table I. This requirement is much more stringent at the $N_{4,5}$ edges ($4d \rightarrow 5f$), where the penetration depth is of a few nanometers only. The reward for the effort required is an energy resolution that can be as good as 30–35 meV in an energy range up to 1 eV.

Figure 27 shows the RIXS spectrum at the uranium N_4 absorption edge (778 eV) measured at 15 K on beamline I21 of the Diamond Light Source (Zhou *et al.*, 2022) on atomically flat, epitaxial UO₂ films (~ 100 nm thickness) (Lander *et al.*, 2021). With a resolution of 35 meV, the crystal-field excitations within the ³H₄ ground-state multiplet are resolved between ~ 140 and 180 meV, confirming earlier inelastic neutron scattering (INS) studies (Amoretti *et al.*, 1989). INS measurements on UO₂ failed to detect nondipolar, higher-energy intermultiplet excitations. RIXS instead shows excitations at 520–580 meV due to transitions toward

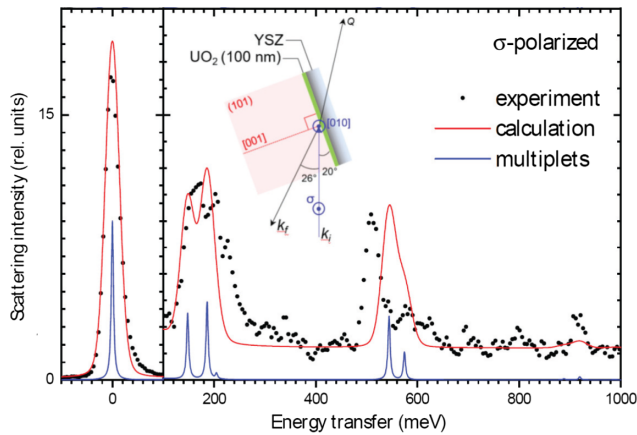


FIG. 27. $U N_4$ -edge RIXS spectra of UO_2 at $T = 15$ K. Data were taken with a photon energy of 778 eV for σ linear polarization, as shown in the inset. The red lines show the RIXS spectrum calculated for the $U^{4+} 5f^2$ configuration and crystal-field parameters consistent with inelastic neutron scattering. The blue lines show the underlying multiplet peaks (without line broadening) of the crystal-field excitations around 180 meV and those for the 3F_2 multiplet around 550 meV. Adapted from Lander *et al.*, 2021.

components of the 3F_2 excited multiplet. Measurements with π polarization at the N_5 edge (not shown in Fig. 27) also establish a peak at ~ 920 meV due to a transition to the 3H_5 multiplet. RIXS experiments around the O edges ($5d \rightarrow 5f$) have been attempted to determine the oxidation state of curium in oxide forms (Kvashnina *et al.*, 2007). At this edge, however, it is complicated to get access to bulk properties by RIXS measurements due to the small penetration length; see Table I.

These problems are also illustrated in the work on URu_2Si_2 using the O resonance by Wray *et al.* (2015). They suggested that the data are compatible only with uranium having a $5f^2$ -like ground state [in agreement with the NIXS work of Sundermann *et al.* (2016)], but they proposed that the wave functions have a dominant $J_z = |\pm 3\rangle$ component rather than the $J_z = |\pm 4\rangle$ value proposed in the NIXS work (Sundermann *et al.*, 2016). Because of the low penetration of the ~ 100 eV incident photon beams at this resonance energy, bulk properties may not be sampled and, in addition, the modeling is complicated due to extreme shallowness of the created core-hole interaction.

RIXS experiments have a bright future, especially at the M and N edges. New work at the M edges (at the DESY synchrotron in Hamburg, Germany) has shown signs of multiplets in a number of uranium systems with the present resolution of ~ 150 meV, while new experiments at the Diamond Light Source with a resolution of ~ 100 meV at the uranium N edges have seen a signal in the $5f^1$ U system U_3O_8 , and almost no measurable signal in UN, so this field is currently active (Lawrence Bright *et al.*, 2023). It is limited by the number of instruments available and their intensity and resolution.

VIII. NIXS EXPERIMENTS

NIXS at the $O_{4,5}$ ($5d_{3/2,5/2} \rightarrow 5f$) absorption edges is a bulk-sensitive technique exploiting multipole transitions from

core $5d$ to valence $5f$ states. For small values of the scattering vector \mathbf{Q} , the NIXS spectra are dominated by the dipole-allowed transitions encapsulated within the giant Fano resonance. For high \mathbf{Q} values, the intensity of the dipole transitions becomes negligible and the spectral response is dominated by dipole-forbidden transitions appearing as a well-resolved multiplet structure in the preedge region (Macrander *et al.*, 1996; Gurtubay *et al.*, 2005; Haverkort *et al.*, 2007; Larson *et al.*, 2007; van Veenendaal and Haverkort, 2008; van der Laan, 2012a). These features provide information on states with symmetries other than those interrogated by electric-dipole transitions in XAS and are sensitive to atomic-environment, valence, and hybridization effects (Gordon *et al.*, 2008).

Compared to most other x-ray spectroscopy techniques, NIXS is intrinsically intensity limited. On the other hand, the absence of an intermediate state makes it easy to model the experimental data in a quantitative way. Another advantage of NIXS is that shallow energy edges are probed by hard x rays. Bulk-sensitive information is therefore obtained. Moreover, the high penetration depth of hard x rays ($\sim 5 \mu\text{m}$ in UO_2 for 10 keV incident photons) makes the study of encapsulated samples feasible, which is a prerequisite in the case of transuranium materials.

Far from resonance conditions, the radiation-matter interaction is dominated by a term proportional to the square of the vector potential \mathbf{A} . Within the first Born approximation, the NIXS double differential cross section is obtained by expanding the transition operator $\exp(i\mathbf{Q} \cdot \mathbf{r})$ in terms of spherical harmonics and is given by Eq. (40).

The potential of NIXS for characterizing the dynamical electron-density response in actinide materials has been demonstrated in a few studies of oxides and intermetallic compounds at the $O_{4,5}$ absorption edges (Bradley *et al.*, 2010; Caciuffo, van der Laan *et al.*, 2010; Sen Gupta *et al.*, 2011; Sundermann *et al.*, 2016, 2018, 2020). Attempts to carry out NIXS experiments at the N edges of actinides have been frustrated by the weakness of the signal.

Figure 28 shows, as an example, the NIXS room-temperature spectra obtained for UO_2 in an energy loss ($\hbar\omega = E_g - E_f$) range encompassing the uranium $O_{4,5}$ absorption edges (Caciuffo, van der Laan *et al.*, 2010). Data were collected at the ID16 inverse-geometry, multiple-analyzer-crystal spectrometer (Verbeni *et al.*, 2009) of ESRF, with a resolution of ~ 1.3 eV at a final photon energy E_f of 9.689 keV. The sample was a UO_2 single crystal with an exposed external surface perpendicular to $[111]$.

At $Q = 2.81 \text{ \AA}^{-1}$, the response is dominated by the dipole transition and shows a broad, asymmetric Fano profile due to resonant decay into continuum states, as observed with XAS measurements (Kalkowski, Kaindl, Brewer, and Krone, 1987). Above $Q \sim 9 \text{ \AA}^{-1}$, the higher multipole transitions appear at lower energies, with three resolved features at 94.9, 97.3, and 103.6 eV at $Q = 9.88 \text{ \AA}^{-1}$, providing a fingerprint for the uranium ground state [the radial and angular dependence of the NIXS cross section for the $O_{4,5}$ edge of a $U^{4+} 5f^2$ configuration was discussed by Caciuffo, van der Laan *et al.* (2010) and Sundermann *et al.* (2016)].

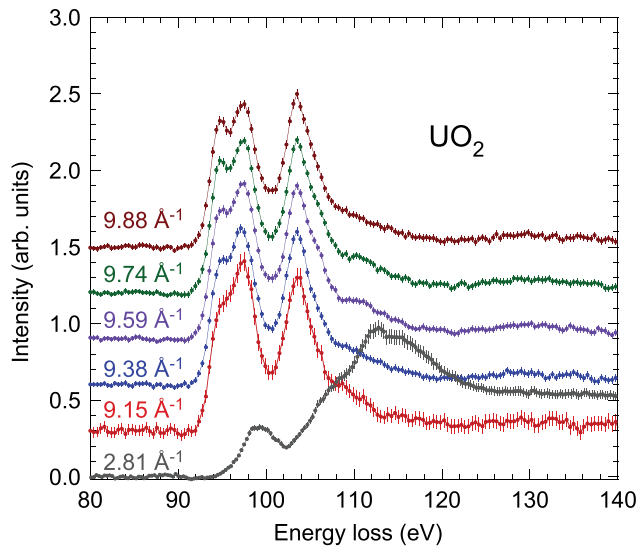


FIG. 28. NIXS spectra for UO_2 at the uranium $O_{4,5}$ edges measured with a fixed final energy of 9.689 keV at different values of the scattering vector Q . Data at different Q values are normalized to the peak intensity of the feature centered at about 104 eV. Adapted from Caciuffo, van der Laan *et al.*, 2010.

Good agreement was found between the experimental data shown in Fig. 28 and many-electron atomic spectral calculations in intermediate coupling that allows one to identify the origin of the observed multipole transitions (Caciuffo, van der Laan *et al.*, 2010; van der Laan, 2012a). Similar experiments were also extended to transuranium materials in investigations of $5f^3$, $5f^4$, and $5f^5$ configurations in NpO_2 , PuO_2 , and $\beta\text{-Pu}_2\text{O}_3$, respectively (Sundermann *et al.*, 2020).

The sum rule for the branching ratio of the electric-multipole transitions from a core hole to a spin-orbit split valence state probed by NIXS was derived by van der Laan (2012b) and is given in Eq. (47). It shows that the effect of the valence spin-orbit interaction on the branching ratio strongly depends on k , the rank of the transition. These effects are large at the end of the lanthanide series, as in the case of the $\text{Er } 4f^{11} M_{4,5}$ spectra but are also observable for light actinides, as for the $\text{U } 5f^2 O_{4,5}$ transition, thus providing additional information about the electronic structure of the investigated material (van der Laan, 2012a, 2012b).

In contrast to the dipole transition, which in cubic systems cannot exhibit any directional anisotropy, the multipole transitions in the NIXS process branch to representations with distinct angular dependence. This fact introduces an anisotropy of the NIXS signal, with measurable differences of the spectral intensity along different directions of the momentum transfer. This directional dichroism can be exploited to gain information about the symmetry and strength of the crystal field acting on the scattering atoms (Willers *et al.*, 2012). The potential of the method has been demonstrated for tetragonal, intermetallic URu_2Si_2 (Sundermann *et al.*, 2016) and cubic UO_2 (Sundermann *et al.*, 2018), in which the crystal field is firmly established by inelastic neutron scattering experiments (Amoretti *et al.*, 1989; Magnani *et al.*, 2005). Figure 29 shows the comparison between experimental data and simulations in the case of UO_2 .

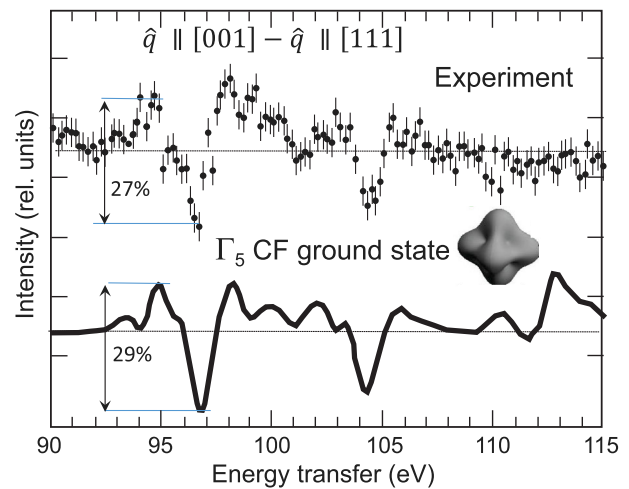


FIG. 29. Difference between the experimental NIXS spectra measured at the uranium $O_{4,5}$ edges in single-crystal UO_2 with a momentum transfer direction $\mathbf{Q} = \mathbf{Q}/Q$ along $[001]$ and $[111]$. Calculations assuming a Γ_5 triplet crystal-field ground state and a crystal-field potential strength compatible with inelastic neutron scattering experiments are indicated by the solid line. Adapted from Sundermann *et al.*, 2018.

The ability to detect these anisotropies in NIXS experiments depending on the direction of the scattering vector has been important in studies of the URu_2Si_2 series of compounds, which includes the heavy-fermion superconductor URu_2Si_2 , for which neither the electron count (i.e., either f^2 or f^3) nor the associated ground-state crystal-field wave functions have been firmly established prior to this NIXS investigation (Sundermann *et al.*, 2016).

The crystal field in the case of the lower (tetragonal) symmetry of URu_2Si_2 (Sundermann *et al.*, 2016), where the $J = 4$ multiplet splits into five singlets and two doublets, is more complicated than it is for UO_2 (Sundermann *et al.*, 2018). The full wave functions were given by Sundermann *et al.* (2016). An examination of the calculated anisotropies in Fig. 30(a) shows that only the Γ_1 and Γ_2 states agree with the experimental data in Fig. 30(b). These differences in the directional signal are shown explicitly in Fig. 30(c), where a more quantitative evaluation of the ground-state wave function is given. The wave function must contain a large proportion of the $J_z = |\pm 4\rangle$ state. The ground states of a $5f^3$ configuration cannot explain the experimental results. This was the first time that the ground-state wave function was identified in URu_2Si_2 , so it is an important achievement. Many theories have been proposed to explain the properties of this material [see Mydosh and Oppeneer (2011) and Mydosh, Oppeneer, and Riseborough (2020) for reviews], and there has been confusion as to whether to start any theory from a $5f^2$ or $5f^3$ configuration. Experiments with neutron inelastic scattering have not been able to observe any well-defined crystal-field levels, because of the mixing of the $5f$ states with the conduction states (Mydosh and Oppeneer, 2011; Mydosh, Oppeneer, and Riseborough, 2020). A polarized-neutron study (Ressouche *et al.*, 2012) of the magnetization induced with a magnetic field found the results consistent only with a $5f^2$ configuration, also with the Γ_1 or Γ_2 states the likely

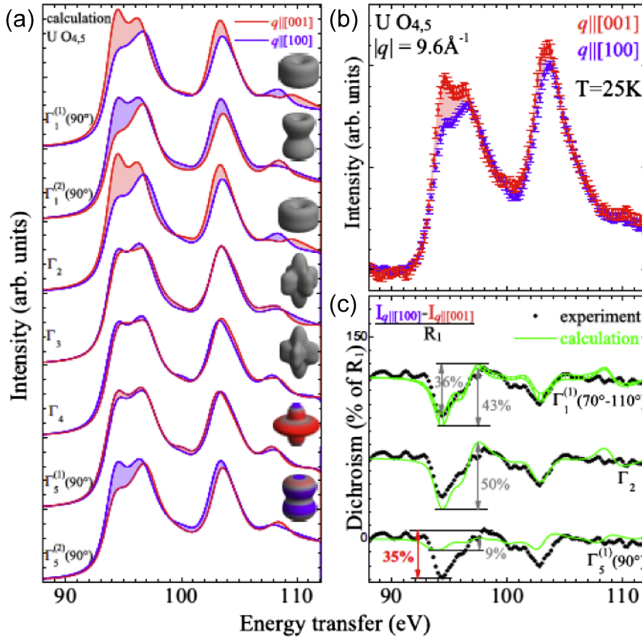


FIG. 30. NIXS measurements of the U $O_{4.5}$ edge of URu_2Si_2 for $Q = 9.6 \text{ \AA}^{-1}$ and corresponding calculations for $5d^{10}5f^2 \rightarrow 5d^95f^3$. (a) Simulation of $S(\mathbf{Q}, \omega)$ of U crystal-field states for $J = 4$ in D_{4h} symmetry for the two directions $\mathbf{Q} \parallel [001]$ (red) and $\mathbf{Q} \parallel [100]$ (blue). Insets: the corresponding electron densities. (b) NIXS data for momentum transfers $\mathbf{Q} \parallel [100]$ (blue) and $\mathbf{Q} \parallel [001]$ (red) at $T = 25 \text{ K}$. (c) Dichroism in a percentage defined as the difference $I(\mathbf{Q} \parallel [100]) - I(\mathbf{Q} \parallel [001])$ relative to the peak height R_1 as defined in the isotropic spectrum. The data (black dots) and calculations (green lines) for the crystal-field states are provided with the correct sign of the directional dichroism. Here the data points have been convoluted with a Gaussian of 0.5 eV FWHM. From [Sundermann *et al.*, 2016](#).

ground states. The NIXS experiment ([Sundermann *et al.*, 2016](#)) found no temperature dependence of the signal, so these results are not able to make any statements about the apparent hidden order that appears at 17 K . This is a rare example of an intermetallic material exhibiting atomlike multiplets, although the $5f$ states are mostly itinerant.

A second important NIXS paper was published by [Amorese *et al.* \(2020\)](#), who reported on an investigation of a series of single crystals of UM_2Si_2 compounds, with $M = \text{Fe, Ni, Ru, and Pd}$. For the NIXS experiments [Amorese *et al.*](#) found that the four compounds had similar anisotropies, as mentioned for URu_2Si_2 ([Sundermann *et al.*, 2016](#)), showing that as a basis for discussing these materials one needs to start with a $5f^2$ multiplet structure. In addition to NIXS, they also examined the $4f$ core states of these same materials using a high-energy (5.945 keV) photon beam with an overall instrumental resolution of 0.3 eV . These core levels are between 370 and 400 eV , and their position and width depend on the valence state. UPd_3 was used for the nominally localized $5f^2$ state, and UCd_{11} was used for the $5f^3$ state. They argued that the transition-metal d states play an important role, as they mix with the U $5f_{5/2}$ band strongly in the Fe compound, and such mixing becomes smaller for Ru and Ni and is almost negligible for Pd. Finally, [Amorese *et al.* \(2020\)](#) showed how

the properties can be placed on a Doniach-like phase diagram. Both experiments were performed at the PETRA beamlines in Hamburg, showing that this third-generation machine is now also performing experiments on actinides, at least with uranium.

IX. HIGH-RESOLUTION IXS EXPERIMENTS

High-resolution IXS at third-generation SR sources is a well-established technique for mapping phonon branches with meV energy resolution. High-performance spectrometers using crystals in near-backscattering geometry and efficient focusing optics ([Burkel, 2000](#)) allow one to measure phonon dispersion curves in crystals with volumes as small as 10^{-4} mm^3 , and in epitaxial thin films less than 500 nm thick ([d'Astuto *et al.*, 2002](#); [Rennie, Lawrence Bright, Darnbrough *et al.*, 2018](#)). Compared with neutrons, this is a crucial advantage for studying radioactive materials or, in general, systems for which large single crystals are not available or high pressure limits the crystal size. The intrinsic background in IXS experiments is low, the energy resolution is decoupled from energy transfer, and the momentum transfer is energy independent. A drawback of the technique is that the scattering cross section is proportional to the square of the atomic number, making it challenging to observe the contributions of light atoms to the vibrational spectra.

The ID28 beamline at the ESRF is an example of a high-performance IXS spectrometer. In the incident energy range of interest for actinide systems ($\sim 17\text{--}24 \text{ keV}$), a flat Si perfect crystal monochromator in backscattering geometry, temperature controlled in the millikelvin region, affords an energy resolution of about $1.5\text{--}3 \text{ meV}$ when the analyzer is thermally stabilized to $6 \times 10^{-4} \text{ K}$. Properly oriented single-crystal diamond slabs provide ideal windows if sample encapsulation is mandated for safety reasons.

The IXS cross section for single-phonon scattering is proportional to the scattering function $S(\mathbf{Q}, \omega)$ ([Krisch and Sette, 2007](#)):

$$S(\mathbf{Q}, \omega) = \sum_{d, \mathbf{q}, j} \left| \frac{f_d(Q) e^{i\mathbf{Q} \cdot \mathbf{r}_d} e^{-W_d} (\boldsymbol{\epsilon}_d^{\mathbf{q}, j} \cdot \mathbf{Q})}{\sqrt{M_d}} \right|^2 \times \frac{\delta(\hbar\omega \pm E_j(\mathbf{q}))}{E_j(\mathbf{q})} \left\langle n(E_j, T) + \frac{1}{2} \pm \frac{1}{2} \right\rangle, \quad (72)$$

where $\mathbf{Q} = \mathbf{G} + \mathbf{q}$, with reciprocal lattice vector \mathbf{G} and phonon quasimomentum \mathbf{q} . f_d is the atomic form factor of the d th atom located at position \mathbf{r}_d of the unit cell, with the Debye-Waller factor W_d . Phonons with a polarization vector $\boldsymbol{\epsilon}_d^{\mathbf{q}, j}$ and polarization index j (taking values 1 to $3n$, where n is the number of atoms per unit cell) have an energy $E_j(\mathbf{q})$. The plus (minus) sign in the Bose factor $\langle n(E_j, T) + 1/2 \pm 1/2 \rangle$ at temperature T indicates phonon creation (annihilation). The sum in Eq. (72) is over the n values of d , the N values of \mathbf{q} in the first Brillouin zone (given by the number of unit cells in the crystal), and the $3n$ values of j . Note that here the scattering factor is necessary, as all the electrons contribute and have their spatial distribution. This is not the case in resonant scattering experiments.

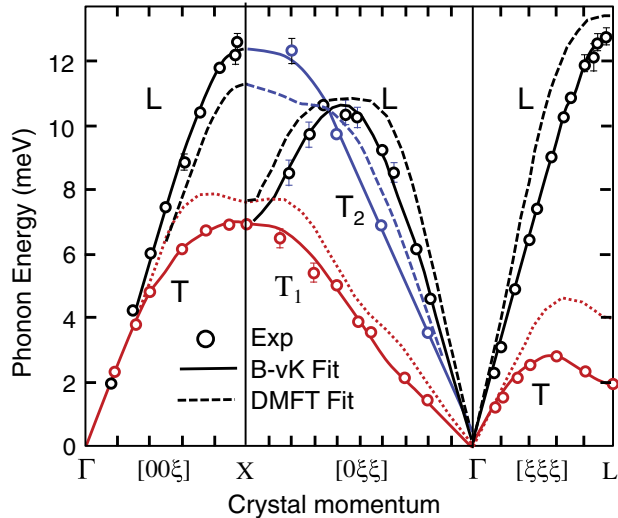


FIG. 31. Phonon dispersion curves at $T = 300$ K along high-symmetry directions in δ -Pu stabilized by 0.6 wt % Ga alloying ($a = 0.4621$ nm). The experimental data are shown as circles [black longitudinal (L) modes, red and blue transverse (T) modes]. The branches T_1 and T_2 propagating along the $[0\xi\xi]$ direction are polarized along $\langle 011 \rangle$ and $\langle 100 \rangle$, respectively. The solid curves are the fourth-nearest-neighbor Born–von Kármán (BvK) model fit. The dashed curves are calculated dispersions for pure δ -Pu based on dynamical mean-field theory (DMFT) (Dai *et al.*, 2003). Adapted from Wong *et al.*, 2003.

Measurements of the dispersion curves in fcc δ -plutonium performed on large-grain polycrystalline samples are exemplary for illustrating the potential of IXS in the study of actinide materials (Wong *et al.*, 2003). The results are shown in Fig. 31 and provide a qualitative validation of the predictions of DMFT calculations (Dai *et al.*, 2003), showing that this theoretical approach is appropriate to describe not only the structure but also (at least qualitatively) the dynamics of strongly correlated electron systems. In particular, the experiment confirms the softening of the $T[111]$ modes and the low-shear elastic modulus C' , reflecting the strong coupling between the lattice structure and the $5f$ valence instabilities. This work, which was carried out at room temperature on the ESRF ID28 beamline, was described in a longer article (Wong *et al.*, 2005). In another attempt to determine whether the soft mode in the $[111]$ direction is further softened with a reduced temperature, the experimental team resorted to measuring at the APS the diffuse scattering (Wong *et al.*, 2004), which contains information on the phonons, with the eventual conclusion that there were no effects as a function of lowering the temperature (Xu *et al.*, 2008). There is still an open question regarding what happens above room temperature, but that raises further safety concerns.

The low-temperature properties of uranium metal have been a mystery since elastic constant measurements in the 1960s found a most unusual behavior. The phonons were measured (Crummett *et al.*, 1979) with neutron inelastic scattering in 1979, showing unusual softening along the $[100]$ direction of the orthorhombic structure of α -uranium. Following these

measurements, a charge-density wave (CDW) was found to develop at 43 K (Lander, Fisher, and Bader, 1994). α -U is the only element to exhibit such a CDW at ambient pressure. However, it was not until 2008 that a theory was presented for phonons (Bouchet, 2008), and it immediately suggested that the phonon anomaly should be suppressed by pressure: a prediction confirmed by experiments with ID28 at the ESRF using pressures up to 20 GPa (Raymond *et al.*, 2011). Later experiments with thin films were successful in placing the $[100]$ axis of α -U under tensile stress (Springell *et al.*, 2014) caused by interaction with the substrate, and the results were a CDW developing at 120 K, a much higher temperature than in the bulk. The combination of theory and experiment showed the importance of the electron-phonon couplings in the metal, and their momentum dependence. Properties such as the equation of state are affected by these considerations (Dewaele *et al.*, 2013).

The phonons in α -U were also measured at the APS in 2003, when the instrument to measure dispersion relations in single crystals there was new (Manley *et al.*, 2003). These measurements, combined with others using neutrons, led to the discovery of a new effect in α -U at room temperature that actually disappears above 650 K, which was described as an intrinsic localized mode (Manley *et al.*, 2006, 2008). These results fit well into the earlier reports of a large phonon softening in the phonon density of states of α -U, as measured with neutrons (Manley *et al.*, 2001), over the same temperature range. However, the overall significance of these observations within the phase diagram for uranium is less clear and needs further elucidation.

Recently the IXS spectrometer has been pushed to new limits by measuring both diffuse scattering and the phonon dispersion curves from a thin (300 nm) epitaxial film of U-Mo alloys. These materials have been of interest for many years and might find applications as advanced nuclear fuels, but single crystals are not available and there has been controversy over whether the structures are bcc or something more complicated. Growing epitaxial films has turned out to be relatively simple, and the subsequent diffuse scattering patterns (Chaney *et al.*, 2021) showed that the structure is essentially bcc, but superposed on that symmetry is correlated disorder, where the local symmetry is lower, as if the uranium atoms prefer to have neighbors reminiscent of the low symmetry found in the element at room temperature, not the high symmetry demanded of bcc. The correlation length of this disorder depends on the composition but is of the order of 5–10 nm.

The phonon dispersion curves shown in Fig. 32 are close to those calculated using theory for this composition, except that they show large linewidths. The latter are much broader than expected for an alloy and are due to the correlated disorder in the material. Thus, we see new effects in these materials, which have been studied for many years. An earlier study of the phonons at the APS of a UMo alloy used small single crystals of dimensions $< 200 \mu\text{m}$ cut out by laser techniques from the melt (Brubaker *et al.*, 2019). Wide phonons were also found. However, the study assumed that because no extra phases were found with a standard Rietveld analysis, there is no diffuse scattering in this system. However, the diffuse scattering, which was first observed by Yakel (1969), does not

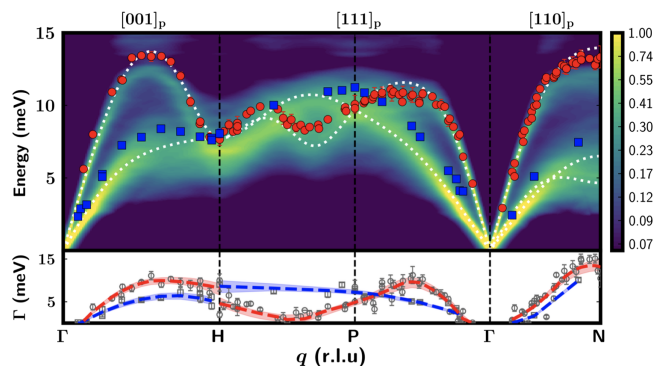


FIG. 32. Phonon energy (top panel) and linewidth (bottom panel) dispersions on epitaxial $U_{1-x}Mo_x$ thin film alloys. Transverse (longitudinal) acoustic modes are shown as blue squares (red circles) for the alloy with 23 at. % Mo. Theoretical results from a virtual crystal approximation for an alloy with 25 at. % Mo are shown as dashed white lines. The full spectral function is plotted as a $\log_{0.6}$ color map to rescale the intensity divergence at gamma. All directions are within the parent Brillouin zone. Bottom panel: raw linewidths Γ_0 displayed as gray squares (TA) and circles (LA). Deconvoluted linewidths Γ_d are shown by dashed blue (TA) and red (LA) trend lines. Adapted from Chaney *et al.*, 2021.

amount to even 1% of the strong bcc peaks, but its presence is crucial to understanding the formation and properties of the alloys. Given the intensity available at such synchrotron beams, it may be wise to search routinely in alloy systems for possible diffuse scattering.

Recent experiments (Paolasini *et al.*, 2021) at ID28 on the phonon linewidths of UO_2 below room temperature (this time using a single crystal rather than a thin epitaxial film) showed that the linewidth broadening in UO_2 is only along the [100] direction, not in the other directions.

These experiments were performed with IXS since with neutrons the magnetic cross section is appreciable and one wants a technique that is sensitive to only the vibrational spectra. The resolution was increased to 1.4 meV. In an exactly similar vein, the acoustic phonons of URu_2Si_2 were examined at the APS and anomalous widths were found for some of the vibrational modes (Gardner *et al.*, 2016).

IXS was used to measure the phonon dispersion in NpO_2 (Maldonado *et al.*, 2016), for which available single crystals are far too small for inelastic neutron scattering. The results observed along the three high-symmetry directions have been used to validate first-principles density-functional-theory calculations, with third-order anharmonicity effects in the quasi-harmonic approximation taken into account.

The phonons in the heavy-fermion superconductor $PuCoGa_5$ were also reported on by Raymond *et al.* (2006). The experiment was performed at room temperature and the theory required a Hubbard $U = 3$ eV to fit the phonons, suggesting rather localized $5f$ states, which was also the conclusion drawn from the XMCD experiments reported in Fig. 24.

In the case of polycrystalline or powder samples, if multi-phonon effects are negligible, it is possible to acquire the phonon density of states by summing $S(\mathbf{Q}, \omega)$ in all directions

for each value of momentum transfer \mathbf{Q} . In practice, this is obtained by summing IXS datasets measured at many different values of \mathbf{Q} (Bosak and Krisch, 2005). This technique was used to determine the phonon density of states (PDOS) for both α -Pu and δ -Pu using the instruments at the APS with an incident energy of 23.8 keV (Manley *et al.*, 2009). In an elemental system the PDOS may be related directly to the heat capacity, and this relationship seems to work well for the α -Pu phase. However, this is not the case for δ -Pu. It appears that most of the entropy stabilizing δ -Pu at high temperature comes from unconventional sources, including electron correlations and possibly intrinsic phonon softening, although the latter has not been found up to room temperature.

On polycrystalline compounds, IXS has also been applied to study the PDOSs of Ga-doped PuO_2 (Manley *et al.*, 2012) and fluorine-doped and undoped $NpFeAsO$, an analog of iron arsenide high-temperature superconductors (Walters *et al.*, 2015). In the case of the PuO_2 work the PDOS was deduced from various theories and compared with experiment. Perhaps unexpectedly, the theoretical results differed by a considerable amount. The best fit was found for DFT + U and for DMFT. For more on the theory for thermal conductivity in actinide oxides, see Hurley *et al.* (2022).

X. PES AND ARPES EXPERIMENTS

Photoemission techniques, which involve an incident photon and an emitted electron, are fundamentally different from all the experiments discussed in this review. Photoemission spectroscopy originates in the photoelectric effect, which was first explained by Einstein in 1905 (and for which he won the Nobel Prize in 1921) and was further exploited in the 1960s by Siegbahn and collaborators in Sweden (leading to the Nobel Prize in 1981). Reinart and Hüfner (2005) explained that the majority of photoemission experiments are performed with specialized laboratory equipment, but since the incident beam consists of photons there are advantages to using synchrotron beams. Two of these advantages are (a) investigations that can profit from tuning the incident photons to a known resonance of one of the elements in the sample and (b) investigations that are intensity limited, such as those that measure the signal as a function of the specific directions in a solid by, for instance, performing ARPES, which requires an intense beam to map much data. As we later show, both of these techniques have been used for actinide samples at synchrotrons.

Early PES work on actinides was reported on by Veal and Lam (1974) on Th, U, and their oxides, and by Naegele *et al.* (1984) on Am. This technique has made a considerable contribution to the research on actinides, and we note a large number of studies performed on transuranium samples at both Los Alamos National Laboratory and on those of the European Commission's Joint Research Centre. Examples are studies of Pu metal at both places (Arko *et al.*, 2000; Gouder *et al.*, 2001; Havela *et al.*, 2002), of the superconductor $PuCoGa_5$ (Joyce *et al.*, 2003; Eloiirdi *et al.*, 2009), of PuSb and PuTe (Gouder *et al.*, 2000), of PuN (Havela *et al.*, 2003), of Am metal and compounds (Gouder *et al.*, 2005), and elemental Cm (Gouder *et al.*, 2011). These are only some of the experimental results reported, and none have used synchrotron radiation.

On the other hand, early synchrotron work (Tobin *et al.*, 2003) focused on using the technique of resonant photoemission, with the incident energy tuned to the $O_{4,5}$ edges of ~ 110 eV, and involved both absorption and photoemission experiments. The differences reported between α -Pu and δ -Pu metal are actually quite small, and there is always at such low incident photon energies a question as to whether the true bulk properties are being examined. Both phases show that the states at the Fermi energy are dominated by the $5f$ electrons (Gouder *et al.*, 2001; van der Laan and Taguchi, 2010).

A. Core-level photoemission

The average number of $5f$ electrons making up the valence state in plutonium metal together with the electronic fluctuations on each metal site has been a subject of debate (Joyce and Lander, 2019). For the δ phase of Pu, where, compared to the α phase, increased localization (a more atomiclike character) leads to decreased overlap and volume increase, an f count close to either 5 or 6 has been proposed, depending on the type of electronic structure calculation. To resolve the controversy, the Pu $4f$ photoemission spectrum has been analyzed, which displays well-screened and poorly screened peaks that can be used as a measure for the degree of localization. Detailed Anderson impurity model calculations, including the full multiplet structure for Pu $4f$ photoemission, have been compared to experimental results obtained from one- to nine-monolayer thin films of Pu on Mg (Fig. 33) and from Pu metal in the α and δ phases (van der Laan and Taguchi, 2010). The trend in the satellite-to-main-peak intensity ratio as a function of the Pu layer thickness indicates that Pu metal has a mainly $5f^5$ -like ground state. For the Pu allotropes and thicker films an f count of 5.22 is obtained with a Coulomb interaction $U = 4$ eV. The calculated results for the f counts are given in Table III. As seen, the standard deviation σ corresponding to the spread over the f counts strongly increases with layer thickness, which indicates an increased delocalization due to stronger $5f$ fluctuations. A strong increase in delocalization is also found when going from δ to α Pu, whereas the average f count $\langle n \rangle$ is barely changing.

Further insight into the screening process of the photoexcited core electron can be gained from a simple two-level model (van der Laan *et al.*, 1981; van der Laan and Taguchi, 2010). Consider an initial state ψ_g composed of two basis states ψ_a and ψ_b (for instance, f^5 and f^6) with energy difference $\Delta = E_b - E_a$ and mixed by hybridization with a matrix element $V = \langle \psi_a | H | \psi_b \rangle$. Introducing the mixing parameter θ defined by $\tan 2\theta = 2V/\Delta$, the ground state can be written as

$$\psi_g = \psi_a \sin \theta - \psi_b \cos \theta. \quad (73)$$

After electron emission, the final-state basis functions are $\psi'_a = e^\dagger c \psi_a$ and $\psi'_b = e^\dagger c \psi_b$, where c is the annihilation operator of a core electron and e^\dagger is the creation operator of a continuum electron. The states have an energy difference $\Delta' = E'_b - E'_a$ and mixing $V' = \langle \psi'_a | H | \psi'_b \rangle$, with a mixing parameter θ' defined by $\tan 2\theta' = 2V'/\Delta'$. This gives the “bonding” and “antibonding” final states

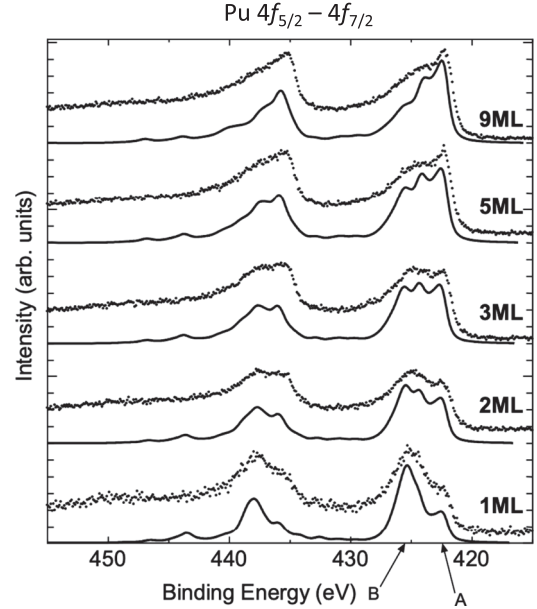


FIG. 33. $4f$ PES spectra for one-, two-, three-, five-, and nine-monolayer (ML) Pu thin films. The experimental results (dots) show a gradual increase in the main-to-satellite intensity ratio with increasing layer thickness [experimental data from Gouder *et al.* (2001)]. The arrows A and B indicate the energy positions of the main and satellite peaks, respectively, which are only well separated in the case of the most localized case of one ML. The experimental spectra are compared to Anderson impurity calculations (drawn lines) with the hybridization parameter $V = 0.25, 0.35, 0.4, 0.45,$ and 0.55 eV for an increasing number of MLs (van der Laan and Taguchi, 2010). The spectrum for nine-ML Pu resembles that of δ -Pu metal, whereas one-ML Pu resembles Am. From van der Laan and Taguchi, 2010.

$$\begin{aligned} \psi_M &= \psi'_a \sin \theta' - \psi'_b \cos \theta', \\ \psi_S &= \psi'_a \cos \theta' + \psi'_b \sin \theta', \end{aligned} \quad (74)$$

with an energy separation of

$$E_S - E_M = \sqrt{\Delta'^2 + 4V'^2}. \quad (75)$$

Substituting Eq. (74) into the transition probability $I_n = |\langle f_n | e^\dagger c | g \rangle|^2$, which is valid in the sudden approximation, gives the relative intensity ratio of the satellite to main peak as

TABLE III. Ground-state $5f$ weights in % for Pu thin films and α and δ Pu obtained from calculated PES spectra in Fig. 33 with a hybridization parameter V . Derived from this are the average value $\langle n \rangle$ and the standard deviation σ over the f count (van der Laan and Taguchi, 2010).

	V (eV)	$5f^4$	$5f^5$	$5f^6$	$\langle n \rangle$	σ
1 ML	0.25	1.3	81.4	17.3	5.16	0.16
2 ML	0.35	2.6	74.7	22.7	5.20	0.21
3 ML	0.40	3.4	72.1	24.5	5.21	0.23
5 ML	0.45	4.2	69.9	25.9	5.22	0.25
9 ML	0.55	5.7	66.4	27.8	5.22	0.29
α Pu	0.55	5.7	66.4	27.8	5.22	0.29
δ Pu	1.10	9.6	58.8	31.6	5.22	0.36

$$\frac{I_S}{I_M} = \frac{|\langle \psi_S | e^\dagger c | \psi_g \rangle|^2}{|\langle \psi_M | e^\dagger c | \psi_g \rangle|^2} = \left(\frac{\sin \theta' \cos \theta - \cos \theta' \sin \theta}{\cos \theta' \cos \theta + \sin \theta' \sin \theta} \right)^2 = \tan^2(\theta' - \theta), \quad (76)$$

where the labels M and S refer to the main and satellite peaks, respectively. Equation (76) demonstrates the important fact that the satellite intensity depends only on the difference in hybridization between the initial and final states. Thus, if the PE process induces no change in the hybridization ($\theta' = \theta$), then all intensity goes into the main peak and the satellite intensity vanishes. Since PES creates a hole in the core level, there will usually be a change in the energy difference between the two basis states due to screening such that $\Delta' \neq \Delta$ and a satellite peak will be present.

As an example, consider the ground state as a mixture of $|5f^n\rangle$ and $|5f^{n+1}\bar{k}\rangle$ and the final state as a mixture of $|\underline{c}5f^n\bar{e}\rangle$ and $|\underline{c}5f^{n+1}\bar{k}\bar{e}\rangle$, where \bar{k} denotes a reservoir of hole states near the Fermi level and \underline{c} denotes a core hole. The underlying physical picture is one in which the f electrons fluctuate among the two different atomic configurations by exchanging electrons with a reservoir. Quantum mechanically, the electrons can, for short periods of time, preserve their atomic character in a superposition of two atomic valence states with different numbers of $5f$ electrons while maintaining their metallic, delocalized hopping between neighboring sites. Correlations are strongest when the electrons are on the same atom. If the energy difference between the initial states is taken as Δ , then the energy difference between the final states is $\Delta' = \Delta - Q_{cf}$, where Q_{cf} is the $c - 5f$ Coulomb interaction. For $Q_{cf} = 0$ we obtain only the main peak. When the Coulomb interaction is switched on, the satellite peak appears. If $Q_{cf} > \Delta$, then the satellite peak is at a lower intensity than the main peak. This gives a well-screened peak that can have a higher intensity than the main peak, depending on the precise values of Q_{cf} , Δ , and V . In localized systems the core-hole potential gives rise to a poorly screened photoemission peak. In metallic systems, on the other hand, the core hole can be screened by valence electrons from surrounding atoms, giving

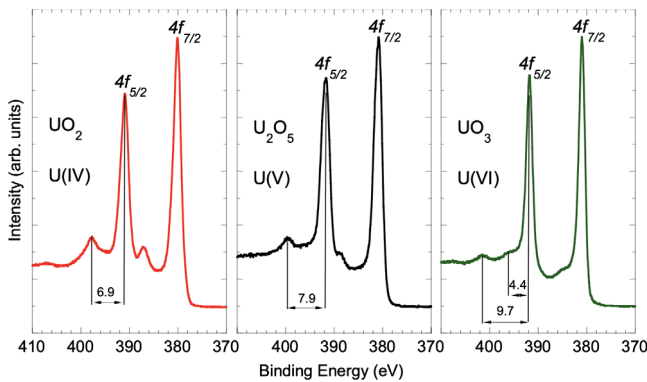


FIG. 34. Uranium $4f$ core-level x-ray photoemission spectra recorded for (left panel) U(IV) in UO_2 , (center panel) U(V) in U_2O_5 , and (right panel) U(VI) in UO_3 . The relative energy between the satellite peak and the $4f_{5/2}$ ($4f_{7/2}$) emission line is used as a marker for the oxidation state of the uranium atoms. From Gouder, Eloirdi, and Caciuffo, 2018.

rise to a well-screened peak, which is at a lower binding energy than the unscreened peak.

Apart from the satellite-to-main-peak intensity ratio, one can also look at their energy separation; see Eq. (75). Ilton and Bagus (2011) calculated peak separations to determine uranium oxidation states. Figure 34 shows the binding energy separation between primary U $4f$ peaks and associated satellites for different oxidation states of uranium (Gouder, Eloirdi, and Caciuffo, 2018). Satellite-primary peak binding energy separations, as well as intensities to a lesser extent, are relatively insensitive to composition and structure and can be used to both identify and help quantify U oxidation states in mixed valence phases.

B. ARPES

ARPES using a laboratory source was reported from Japan on the compound USb by Kumigashira *et al.* (2000). These results and calculations suggested that the $5f$ electrons in USb have a “dual character”: they are partly localized and partly itinerant. Earlier work had suggested that the $5f$ electrons in USb were almost fully localized, as are the $4f$ electrons in CeSb. The answer to this question may depend on the choice of the probe used for the investigation.

A first ARPES measurement at SPring-8 was reported in 2006 on the compound UFeGa₅ (Fujimori *et al.*, 2006), in which the $5f$ states are essentially itinerant and the spectra are well reproduced by LDA theory. The following year, they published a rather complete ARPES study of the superconducting (and antiferromagnetic) compound UPd₂Al₃ (Fujimori *et al.*, 2007).

In this material the photoemission experiments showed an increase of the weight of the $5f$ contribution, as the temperature was lowered, offering an explanation of why the high-temperature properties appear to show localized $5f$ states, whereas at the lowest temperatures, when the material becomes first an antiferromagnet and then (in addition) a superconductor, the $5f$ states are better described as itinerant; see Fig. 5 of Fujimori *et al.* (2007). These experiments used incident energies of 400 and 800 eV, where the difference in these two spectra can be related to that originating from the $5f$ states. They also demonstrated strongly dispersive $5f$ bands in the compound UB₂, in which the $5f$ bands are fully itinerant (Ohkochi *et al.*, 2008).

Given the intense interest in URu₂Si₂ it is not surprising that a major effort with ARPES has been made on this material. Durakiewicz (2014) considered all the work, which was done with both synchrotron and laboratory instruments. Many features of URu₂Si₂ were established using these techniques. One interesting aspect is that Durakiewicz concluded that the $5f$ count in this material is close to 2.6, whereas the previously discussed NIXS and RIXS experiments come out with a number closer to 2.0. Again, we emphasize that this number may be dependent on the technique used. A more recent study of ThRu₂Si₂ at SPring-8 (Fujimori *et al.*, 2017) showed the difference between this material, with no $5f$ states, and URu₂Si₂. Fujimori *et al.* concluded that there is a strong hybridization between the $5f$ states and the ligand states in URu₂Si₂.

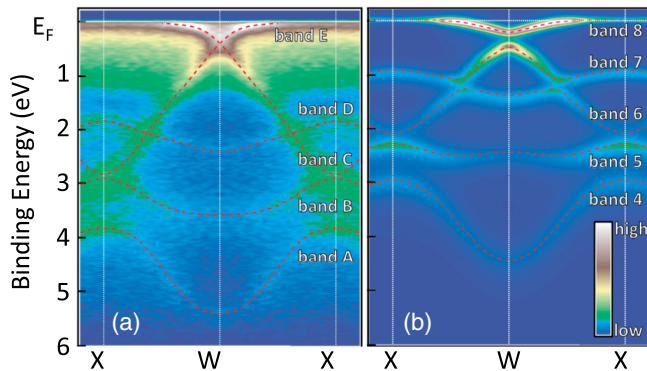


FIG. 35. ARPES spectra and comparison with the results of band-structure calculations for single crystals of UN. (a) Symmetrized ARPES spectra measured along the X-W-X line. Dashed curves are guides for the eye. (b) Simulation of ARPES spectra based on the band-structure calculation treating all U $5f$ electrons as itinerant. From Fujimori, Ohkochi *et al.*, 2012.

An interesting study at SPring-8 was performed on UN (Fujimori, Ohkochi *et al.*, 2012). This simple NaCl-structure-type compound has been controversial for many years, especially since the first investigations in the 1960s. The results from the ARPES experiments are shown in Fig. 35. Whereas not all the bands in the figure involve $5f$ states, there is strong evidence that all such $5f$ states are itinerant. These conclusions strongly support earlier neutron work (Holden *et al.*, 1984) as well as more recent RIXS experiments (Lawrence Bright *et al.*, 2023). Neither neutron nor RIXS work have observed any sign of the crystal-field states that are a major component of any $5f$ localization.

A good summary of the work published at SPring-8 was published by Fujimori *et al.* (2016) and the Los Alamos group (Beaux *et al.*, 2011), who performed experiments at both the ESRF and the Wisconsin synchrotron on uranium compounds, as well as with laboratory systems. Many of these experiments were performed with hard x-ray photoelectron spectroscopy, where the incident energies were as high as 7.6 keV, eliminating questions about whether the bulk properties were examined. In reviewing the experiments done at synchrotrons, Fujimori *et al.* (2016) pointed out that they used photon energies of between 400 and 500 eV, whereas laboratory experiments using the He-I and He-II radiations normally expend energies of less than 100 eV. As frequently discussed in this review, such low photon energies must be regarded as extremely surface sensitive (see Table I), so the conclusions may depend on the preparation of the surface and the ultra-vacuum conditions in the chamber.

More recent studies at SPring-8 have been made of the UX_3 ($X = \text{Al, Ga, and In}$) systems and a relatively complete picture of their Fermi surfaces has been elucidated (Fujimori, Kobata *et al.*, 2017). There are strong electron correlations in these systems, so the magnetic ordering is of the weakly itinerant $5f$ states. The mixing between the $5f$ and anion p states shows why a strong signal was obtained at the Ga K edge in UGa_3 in resonant diffraction experiments (Mannix *et al.*, 2001).

A recent study reported on UTe_2 , a material of much current interest (Ran *et al.*, 2019), and Shick, Fujimori, and Pickett (2021), concluded that there are both localized and itinerant

features seen in the angle-integrated spectra. They believed that the ground state is predominantly $5f^3$.

Finally, resonant photoemission was reported by the SPring-8 group for the first time on a series of U compounds (Fujimori *et al.*, 2019). This was performed by tuning the incident photons to the $N_{4,5}$ resonance, where the core $4d$ states are promoted to the empty $5f$ states and there is an enhancement of the signal arising from the $5f$ states. This is the same transition energy used for the successful RIXS work discussed in Sec. VII. The enhancement in the signal is less than that observed at the Ce $M_{4,5}$ edges ($3d \rightarrow 4f$) but can still be useful. Fujimori *et al.* (2019) found the enhancement at the two edges to be roughly equivalent. They reported scans on resonance (737 eV for the $N_5 4d_{5/2} \rightarrow 5f$) and off resonance at 725 eV, and then plotted the difference spectra. This is shown for UGa_2 and UPd_2Al_3 in Fig. 36.

Although UGa_2 (which is a ferromagnet with a large magnetic moment of $\sim 3\mu_B$) appears to have a localized $5f$ component (Kolomiets *et al.*, 2021), it is probably better to consider it as a band system. One can see some weight at E_F attributed to the U $5f$ states, even if the major weight is around -1 eV.

The series of experiments performed with ARPES at SPring-8 have been important in actinide research in a number of ways. Perhaps the most crucial aspect is that they have produced high-quality data that can be tested against the latest theoretical predictions. In this respect the resonance experiments described by Fujimori *et al.* (2019) are particularly valuable and have already shown that the behavior of the $5f$ electrons is often more complicated than expected; reproducing these results from first-principles theories is a considerable challenge. On the negative side, it is unfortunate that we have so little data on transuranium samples. Given that the detected particles are electrons, it is clear that the chambers would become contaminated if transuranium samples were used, as no encapsulation of the sample is possible with the technique. Whether this could be overcome with a determined effort is still unclear. However, imagine the information that could be obtained if resonant ARPES could be determined on the series $AnCoGa_5$ (with $An = \text{U, Np, and Pu}$). We could follow the $5f$ states as they progress from a probably itinerant $UCoGa_5$ to

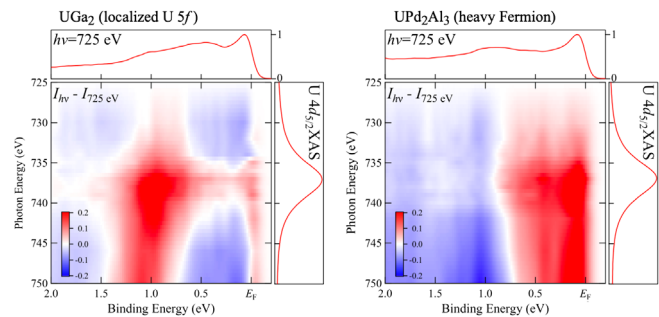


FIG. 36. Angle-integrated spectra showing the difference between photoemission spectroscopy taken with the energy tuned near the N_5 edge at 737 eV and the off-resonance condition of 725 eV. The $5f$ enhancement shows the weight of the signal in UGa_2 , where the $5f$ electrons are essentially localized, is ~ 1 eV below E_F , whereas in the heavy-fermion system UPd_2Al_3 they are basically at E_F . From Fujimori *et al.*, 2019.

the partial localization of the $5f$'s in NpCoGa_5 (which orders antiferromagnetically at 47 K with a magnetic moment of $0.8\mu_B$), and then to the heavy-fermion superconductor PuCoGa_5 , which has the highest T_c of any heavy-fermion material with $T_c = 18$ K. Many other such examples could be proposed, but this one is especially interesting, and it turns out that single crystals of all three of these compounds have been made in Japan.

XI. CONCLUSIONS

Actinides were examined soon after the first synchrotrons began operations in the late 1970s and 1980s, notably with XAS (Kalkowski, Kaindl, Bertram *et al.*, 1987; Bertram *et al.*, 1989), XMCD (Collins, Laundry, Tang, and van der Laan, 1995), and EXAFS measurements (Silva and Nitsche, 1995; Conradson *et al.*, 1998) at the actinide L edges, high-pressure experiments using energy dispersive detectors (Benedict and Holzapfel, 1993), and high-resolution XRD to investigate the fine details of the diffraction patterns (Grübel *et al.*, 1991). The success of these early-generation synchrotrons utilized across all parts of the periodic table led to more powerful light sources being built, and the advantages for the study of actinides increased. They now represent some of the most powerful tools available for this research.

This review has focused on experiments performed in the field of condensed-matter physics in the last 20 years at the ESRF, with references to work at other synchrotrons, notably Diamond Light Source, the APS, and SPring-8. Many experiments have been performed in the domains of chemistry and environmental science; efforts to study the dissolution of UO_2 in water (Springell *et al.*, 2015; Rennie, Lawrence Bright, Sutcliffe *et al.*, 2018) span these fields. They demand synchrotron radiation, as diffraction signals are required from epitaxial films having a thickness of < 10 nm.

To conclude the review, we highlight six examples that have been “game changers” for actinide research. The *first* (from Sec. IV.A) is the capability to observe samples at the microgram level, allowing pressures up to 100 GPa to be applied in diamond-anvil cells, and the development of the angular-dependent data collection is so sophisticated that data analysis can be used to determine the crystallographic structures; see Fig. 7. These experiments, extended to transuranium samples (Lindbaum *et al.*, 2001; Heathman *et al.*, 2005), illustrated the failure of the DFT for actinides and influenced the subsequent work with DMFT that is frequently mentioned in the review. These experiments could only have been done on third-generation synchrotrons.

The *second* example (from Sec. IV.D) concerns the field of materials science and involves narrow beams of usually high-energy photons (often $E > 40$ keV). Combined with tomography, this gives an extremely detailed view of defects and pore structure, and unlike the electron microscope the technique is nondestructive. Figure 12 gives one example (Thomas *et al.*, 2020). This field may also benefit from the time structure of future FELs, as one can imagine materials subjected to various dynamical stresses and being able to follow the microscopic changes, again in a nondestructive way.

The *third* example (from Sec. V.A) is the discovery in the actinide oxides and UPd_3 of ordering of the electric-quadrupole moments (Santini *et al.*, 2009) below room temperature. In this case, intensity is not always the main problem, but complex instrumentation is needed to measure the polarization dependence of the scattered photons and their azimuthal dependence; see Fig. 15. In the case of NpO_2 , the nature of the phase transition at 25 K (Paixão *et al.*, 2002) had been the source of speculation for more than 50 years. How common this phenomenon is in the actinides is still an open question, but the tools to determine such effects are now available.

The *fourth* example is that the development of the technique of XMCD (see Sec. VI.C) led to a direct method of determining the absolute values of the spin and orbital moments in actinide materials. Prior to this, the only technique available was using polarized neutrons, but doing so requires sizable single crystals. Now these quantities can be measured with micrograms of polycrystalline samples. The values, and especially their ratio, are of major importance for actinide research, as with itinerant $5f$ electrons there is a tendency for a partial quenching of the orbital moment (Lander, Brooks, and Johansson, 1991). Now that the $\langle T_z \rangle$ values calculated with intermediate coupling (van der Laan and Thole, 1996) can be used, the orbital-to-spin ratio is readily determined. Figure 23 represents perhaps the most convincing evidence given thus far that intermediate coupling is a crucial requirement of the physics and chemistry of actinide materials in general.

The *fifth* example concerns the inelastic scattering of x rays (Sec. IX). Here again the capability to determine the phonon spectra from micrograms of material as at the ID28 beamline has been of great importance. The phonons of δ -Pu [see Fig. 31 and Wong *et al.* (2003)] was a major achievement, especially since the theoretical work was actually published in advance (Dai *et al.*, 2003), and gave the first major credibility test of DMFT at that time. More recently the development of grazing incidence IXS has led to important new information on the radiation damage in UO_2 (Rennie, Lawrence Bright, Dambrough *et al.*, 2018) and on the complexity of the U-Mo alloy system; see Fig. 32. The sensitivity of these experiments is noteworthy, especially considering that the sample mass is less than 100 μg .

The measurement of ARPES from a large number of uranium compounds at the SPring-8 facility (our *sixth* example; Sec. X) represents a landmark for actinide research. The data, especially that using resonance at the uranium N edge, offer an unprecedented snapshot of the electronic structure and the role of the $5f$ states in these materials; see Figs. 35 and 36. Although considerable effort has already been expended to match these to present-day theory, they remain a challenge for future, no doubt more sophisticated, theories. As described, it is vital that ways be found to extend this work to transuranium materials so that a better overview of the changes in the $5f$ -electron behavior can be found as their number is increased.

The future of actinide research at synchrotrons is promising. A new generation of machines with the associated complex instrumentation is coming online that will benefit new initiatives. FELs with extremely high peak brightness and pulse durations from a few to hundreds of femtoseconds are

now starting to operate, pushing the timescale limits of spectroscopy and structure studies (Liermann *et al.*, 2021). Diffraction-limited storage rings such as MAX-IV in Sweden (Tavares *et al.*, 2018), Sirius in Brazil (Liu *et al.*, 2014), and ESRF-EBS in France (Raimondi, 2016; Chenevier and Joly, 2020), with emittance approaching the diffraction limit and delivering ultrasmall x-ray beam sizes, start demonstrating their potential as an extraordinarily powerful tool for the investigation of complex systems and emerging phenomena. These machines will provide an increase in average brightness and coherent flux of about 2 orders of magnitude compared to third-generation x-ray sources, with applications for high-pressure studies, microscopy, coherent diffraction, high-resolution imaging, and spectroscopy (Eriksson, van der Veen, and Quitmann, 2014; Frenkel and van Bokhoven, 2014). The possibility of achieving submicrometer focal-spot diameters at the sample position will extend the use of x-ray absorption and emission spectroscopy methods to single actinide nanoparticles and colloids, providing powerful characterization tools for the study of surface defects and particle-size-dependent structural details, which is important for a better understanding of environmental effects and catalytic properties. High-pressure diffraction experiments will provide benefits from both the higher brightness and the smaller beam size, giving access to higher pressures in smaller diamond-anvil cells (McMahon, 2014). For actinides, this will give us the opportunity to extend phase diagrams and observe the destabilization of localized $5f$ states in curium and beyond. All such instrumentation will greatly benefit our understanding of this complex row of elements in the periodic table. XPCS (Grübel and Zontone, 2004; Lim *et al.*, 2014) will benefit from the increased coherence of the incident beam, enabling studies of phase transitions and critical phenomena to be made in strongly correlated electron systems at picosecond timescales (Shpyrko, 2014). A source at the diffraction limit in the hard x-ray range with high coherent flux and an almost round beam footprint (thanks to the strongly reduced horizontal emittance) will make scanning coherent diffractive imaging techniques, such as x-ray ptychography (Thibault, Guizar-Sicairos, and Menzel, 2014), available for coherent imaging experiments on nuclear waste forms and irradiated fuels with mesoscopic spatial resolution between the nanometer and micrometer length scales. A strong reduction of the focus size will be reflected in an improved energy resolution of spectroscopy techniques, like IXS, RIXS, NIXS, and ARPES, enabling a precise observation to be made of magnetovibrational and multipole excitations, splitting of electronic multiplets by spin-orbit and crystal-field interactions, and dispersion of band-structure states (Rotenberg and Bostwick, 2014; Schmitt, De Groot, and Rubensson, 2014). This is particularly important for understanding the subtle interplay between competing interaction mechanisms in actinide materials poised at the brink of electronic, lattice, and magnetic instabilities.

ACKNOWLEDGMENTS

A number of colleagues from Joint Research Centre Karlsruhe, the Universities of Parma (Italy), Köln (Germany), and Oxford and Bristol (UK), the European

Synchrotron Radiation Facility, Diamond Light Source, the DESY synchrotron, Brookhaven and Los Alamos National Laboratories, and several other institutions have been involved in the studies presented in this review. The inspiration shown by the late Marty Blume at BNL in the early days of this research is gratefully acknowledged. We thankfully acknowledge M. Altarelli, L. Braicovich, S. P. Collins, A. Fujimori, G. Ghiringhelli, K. Kvashnina, and A. Severing for the helpful discussions. We thank the radioprotection services, and especially Patrick Colomp, at the ESRF for their collaboration in the safe running of transuranium experiments on (thus far) at least ten different beamlines.

REFERENCES

- Als-Nielsen, J., and D. McMorrow, 2011, *Elements of Modern X-Ray Physics*, 2nd ed. (John Wiley & Sons, New York).
- Altarelli, M., 2013, in *Magnetism and Synchrotron Radiation: Towards the Fourth Generation Light Sources*, Springer Proceedings in Physics Vol. 151, edited by E. Beaurepaire, H. Boulu, L. Joly, and F. Scheurer (Springer-Verlag, Berlin), pp. 95–138.
- Ament, L. J. P., G. Ghiringhelli, M. Moretti Sala, L. Braicovich, and J. van den Brink, 2009, *Phys. Rev. Lett.* **103**, 117003.
- Ament, L. J. P., M. van Veenendaal, T. P. Devereaux, J. P. Hill, and J. van den Brink, 2011, *Rev. Mod. Phys.* **83**, 705.
- Amidani, L., M. Retegan, A. Volkova, K. Popa, P. M. Martin, and K. O. Kvashnina, 2021, *Inorg. Chem.* **60**, 16286.
- Amidani, L., G. B. M. Vaughan, T. V. Plakhova, A. Y. Romanchuk, E. Gerber, R. Svetogorov, S. Weiss, Y. Joly, S. N. Kalmykov, and K. O. Kvashnina, 2021, *Chem. Eur. J.* **27**, 252.
- Amitsuka, H., T. Inami, M. Yokoyama, S. Takayama, Y. Ikeda, I. Kawasaki, Y. Homma, H. Hidaka, and T. Yanagisawa, 2010, *J. Phys. Conf. Ser.* **200**, 012007.
- Amorese, A., *et al.*, 2020, *Proc. Natl. Acad. Sci. U.S.A.* **117**, 30220.
- Amoretti, G., A. Blaise, R. Caciuffo, D. Di Cola, J. M. Fournier, M. T. Hutchings, G. H. Lander, R. Osborn, A. Severing, and A. D. Taylor, 1992, *J. Phys. Condens. Matter* **4**, 3459.
- Amoretti, G., A. Blaise, R. Caciuffo, J. M. Fournier, M. T. Hutchings, R. Osborn, and A. D. Taylor, 1989, *Phys. Rev. B* **40**, 1856.
- Antonio, D. J., *et al.*, 2021, *Commun. Mater.* **2**, 17.
- Antonio, R., L. Soderholm, C. W. Williams, J.-P. Blaudeau, and B. E. Bursten, 2001, *Radiochim. Acta* **89**, 17.
- Antonov, V. N., B. N. Harmon, O. V. Andryushchenko, L. V. Bekenev, and A. N. Yaresko, 2003, *Phys. Rev. B* **68**, 214425.
- Antonov, V. N., B. N. Harmon, and A. N. Yaresko, 2003, *Phys. Rev. B* **68**, 214424.
- Aoki, D., *et al.*, 2007, *J. Phys. Soc. Jpn.* **76**, 063701.
- Arko, A. J., J. J. Joyce, L. Morales, J. Wills, J. Lashley, F. Wastin, and J. Rebizant, 2000, *Phys. Rev. B* **62**, 1773.
- Bagus, P. S., B. Schacherl, and T. Vitova, 2021, *Inorg. Chem.* **60**, 16090.
- Bahl, S., *et al.*, 2017, *Inorg. Chem.* **56**, 13982.
- Bao, H., *et al.*, 2018, *Inorg. Chem.* **57**, 11404.
- Bao, Z., *et al.*, 2013, *Phys. Rev. B* **88**, 134426.
- Bargar, J. R., G. E. J. Brown, I. Evans, T. Rabedeau, M. Rowen, and J. Rogers, 2002, in *Proceedings of the 2nd Euroconference and NEA Workshop on Speciation, Techniques, and Facilities for Radioactive Materials at Synchrotron Light Sources, Grenoble, France, 2000*, edited by T. Reich and D. K. Shuh (OECD Publications, Paris), pp. 169–176.
- Beaux, M., *et al.*, 2011, *J. Electron Spectrosc. Relat. Phenom.* **184**, 517.

- Benedict, U., and W. B. Holzapfel, 1993, in *Handbook of Physics and Chemistry of Rare Earths*, Vol. 17, edited by K. A. Gschneidner, L. Eyring, G. H. Lander, and G. R. Choppin (North-Holland, Amsterdam), Chap. 113, p. 245.
- Berger, M. J., J. H. Hubbell, S. M. Seltzer, J. Chang, J. S. Coursey, R. Sukumar, D. S. Zucker, and K. Olsen, 2010, <http://physics.nist.gov/xcom>.
- Bernhoeft, N., A. Hiess, S. Langridge, A. Stunault, D. Wermeille, C. Vettier, G. H. Lander, M. Huth, M. Jourdan, and H. Adrian, 1998, *Phys. Rev. Lett.* **81**, 3419.
- Bernhoeft, N., G. H. Lander, M. J. Longfield, S. Langridge, D. Mannix, S. D. Brown, W. J. Nuttall, A. Hiess, C. Vettier, and P. Lejay, 2004, *J. Phys. Condens. Matter* **16**, 3869.
- Bernhoeft, N., J. A. Paixão, C. Detlefs, S. B. Wilkins, P. Javorský, E. Blackburn, and G. H. Lander, 2004, *Phys. Rev. B* **69**, 174415.
- Bertram, S., G. Kaindl, J. Jové, M. Pagès, and J. Gal, 1989, *Phys. Rev. Lett.* **63**, 2680.
- Bes, R., G. Leinders, and K. Kvashnina, 2022, *J. Synchrotron Radiat.* **29**, 21.
- Bès, R., M. Rivenet, P.-L. Solari, K. O. Kvashnina, A. C. Scheinost, and P. M. Martin, 2016, *Inorg. Chem.* **55**, 4260.
- Bevan, D. J. M., I. E. Grey, and B. T. M. Willis, 1986, *J. Solid State Chem.* **61**, 1.
- Bhattacharyya, A., and P. K. Mohapatra, 2019, *Radiochim. Acta* **107**, 931.
- Blackburn, E., and N. Bernhoeft, 2006, *J. Phys. Soc. Jpn.* **75**, 63.
- Blackburn, E., R. Caciuffo, N. Magnani, P. Santini, P. J. Brown, M. Enderle, and G. H. Lander, 2005, *Phys. Rev. B* **72**, 184411.
- Blackburn, E., *et al.*, 2006, *Philos. Mag.* **86**, 2553.
- Blume, M., 1985, *J. Appl. Phys.* **57**, 3615.
- Blume, M., and D. Gibbs, 1988, *Phys. Rev. B* **37**, 1779.
- Boeuf, A., R. Caciuffo, J. M. Fournier, L. Manes, J. Rebizant, F. Rustichelli, and J. C. Spirlet, 1983, *Phys. Status Solidi A* **79**, K1.
- Böhler, R., *et al.*, 2014, *J. Nucl. Mater.* **448**, 330.
- Bohr, J., D. Gibbs, and K. Huang, 1990, *Phys. Rev. B* **42**, 4322.
- Bolvin, H., U. Wahlgren, H. Moll, T. Reich, G. Geipel, T. Fanghänel, and I. Grenthe, 2001, *J. Phys. Chem. A* **105**, 11441.
- Bonato, L., *et al.*, 2020, *Nanoscale Adv.* **2**, 214.
- Bonnin, A., J. P. Wright, R. Tucoulou, and H. Palanchar, 2014, *Appl. Phys. Lett.* **105**, 084103.
- Booth, C., *et al.*, 2012, *Proc. Natl. Acad. Sci. U.S.A.* **109**, 10205.
- Booth, C. H., E. D. Bauer, M. Daniel, R. E. Wilson, J. N. Mitchell, L. A. Morales, J. L. Sarrao, and P. G. Allen, 2007, *Phys. Rev. B* **76**, 064530.
- Booth, C. H., S. A. Medling, J. G. Tobin, R. E. Baumbach, E. D. Bauer, D. Sokaras, D. Nordlund, and T.-C. Weng, 2016, *Phys. Rev. B* **94**, 045121.
- Booth, C. H., *et al.*, 2014, *J. Electron Spectrosc. Relat. Phenom.* **194**, 57.
- Borca, C. N., D. Grolimund, M. Willmann, B. Meyer, K. Jefimovs, J. Vila-Comamala, and C. David, 2009, *J. Phys. Conf. Ser.* **186**, 012003.
- Borgatti, F., G. Ghiringhelli, P. Ferriani, G. Ferrari, G. van der Laan, and C. M. Bertoni, 2004, *Phys. Rev. B* **69**, 134420.
- Bosak, A., and M. Krisch, 2005, *Phys. Rev. B* **72**, 224305.
- Boubals, N., *et al.*, 2017, *Inorg. Chem.* **56**, 7861.
- Bouchet, J., 2008, *Phys. Rev. B* **77**, 024113.
- Bradley, J. A., S. Sen Gupta, G. T. Seidler, K. T. Moore, M. W. Haverkort, G. A. Sawatzky, S. D. Conradson, D. L. Clark, S. A. Koziomor, and K. S. Boland, 2010, *Phys. Rev. B* **81**, 193104.
- Braicovich, L., *et al.*, 2010, *Phys. Rev. Lett.* **104**, 077002.
- Bridges, F., R. Dudschus, C. Mackeen, T. Keiber, C. H. Booth, and M. B. Maple, 2020, *Phys. Rev. B* **102**, 014109.
- Broholm, C., H. Lin, P. T. Matthews, T. E. Mason, W. J. L. Buyers, M. F. Collins, A. A. Menovsky, J. A. Mydosh, and J. K. Kjems, 1991, *Phys. Rev. B* **43**, 12809.
- Brubaker, Z. E., S. Ran, A. H. Said, M. E. Manley, P. Söderlind, D. Rosas, Y. Idell, R. J. Zieve, N. P. Butch, and J. R. Jeffries, 2019, *Phys. Rev. B* **100**, 094311.
- Brunel, M., and F. de Bergevin, 1981, *Acta Crystallogr. Sect. A* **37**, 324.
- Burkel, E., 2000, *Rep. Prog. Phys.* **63**, 171.
- Burlet, P., J. Rossat-Mignod, S. Quezel, O. Vogt, J. C. Spirlet, and J. Rebizant, 1986, *J. Less-Common Met.* **121**, 121.
- Burns, P. C., K. A. Kubatko, G. Sigmon, B. J. Fryer, J. E. Gagnon, M. R. Antonio, and L. Soderholm, 2005, *Angew. Chem., Int. Ed. Engl.* **44**, 2135.
- Butchers, M. W., J. A. Duffy, J. W. Taylor, S. R. Giblin, S. B. Dugdale, C. Stock, P. H. Tobash, E. D. Bauer, and C. Paulsen, 2015, *Phys. Rev. B* **92**, 121107.
- Butorin, S. M., 2020, *Inorg. Chem.* **59**, 16251.
- Butorin, S. M., K. O. Kvashnina, A. L. Smith, K. Popa, and P. M. Martin, 2016, *Chem. Eur. J.* **22**, 9693.
- Butorin, S. M., K. O. Kvashnina, J. R. Vegelius, D. Meyer, and D. K. Shuh, 2016, *Proc. Natl. Acad. Sci. U.S.A.* **113**, 8093.
- Butorin, S. M., A. Modin, J. R. Vegelius, K. O. Kvashnina, and D. K. Shuh, 2016, *J. Phys. Chem. C* **120**, 29397.
- Caciuffo, R., 2014, *C.R. Phys.* **15**, 553.
- Caciuffo, R., E. C. Buck, D. L. Clark, and G. van der Laan, 2010, *MRS Bull.* **35**, 889.
- Caciuffo, R., and G. H. Lander, 2021, *J. Synchrotron Radiat.* **28**, 1692.
- Caciuffo, R., G. H. Lander, J. C. Spirlet, J. M. Fournier, and W. F. Kuhs, 1987, *Solid State Commun.* **64**, 149.
- Caciuffo, R., N. Magnani, P. Santini, S. Carretta, G. Amoretti, E. Blackburn, M. Enderle, P. J. Brown, and G. H. Lander, 2007, *J. Magn. Magn. Mater.* **310**, 1698.
- Caciuffo, R., J. A. Paixao, C. Detlefs, M. J. Longfield, P. Santini, N. Bernhoeft, J. Rebizant, and G. H. Lander, 2003, *J. Phys. Condens. Matter* **15**, S2287.
- Caciuffo, R., L. Paolasini, A. Sollier, P. Ghigna, E. Pavarini, J. van den Brink, and M. Altarelli, 2002, *Phys. Rev. B* **65**, 174425.
- Caciuffo, R., G. van der Laan, L. Simonelli, T. Vitova, C. Mazzoli, M. A. Denecke, and G. H. Lander, 2010, *Phys. Rev. B* **81**, 195104.
- Carra, P., M. Fabrizio, and B. T. Thole, 1995, *Phys. Rev. Lett.* **74**, 3700.
- Carra, P., B. T. Thole, M. Altarelli, and X. Wang, 1993, *Phys. Rev. Lett.* **70**, 694.
- Carter, K. P., *et al.*, 2021, *Nature (London)* **590**, 85.
- Chandra, P., P. Coleman, and R. Flint, 2015, *Phys. Rev. B* **91**, 205103.
- Chaney, D., *et al.*, 2021, *Phys. Rev. Mater.* **5**, 035004.
- Chenevier, D., and A. Joly, 2020, *Synchrotron Radiat. News* **33**, 37.
- Chernyshov, A. A., A. A. Veligzhanin, and Y. V. Zubavichus, 2009, *Nucl. Instrum. Methods Phys. Res., Sect. A* **603**, 95.
- Clark, D. L., D. R. Janecky, and L. J. Lane, 2006, *Phys. Today* **59**, No. 9, 34.
- Coleman, P., 2007, in *Handbook of Magnetism and Advanced Magnetic Materials*, Vol. 1, edited by H. Kronmüller and S. S. P. Parkin (John Wiley & Sons, New York), pp. 95–148.
- Collins, S. P., D. Laundry, C. C. Tang, and R. J. Cernik, 1995, *J. Phys. Condens. Matter* **7**, L223.
- Collins, S. P., D. Laundry, C. C. Tang, and G. van der Laan, 1995, *J. Phys. Condens. Matter* **7**, 9325.
- Conradson, S. D., I. Al Mahamid, D. L. Clark, N. J. Hess, E. A. Hudson, M. P. Neu, P. D. Palmer, W. H. Runde, and C. D. Tait, 1998, *Polyhedron* **17**, 599.

- Conradson, S. D., D. Manara, F. Wastin, D. L. Clark, G. H. Lander, L. A. Morales, J. Rebizant, and V. V. Rondinella, 2004, *Inorg. Chem.* **43**, 6922.
- Conradson, S. D., *et al.*, 2004a, *Inorg. Chem.* **43**, 116.
- Conradson, S. D., *et al.*, 2004b, *J. Am. Chem. Soc.* **126**, 13443.
- Conradson, S. D., *et al.*, 2005, *J. Solid State Chem.* **178**, 521.
- Conradson, S. D., *et al.*, 2013, *Phys. Rev. B* **88**, 115135.
- Cooper, R. I., and B. T. M. Willis, 2004, *Acta Crystallogr. Sect. A* **60**, 322.
- Cot-Auriol, M., M. Viro, C. Micheau, T. Dumas, X. Le Goff, C. Den Auwer, O. Diat, P. Moisy, and S. I. Nikitenko, 2021, *Dalton Trans.* **50**, 11498.
- Cowan, R. D., 1981, *The Theory of Atomic Structure and Spectra* (University of California Press, Berkeley, CA).
- Cromer, D. T., and D. Liberman, 1970, *J. Chem. Phys.* **53**, 1891.
- Cross, J. O., M. Newville, J. J. Rehr, L. B. Sorensen, C. E. Bouldin, G. Watson, T. Gouder, G. H. Lander, and M. I. Bell, 1998, *Phys. Rev. B* **58**, 11215.
- Crummett, W. P., H. G. Smith, R. M. Nicklow, and N. Wakabayashi, 1979, *Phys. Rev. B* **19**, 6028.
- Daghero, D., M. Tortello, G. A. Ummarino, J.-C. Griveau, E. Colineau, R. Eloirdi, A. B. Shick, J. Kolorenc, A. I. Lichtenstein, and R. Caciuffo, 2012, *Nat. Commun.* **3**, 786.
- Dai, X., S. Y. Savrasov, G. Kotliar, A. Migliori, H. Ledbetter, and E. Abrahams, 2003, *Science* **300**, 953.
- Dalmas de Réotier, P., J.-P. Sanchez, and A. Yaouanc, 1998, *J. Alloys Compd.* **271–273**, 414.
- Dalmas de Réotier, P., A. Yaouanc, G. van der Laan, N. Kernavanois, J.-P. Sanchez, J. L. Smith, A. Hiess, A. Huxley, and A. Rogalev, 1999, *Phys. Rev. B* **60**, 10606.
- Dalmas de Réotier, P., *et al.*, 1997, *J. Phys. Condens. Matter* **9**, 3291.
- Dalodière, E., *et al.*, 2017, *Sci. Rep.* **7**, 43514.
- Dardenne, K., B. Brendebach, M. A. Denecke, X. Liu, J. Rothe, and T. Vitova, 2009, *J. Phys. Conf. Ser.* **190**, 012037.
- Dambrough, J. E., R. M. Harker, I. Griffiths, D. Wermeille, G. H. Lander, and R. Springell, 2018, *J. Nucl. Mater.* **502**, 9.
- Das, T., J.-X. Zhu, and M. J. Graf, 2015, *Sci. Rep.* **5**, 8632.
- d'Astuto, M., P. K. Mang, P. Giura, A. Shukla, P. Ghigna, A. Mirone, M. Braden, M. Greven, M. Krisch, and F. Sette, 2002, *Phys. Rev. Lett.* **88**, 167002.
- de Bergevin, F., and M. Brunel, 1981, *Acta Crystallogr. Sect. A* **37**, 314.
- Degueldre, C., C. Cozzo, M. Martin, D. Grolimund, and C. Mieszczynski, 2013, *J. Solid State Chem.* **202**, 315.
- Degueldre, C., M. Martin, G. Kuri, D. Grolimund, and C. Borca, 2011, *J. Nucl. Mater.* **416**, 142.
- Denecke, M. A., 2006, *Coord. Chem. Rev.* **250**, 730.
- Denning, R. G., J. C. Green, T. E. Hutchings, C. Dallera, A. Tagliaferri, K. Giarda, N. B. Brookes, and L. Braicovich, 2002, *J. Chem. Phys.* **117**, 8008.
- Detlefs, B., S. B. Wilkins, R. Caciuffo, J. A. Paixão, K. Kaneko, F. Honda, N. Metoki, N. Bernhoeft, J. Rebizant, and G. H. Lander, 2008, *Phys. Rev. B* **77**, 024425.
- Detlefs, B., S. B. Wilkins, P. Javorský, E. Blackburn, and G. H. Lander, 2007, *Phys. Rev. B* **75**, 174403.
- Detlefs, C., F. Duc, Z. A. Kazej, J. Vanacken, P. Frings, W. Bras, J. E. Lorenzo, P. C. Canfield, and G. L. J. A. Rikken, 2008, *Phys. Rev. Lett.* **100**, 056405.
- Dewaele, A., J. Bouchet, F. Occelli, M. Hanfland, and G. Garbarino, 2013, *Phys. Rev. B* **88**, 134202.
- Dieste, O., T. Wiss, J.-C. Griveau, R. J. M. Konings, G. van der Laan, and R. Caciuffo, 2019, *Mater. Res. Express* **6**, 026307.
- Ding, H., *et al.*, 2021, *J. Mater. Chem. A* **9**, 12612.
- dos Reis, R. D., L. S. I. Veiga, C. A. Escanhoela, Jr., J. C. Lang, Y. Joly, F. G. Gandra, D. Haskel, and N. M. Souza-Neto, 2017, *Nat. Commun.* **8**, 1203.
- Dressler, A., T. Le Nedelec, A. Leydier, F. Cuer, T. Dumas, and A. Grandjean, 2022, *Chem. Eng. J. Adv.* **9**, 100225.
- Dudarev, S. L., P. Liu, D. A. Andersson, C. R. Stanek, T. Ozaki, and C. Franchini, 2019, *Phys. Rev. Mater.* **3**, 083802.
- Dumas, T., M. Viro, D. Menut, C. Tamain, C. Micheau, S. Dourdain, and O. Diat, 2022, *J. Synchrotron Radiat.* **29**, 30.
- Durakiewicz, T., 2014, *Philos. Mag.* **94**, 3723.
- Edmonds, A. R., 1957, *Angular Momentum in Quantum Mechanics* (Princeton University Press, Princeton, NJ).
- Eloirdi, R., C. Giacobbe, P. A. Celdran, N. Magnani, G. H. Lander, J.-C. Griveau, E. Colineau, K. Miyake, and R. Caciuffo, 2017, *Phys. Rev. B* **95**, 094517.
- Eloirdi, R., L. Havela, T. Gouder, A. Shick, J. Rebizant, F. Huber, and R. Caciuffo, 2009, *J. Nucl. Mater.* **385**, 8.
- Eriksson, M., J. F. van der Veen, and C. Quitmann, 2014, *J. Synchrotron Radiat.* **21**, 837.
- Estevenon, P., T. Dumas, P. L. Solari, E. Welcomme, S. Szenknect, A. Mesbah, K. O. Kvashnina, P. Moisy, C. Poinssot, and N. Dacheux, 2021, *Dalton Trans.* **50**, 12528.
- Faber, J., G. H. Lander, and B. R. Cooper, 1975, *Phys. Rev. Lett.* **35**, 1770.
- Ferrier, M. G., B. W. Stein, S. E. Bone, S. K. Cary, A. S. Ditter, S. A. Kozimor, J. S. Lezama Pacheco, V. Mocko, and G. T. Seidler, 2018, *Chem. Sci.* **9**, 7078.
- Finazzi, M., P. Sainctavit, A.-M. Dias, J.-P. Kappler, G. Krill, J.-P. Sanchez, P. Dalmas de Réotier, A. Yaouanc, A. Rogalev, and J. Goulon, 1997, *Phys. Rev. B* **55**, 3010.
- Forte, F., L. J. P. Ament, and J. van den Brink, 2008, *Phys. Rev. B* **77**, 134428.
- Fournier, J. M., A. Blaise, G. Amoretti, R. Caciuffo, J. Larroque, M. T. Hutchings, R. Osborn, and A. D. Taylor, 1991, *Phys. Rev. B* **43**, 1142.
- Frenkel, A. I., and J. A. van Bokhoven, 2014, *J. Synchrotron Radiat.* **21**, 1084.
- Fujimori, S.-i., M. Kobata, Y. Takeda, T. Okane, Y. Saitoh, A. Fujimori, H. Yamagami, Y. Haga, E. Yamamoto, and Y. Ōnuki, 2017, *Phys. Rev. B* **96**, 115126.
- Fujimori, S.-i., M. Kobata, Y. Takeda, T. Okane, Y. Saitoh, A. Fujimori, H. Yamagami, Y. Haga, E. Yamamoto, and Y. Ōnuki, 2019, *Phys. Rev. B* **99**, 035109.
- Fujimori, S.-i., T. Ohkochi, T. Okane, Y. Saitoh, A. Fujimori, H. Yamagami, Y. Haga, E. Yamamoto, and Y. Ōnuki, 2012, *Phys. Rev. B* **86**, 235108.
- Fujimori, S.-i., Y. Takeda, T. Okane, Y. Saitoh, A. Fujimori, H. Yamagami, Y. Haga, E. Yamamoto, and Y. Ōnuki, 2016, *J. Phys. Soc. Jpn.* **85**, 062001.
- Fujimori, S.-i., *et al.*, 2006, *Phys. Rev. B* **73**, 125109.
- Fujimori, S.-i., *et al.*, 2012, *J. Phys. Soc. Jpn.* **81**, 014703.
- Fujimori, S.-i., *et al.*, 2017, *Phys. Rev. B* **96**, 125117.
- Fujimori, S.-i., Y. Saitoh, T. Okane, A. Fujimori, H. Yamagami, Y. Haga, E. Yamamoto, and Y. Ōnuki, 2007, *Nat. Phys.* **3**, 618.
- Ganguly, G., D.-C. Sergentu, and J. Autschbach, 2020, *Chem. Eur. J.* **26**, 1776.
- Gaona, X., E. Wieland, J. Tits, A. C. Scheinost, and R. Dahn, 2013, *Appl. Geochem.* **28**, 109.
- Gardner, D. R., C. J. Bonnoit, R. Chisnell, A. H. Said, B. M. Leu, T. J. Williams, G. M. Luke, and Y. S. Lee, 2016, *Phys. Rev. B* **93**, 075123.
- Garrido, F., A. C. Hannon, R. M. Ibberson, L. Nowicki, and B. T. M. Willis, 2006, *Inorg. Chem.* **45**, 8408.

- Gerber, E., A. Y. Romanchuk, S. Weiss, A. Kuzenkova, M. O. J. Y. Hunault, S. Bauters, A. Egorov, S. M. Butorin, S. N. Kalmykov, and K. O. Kvashnina, 2022, *Environ. Sci. Nano* **9**, 1509.
- Gerber, E., *et al.*, 2020, *Nanoscale* **12**, 18039.
- Gerber, E., *et al.*, 2021, *Inorg. Chem. Front.* **8**, 1102.
- Gerken, F., and J. Schmidt-May, 1983, *J. Phys. F* **13**, 1571.
- Ghiringhelli, G., N. B. Brookes, E. Annese, H. Berger, C. Dallera, M. Griioni, L. Perfetti, A. Tagliaferri, and L. Braicovich, 2004, *Phys. Rev. Lett.* **92**, 117406.
- Gibbs, D., D. R. Harshman, E. D. Isaacs, D. B. McWhan, D. Mills, and C. Vettier, 1988, *Phys. Rev. Lett.* **61**, 1241.
- Glasauer, S., S. C. Fakra, S. Schooling, P. Weidler, T. Tylliszczak, and D. K. Shuh, 2022, *Chem. Geol.* **591**, 120726.
- Glatzel, P., A. Harris, P. Marion, M. Sikora, T.-C. Weng, C. Guilloud, S. Lafuerza, M. Rovezzi, B. Detlefs, and L. Ducotté, 2021, *J. Synchrotron Radiat.* **28**, 362.
- Gordon, R. A., G. T. Seidler, T. T. Fister, M. W. Haverkort, G. A. Sawatzky, A. Tanaka, and T. K. Sham, 2008, *Europhys. Lett.* **81**, 26004.
- Gouder, T., R. Eloirdi, and R. Caciuffo, 2018, *Sci. Rep.* **8**, 8306.
- Gouder, T., L. Havela, F. Wastin, and J. Rebizant, 2001, *Europhys. Lett.* **55**, 705.
- Gouder, T., P. M. Oppeneer, F. Huber, F. Wastin, and J. Rebizant, 2005, *Phys. Rev. B* **72**, 115122.
- Gouder, T., G. van der Laan, A. B. Shick, R. G. Haire, and R. Caciuffo, 2011, *Phys. Rev. B* **83**, 125111.
- Gouder, T., F. Wastin, J. Rebizant, and L. Havela, 2000, *Phys. Rev. Lett.* **84**, 3378.
- Goulon, J., C. Goulon-Ginet, R. Cortes, and J. M. Dubois, 1982, *J. Phys. (Paris)* **43**, 539.
- Griveau, J.-C., J. Rebizant, G. H. Lander, and G. Kotliar, 2005, *Phys. Rev. Lett.* **94**, 097002.
- Grübel, G., J. D. Axe, D. Gibbs, G. H. Lander, J. C. Marmeggi, and T. Brückel, 1991, *Phys. Rev. B* **43**, 8803.
- Grübel, G., and F. Zontone, 2004, *J. Alloys Compd.* **362**, 3.
- Gumenuik, R., K. O. Kvashnina, W. Schnelle, A. Leithe-Jasper, and Y. Grin, 2015, *Phys. Rev. B* **91**, 094110.
- Gumenuik, R., A. N. Yaresko, W. Schnelle, M. Nicklas, K. O. Kvashnina, C. Hennig, Y. Grin, and A. Leithe-Jasper, 2018, *Phys. Rev. B* **97**, 174405.
- Guo, X., X. Lü, J. T. White, C. J. Benmore, A. T. Nelson, R. C. Roback, and H. Xu, 2019, *J. Nucl. Mater.* **523**, 135.
- Gurtubay, I. G., J. M. Pitarke, W. Ku, A. G. Eguluz, B. C. Larson, J. Tischler, P. Zschack, and K. D. Finkelstein, 2005, *Phys. Rev. B* **72**, 125117.
- Hagen, M., W. G. Stirling, and G. H. Lander, 1988, *Phys. Rev. B* **37**, 1846.
- Haire, R. G., S. Heathman, M. Idiri, T. Le Bihan, A. Lindbaum, and J. Rebizant, 2003, *Phys. Rev. B* **67**, 134101.
- Halevy, I., *et al.*, 2012, *Phys. Rev. B* **85**, 014434.
- Hannon, J., G. Trammell, M. Blume, and D. Gibbs, 1988, *Phys. Rev. Lett.* **61**, 1245.
- Havela, L., T. Gouder, F. Wastin, and J. Rebizant, 2002, *Phys. Rev. B* **65**, 235118.
- Havela, L., F. Wastin, J. Rebizant, and T. Gouder, 2003, *Phys. Rev. B* **68**, 085101.
- Haverkort, M. W., A. Tanaka, L. H. Tjeng, and G. A. Sawatzky, 2007, *Phys. Rev. Lett.* **99**, 257401.
- Heathman, S., R. G. Haire, T. Le Bihan, A. Lindbaum, M. Idiri, P. Normile, S. Li, R. Ahuja, B. Johansson, and G. H. Lander, 2005, *Science* **309**, 110.
- Heathman, S., R. G. Haire, T. Le Bihan, A. Lindbaum, K. Litfin, Y. Méresse, and H. Libotte, 2000, *Phys. Rev. Lett.* **85**, 2961.
- Heathman, S., T. Le Bihan, S. Yagoubi, B. Johansson, and R. Ahuja, 2013, *Phys. Rev. B* **87**, 214111.
- Heathman, S., J.-P. Rueff, L. Simonelli, M. A. Denecke, J.-C. Griveau, R. Caciuffo, and G. H. Lander, 2010, *Phys. Rev. B* **82**, 201103(R).
- Hen, A., *et al.*, 2014, *Phys. Rev. B* **90**, 054408.
- Hen, A., *et al.*, 2015, *Phys. Rev. B* **92**, 024410.
- Henke, B. L., E. M. Gullikson, and J. C. Davis, 1993, *At. Data Nucl. Data Tables* **54**, 181.
- Hiess, A., A. Stunault, E. Colineau, J. Rebizant, F. Wastin, R. Caciuffo, and G. H. Lander, 2008, *Phys. Rev. Lett.* **100**, 076403.
- Hill, A. H., T. Klimczuk, R. Springell, and H. C. Walker, 2013, *J. Appl. Crystallogr.* **46**, 567.
- Hill, J. P., and D. F. McMorrow, 1996, *Acta Crystallogr. Sect. A* **52**, 236.
- Hiranaka, Y., *et al.*, 2013, *J. Phys. Soc. Jpn.* **82**, 083708.
- Hirao, N., S. I. Kawaguchi, K. Hirose, K. Shimizu, E. Ohtani, and Y. Ohishi, 2020, *Matter Radiat. Extremes* **5**, 018403.
- Holden, T. M., W. J. L. Buyers, E. C. Svensson, and G. H. Lander, 1984, *Phys. Rev. B* **30**, 114.
- Honda, F., N. Kawamura, D. Li, Y. Hirose, Y. Homma, A. Nakamura, Y. Shimizu, A. Maurya, Y. J. Sato, and D. Aoki, 2020, *JPS Conf. Proc.* **29**, 013002.
- Hubert, S., J. Purans, G. Heisbourg, P. Moisy, and N. Dacheux, 2006, *Inorg. Chem.* **45**, 3887.
- Hudry, D., *et al.*, 2014, *Chem. Eur. J.* **20**, 10431.
- Hurley, D. H., *et al.*, 2022, *Chem. Rev.* **122**, 3711.
- Husar, R., T. Dumas, M. L. Schlegel, D. Schlegel, D. Guillaumont, P.-L. Solari, and P. Moisy, 2022, *J. Synchrotron Radiat.* **29**, 1.
- Ikeda-Ohno, A., C. Hennig, A. Rossberg, A. Funke, A. C. Scheinost, G. Bernhard, and T. Yaita, 2008, *Inorg. Chem.* **47**, 8294.
- Ilton, E. S., and P. S. Bagus, 2011, *Surf. Interface Anal.* **43**, 1549.
- Isaacs, E. D., D. B. McWhan, R. N. Kleiman, D. J. Bishop, G. E. Ice, P. Zschack, B. D. Gaulin, T. E. Mason, J. D. Garrett, and W. J. L. Buyers, 1990, *Phys. Rev. Lett.* **65**, 3185.
- Isaacs, E. D., D. B. McWhan, C. Peters, G. E. Ice, D. P. Siddons, J. B. Hastings, C. Vettier, and O. Vogt, 1989, *Phys. Rev. Lett.* **62**, 1671.
- Jaime, M., *et al.*, 2017, *Nat. Commun.* **8**, 99.
- Janoschek, M., D. Haskel, J. Fernandez-Rodriguez, M. van Veenendaal, J. Rebizant, G. H. Lander, J.-X. Zhu, J. D. Thompson, and E. D. Bauer, 2015, *Phys. Rev. B* **91**, 035117.
- Jeffries, J. R., K. T. Moore, N. P. Butch, and M. B. Maple, 2010, *Phys. Rev. B* **82**, 033103.
- Jeffries, J. R., P. Söderlind, H. Cynn, A. Landa, W. J. Evans, S. T. Weir, Y. K. Vohra, and G. H. Lander, 2013, *Phys. Rev. B* **87**, 214104.
- Jegou, C., M. Odorowski, V. Kerleguer, V. Broudic, M. L. Schlegel, G. Jouan, C. Marques, and L. De Windt, 2022, *Corros. Sci.* **195**, 109964.
- Jensen, J., and P. Bak, 1981, *Phys. Rev. B* **23**, 6180.
- Jones, D. J., J. Roziere, G. C. Allen, and P. A. Tempest, 1986, *J. Chem. Phys.* **84**, 6075.
- Joyce, J. J., and G. H. Lander, 2019, in *Plutonium Handbook*, edited by D. L. Clark, D. A. Geeson, and R. J. Hanrahan (American Nuclear Society, Oak Brook, IL), Chap. 15, p. 1203.
- Joyce, J. J., J. M. Wills, T. Durakiewicz, M. T. Butterfield, E. Guziewicz, J. L. Sarrao, L. A. Morales, A. J. Arko, and O. Eriksson, 2003, *Phys. Rev. Lett.* **91**, 176401.
- Jutier, F., G. A. Ummarino, J.-C. Griveau, F. Wastin, E. Colineau, J. Rebizant, N. Magnani, and R. Caciuffo, 2008, *Phys. Rev. B* **77**, 024521.
- Kalkowski, G., G. Kaindl, S. Bertram, G. Schmiester, J. Rebizant, J. C. Spirlet, and O. Vogt, 1987, *Solid State Commun.* **64**, 193.

- Kalkowski, G., G. Kaindl, W. D. Brewer, and W. Krone, 1987, *Phys. Rev. B* **35**, 2667.
- Kawamura, N., Y. Hirose, F. Honda, R. Shimokasa, N. Ishimatsu, M. Mizumaki, S. I. Kawaguchi, N. Hirao, and K. Mimura, 2020, *JPS Conf. Proc.* **30**, 011172.
- Kernavainis, N., P. Dalmas de Réotier, A. Yaouanc, J.-P. Sanchez, V. Honkimäki, T. Tschentscher, J. McCarthy, and O. Vogt, 2001, *J. Phys. Condens. Matter* **13**, 9677.
- Kernavainis, N., B. Grenier, A. Huxley, E. Ressouche, J. P. Sanchez, and J. Flouquet, 2001, *Phys. Rev. B* **64**, 174509.
- Klimczuk, T., A. B. Shick, R. Springell, H. C. Walker, A. H. Hill, E. Colineau, J.-C. Griveau, D. Bouëxière, R. Eloirdi, and R. Caciuffo, 2012, *Phys. Rev. B* **86**, 174510.
- Klimczuk, T., *et al.*, 2012, *Phys. Rev. B* **85**, 174506.
- Knol, S., S. de Groot, P. R. Hania, and M. H. C. Hannink, 2012, *Nucl. Eng. Des.* **251**, 150.
- Kokubun, J., and V. E. Dmitrienko, 2012, *Eur. Phys. J. Special Topics* **208**, 39.
- Kolomiets, A. V., *et al.*, 2021, *Phys. Rev. B* **104**, 045119.
- Kolorenc, J., A. B. Shick, and R. Caciuffo, 2012, *Mater. Res. Soc. Symp. Proc.* **1444**, 177.
- Konishi, H., *et al.*, 1996, *Nucl. Instrum. Methods Phys. Res., Sect. A* **372**, 322.
- Kotani, A., and S. Shin, 2001, *Rev. Mod. Phys.* **73**, 203.
- Kotliar, G., S. Y. Savrasov, K. Haule, V. S. Oudovenko, O. Parcollet, and C. A. Marianetti, 2006, *Rev. Mod. Phys.* **78**, 865.
- Kramers, H. A., and W. Heisenberg, 1925, *Z. Phys.* **31**, 681.
- Krisch, M., and F. Sette, 2007, in *Light Scattering in Solids, Novel Materials and Techniques*, Topics in Applied Physics Vol. 108, edited by M. Cardona and R. Merlin (Springer-Verlag, Berlin), pp. 317–369.
- Kučera, M., J. Kuneš, A. Kolomiets, M. Diviš, A. V. Andreev, V. Sechovský, J.-P. Kappler, and A. Rogalev, 2002, *Phys. Rev. B* **66**, 144405.
- Kumigashira, H., T. Ito, A. Ashihara, H.-D. Kim, H. Aoki, T. Suzuki, H. Yamagami, T. Takahashi, and A. Ochiai, 2000, *Phys. Rev. B* **61**, 15707.
- Kuzushita, K., *et al.*, 2006, *Phys. Rev. B* **73**, 104431.
- Kvashnina, K. O., and S. M. Butorin, 2022, *Chem. Commun. (Cambridge)* **58**, 327.
- Kvashnina, K. O., S. M. Butorin, P. Martin, and P. Glatzel, 2013, *Phys. Rev. Lett.* **111**, 253002.
- Kvashnina, K. O., S. M. Butorin, D. K. Shuh, J.-H. Guo, L. Werme, and J. Nordgren, 2007, *Phys. Rev. B* **75**, 115107.
- Kvashnina, K. O., Y. O. Kvashnin, and S. M. Butorin, 2014, *J. Electron Spectrosc. Relat. Phenom.* **194**, 27.
- Kvashnina, K. O., and A. C. Scheinost, 2016, *J. Synchrotron Radiat.* **23**, 836.
- Kvashnina, K. O., H. C. Walker, N. Magnani, G. H. Lander, and R. Caciuffo, 2017, *Phys. Rev. B* **95**, 245103.
- Kvashnina, K. O., *et al.*, 2019, *Angew. Chem., Int. Ed. Engl.* **58**, 17558.
- Lander, G., E. Fisher, and S. Bader, 1994, *Adv. Phys.* **43**, 1.
- Lander, G. H., 1993, in *Handbook of Physics and Chemistry of Rare Earths*, Vol. 17, edited by K. A. Gschneidner, L. Eyring, G. H. Lander, and G. R. Choppin (North-Holland, Amsterdam), Chap. 17, p. 635.
- Lander, G. H., A. T. Aldred, B. D. Dunlap, and G. K. Shenoy, 1977, *Physica (Amsterdam)* **86B+C–88B+C**, 152.
- Lander, G. H., M. S. S. Brooks, and B. Johansson, 1991, *Phys. Rev. B* **43**, 13672.
- Lander, G. H., and R. Caciuffo, 2021, [arXiv:2104.06340](https://arxiv.org/abs/2104.06340).
- Lander, G. H., M. Sundermann, R. Springell, A. C. Walters, A. Nag, M. Garcia-Fernandez, K. J. Zhou, G. van der Laan, and R. Caciuffo, 2021, *J. Phys. Condens. Matter* **33**, 06LT01.
- Lander, G. H., *et al.*, 2019, *Phys. Rev. B* **99**, 224419.
- Langridge, S., W. G. Stirling, G. H. Lander, and J. Rebizant, 1994a, *Phys. Rev. B* **49**, 12010.
- Langridge, S., W. G. Stirling, G. H. Lander, and J. Rebizant, 1994b, *Phys. Rev. B* **49**, 12022.
- Langridge, S., G. M. Watson, D. Gibbs, J. J. Betouras, N. I. Gidopoulos, F. Pollmann, M. W. Long, C. Vettier, and G. H. Lander, 2014, *Phys. Rev. Lett.* **112**, 167201.
- Langridge, S., *et al.*, 1997, *Phys. Rev. B* **55**, 6392.
- Larson, B. C., W. Ku, J. Z. Tischler, C.-C. Lee, O. D. Restrepo, A. G. Eguliz, P. Zschack, and K. D. Finkelstein, 2007, *Phys. Rev. Lett.* **99**, 026401.
- Lashley, J. C., and A. Lawson, 2019, in *Plutonium Handbook*, edited by D. L. Clark, D. A. Geeson, and R. J. Hanrahan (American Nuclear Society, Oak Brook, IL), Chap. 7, p. 287.
- Lashley, J. C., A. Lawson, R. J. McQueeney, and G. H. Lander, 2005, *Phys. Rev. B* **72**, 054416.
- Lawrence Bright, E., R. Springell, D. G. Porter, S. P. Collins, and G. H. Lander, 2019, *Phys. Rev. B* **100**, 134426.
- Lawrence Bright, E., *et al.*, 2023, *J. Phys. Condens. Matter* (in press), [10.1088/1361-648X/acb8f4](https://doi.org/10.1088/1361-648X/acb8f4).
- Le Bihan, T., S. Heathman, M. Idiri, G. H. Lander, J. M. Wills, A. C. Lawson, and A. Lindbaum, 2003, *Phys. Rev. B* **67**, 134102.
- Leinders, G., R. Bes, K. O. Kvashnina, and M. Verwerft, 2020, *Inorg. Chem.* **59**, 4576.
- Le Pape, P., L. Stetten, M. O. J. Y. Hunault, A. Mangeret, J. Brest, J.-C. Boulliard, and G. Morin, 2020, *Appl. Geochem.* **122**, 104714.
- Lidström, E., D. Mannix, A. Hiess, J. Rebizant, F. Wastin, G. H. Lander, I. Marri, P. Carra, C. Vettier, and M. J. Longfield, 2000, *Phys. Rev. B* **61**, 1375.
- Liermann, H. P., *et al.*, 2021, *J. Synchrotron Radiat.* **28**, 688.
- Liermann, H.-P., *et al.*, 2015, *J. Synchrotron Radiat.* **22**, 908.
- Lim, J. A., E. Blackburn, G. Beutier, F. Livet, N. Magnani, A. Bombardi, R. Caciuffo, and G. H. Lander, 2014, *J. Phys. Conf. Ser.* **519**, 012010.
- Lim, J. A., E. Blackburn, N. Magnani, A. Hiess, L. P. Regnault, R. Caciuffo, and G. H. Lander, 2013, *Phys. Rev. B* **87**, 064421.
- Lindbaum, A., S. Heathman, K. Litfin, Y. Méresse, R. G. Haire, T. Le Bihan, and H. Libotte, 2001, *Phys. Rev. B* **63**, 214101.
- Liu, D., S. Knol, J. Ell, H. Barnard, M. Davies, J. A. Vreeling, and R. O. Ritchie, 2020, *Mater. Des.* **187**, 108382.
- Liu, L., N. Milas, A. H. C. Mukai, X. R. Resende, and F. H. de Sá, 2014, *J. Synchrotron Radiat.* **21**, 904.
- Longfield, M. J., J. A. Paixão, N. Bernhoeft, and G. H. Lander, 2002, *Phys. Rev. B* **66**, 054417.
- Lytle, F. W., 1999, *J. Synchrotron Radiat.* **6**, 123.
- Macrander, A. T., P. A. Montano, D. L. Price, V. I. Kushnir, R. C. Blasdel, C. C. Kao, and B. R. Cooper, 1996, *Phys. Rev. B* **54**, 305.
- Magnani, N., R. Caciuffo, F. Wilhelm, E. Colineau, R. Eloirdi, J.-C. Griveau, J. Ruzs, P. M. Oppeneer, A. Rogalev, and G. H. Lander, 2015, *Phys. Rev. Lett.* **114**, 097203.
- Magnani, N., S. Carretta, R. Caciuffo, P. Santini, G. Amoretti, A. Hiess, J. Rebizant, and G. H. Lander, 2008, *Phys. Rev. B* **78**, 104425.
- Magnani, N., R. Eloirdi, F. Wilhelm, E. Colineau, J.-C. Griveau, A. B. Shick, G. H. Lander, A. Rogalev, and R. Caciuffo, 2017, *Phys. Rev. Lett.* **119**, 157204.

- Magnani, N., P. Santini, G. Amoretti, and R. Caciuffo, 2005, *Phys. Rev. B* **71**, 054405.
- Maldonado, P., L. Paolasini, P. M. Oppeneer, T. R. Forrest, A. Prodi, N. Magnani, A. Bosak, G. H. Lander, and R. Caciuffo, 2016, *Phys. Rev. B* **93**, 144301.
- Manley, M. E., B. Fultz, R. J. McQueeney, C. M. Brown, W. L. Hulst, J. L. Smith, D. J. Thoma, R. Osborn, and J. L. Robertson, 2001, *Phys. Rev. Lett.* **86**, 3076.
- Manley, M. E., J. R. Jeffries, A. H. Said, C. A. Marianetti, H. Cynn, B. M. Leu, and M. A. Wall, 2012, *Phys. Rev. B* **85**, 132301.
- Manley, M. E., G. H. Lander, H. Sinn, A. Alatas, W. L. Hulst, R. J. McQueeney, J. L. Smith, and J. Willit, 2003, *Phys. Rev. B* **67**, 052302.
- Manley, M. E., J. W. Lynn, Y. Chen, and G. H. Lander, 2008, *Phys. Rev. B* **77**, 052301.
- Manley, M. E., A. H. Said, M. J. Fluss, M. Wall, J. C. Lashley, A. Alatas, K. T. Moore, and Y. Shvyd'ko, 2009, *Phys. Rev. B* **79**, 052301.
- Manley, M. E., M. Yethiraj, H. Sinn, H. M. Volz, A. Alatas, J. C. Lashley, W. L. Hulst, G. H. Lander, and J. L. Smith, 2006, *Phys. Rev. Lett.* **96**, 125501.
- Mannix, D., G. H. Lander, J. Rebizant, R. Caciuffo, N. Bernhoeft, E. Lidström, and C. Vettier, 1999, *Phys. Rev. B* **60**, 15187.
- Mannix, D., S. Langridge, G. H. Lander, J. Rebizant, M. J. Longfield, W. G. Stirling, W. J. Nuttall, S. Couburn, S. Wasserman, and L. Soderholm, 1999, *Physica (Amsterdam)* **262B**, 125.
- Mannix, D., A. Stunault, N. Bernhoeft, L. Paolasini, G. H. Lander, C. Vettier, F. de Bergevin, D. Kaczorowski, and A. Czopnik, 2001, *Phys. Rev. Lett.* **86**, 4128.
- Mason, T. E., B. D. Gaulin, J. D. Garrett, Z. Tun, W. J. L. Buyers, and E. D. Isaacs, 1990, *Phys. Rev. Lett.* **65**, 3189.
- McMahon, M. I., 2014, *J. Synchrotron Radiat.* **21**, 1077.
- McMahon, M. I., 2022, *J. Phys. Condens. Matter* **34**, 043001.
- McMorrow, D. F., K. A. McEwen, U. Steigenberger, H. M. Rønnow, and F. Yakhov, 2001, *Phys. Rev. Lett.* **87**, 057201.
- Meng, Y., R. Hrubiak, E. Rod, R. Boehler, and G. Shen, 2015, *Rev. Sci. Instrum.* **86**, 072201.
- Mezouar, M., *et al.*, 2005, *J. Synchrotron Radiat.* **12**, 659.
- Micheau, C., M. Virost, S. Dourdain, T. Dumas, D. Menut, P. L. Solari, L. Venault, O. Diat, P. Moisy, and S. I. Nikitenko, 2020, *Environ. Sci. Nano* **7**, 2252.
- Minasian, S. G., *et al.*, 2012, *J. Am. Chem. Soc.* **134**, 5586.
- Miyake, S., and S. Watanabe, 2014, *J. Phys. Soc. Jpn.* **83**, 061006.
- Modin, A., Y. Yun, M.-T. Suzuki, J. Vegelius, L. Werme, J. Nordgren, P. M. Oppeneer, and S. M. Butorin, 2011, *Phys. Rev. B* **83**, 075113.
- Moeyaert, P., T. Dumas, D. Guillaumont, P. L. Solari, C. Lefebvre, A. Thevenet, C. Sorel, and P. Moisy, 2021, *Solvent Extr. Ion Exch.* **39**, 305.
- Moore, K. T., and G. van der Laan, 2009, *Rev. Mod. Phys.* **81**, 235.
- Moore, K. T., G. van der Laan, R. G. Haire, M. A. Wall, and A. J. Schwartz, 2006, *Phys. Rev. B* **73**, 033109.
- Moore, K. T., G. van der Laan, R. G. Haire, M. A. Wall, A. J. Schwartz, and P. Söderlind, 2007, *Phys. Rev. Lett.* **98**, 236402.
- Murphy, G. L., P. Kegler, Y. Zhang, Z. Zhang, E. V. Alekseev, M. D. de Jonge, and B. J. Kennedy, 2018, *Inorg. Chem.* **57**, 13847.
- Mydosh, J. A., and P. M. Oppeneer, 2011, *Rev. Mod. Phys.* **83**, 1301.
- Mydosh, J. A., P. M. Oppeneer, and P. S. Riseborough, 2020, *J. Phys. Condens. Matter* **32**, 143002.
- Naegele, J. R., L. Manes, J. C. Spirlet, and W. Müller, 1984, *Phys. Rev. Lett.* **52**, 1834.
- Nagao, T., and J.-i. Igarashi, 2005, *Phys. Rev. B* **72**, 174421.
- Nastren, C., R. Jardin, J. Somers, M. Walter, and B. Brendebach, 2009, *J. Solid State Chem.* **182**, 1.
- Nilsson, F., and F. Aryasetiawan, 2018, *Computation* **6**, 26.
- Normile, P. S., W. G. Stirling, D. Mannix, G. H. Lander, F. Wastin, J. Rebizant, F. Boudarot, P. Burlet, B. Lebech, and S. Couburn, 2002a, *Phys. Rev. B* **66**, 014405.
- Normile, P. S., W. G. Stirling, D. Mannix, G. H. Lander, F. Wastin, J. Rebizant, and S. Couburn, 2002b, *Phys. Rev. B* **66**, 014406.
- Nyman, M., 2017, *Coord. Chem. Rev.* **352**, 461.
- Ohkochi, T., S.-i. Fujimori, H. Yamagami, T. Okane, Y. Saitoh, A. Fujimori, Y. Haga, E. Yamamoto, and Y. Ōnuki, 2008, *Phys. Rev. B* **78**, 165110.
- Okane, T., J. Okamoto, K. Mamiya, S.-I. Fujimori, Y. Saitoh, Y. Muramatsu, A. Fujimori, and A. Ochiai, 2004, *Physica (Amsterdam)* **345B**, 221.
- Okane, T., *et al.*, 2006a, *J. Phys. Soc. Jpn.* **75**, 024704.
- Okane, T., *et al.*, 2006b, *J. Phys. Soc. Jpn.* **75**, 105.
- Okane, T., *et al.*, 2008, *J. Phys. Soc. Jpn.* **77**, 024706.
- Oppeneer, P. M., S. Elgazzar, J. Rusz, Q. Feng, T. Durakiewicz, and J. A. Mydosh, 2011, *Phys. Rev. B* **84**, 241102.
- Paixão, J. A., C. Detlefs, M. J. Longfield, R. Caciuffo, P. Santini, N. Bernhoeft, J. Rebizant, and G. H. Lander, 2002, *Phys. Rev. Lett.* **89**, 187202.
- Palomares, R. I., *et al.*, 2019, *Phys. Rev. Mater.* **3**, 053611.
- Paolasini, L., D. Chaney, A. Bosak, G. H. Lander, and R. Caciuffo, 2021, *Phys. Rev. B* **104**, 024305.
- Parratt, L. G., and C. F. Hempstead, 1954, *Phys. Rev.* **94**, 1593.
- Pezzoli, M. E., K. Haule, and G. Kotliar, 2011, *Phys. Rev. Lett.* **106**, 016403.
- Pfalzer, P., J.-P. Urbach, M. Klemm, S. Horn, M. L. denBoer, A. I. Frenkel, and J. P. Kirkland, 1999, *Phys. Rev. B* **60**, 9335.
- Pidchenko, I., J. März, M. O. J. Y. Hunault, S. Bauters, S. M. Butorin, and K. O. Kvashnina, 2020, *Inorg. Chem.* **59**, 11889.
- Plakhova, T. V., *et al.*, 2019, *J. Phys. Chem. C* **123**, 23167.
- Pourovskii, L. V., and S. Khmelevskiy, 2021, *Proc. Natl. Acad. Sci. U.S.A.* **118**, e2025317118.
- Prieur, D., P. Martin, F. Lebreton, T. Delahaye, D. Banerjee, A. C. Scheinost, and A. Jankowiak, 2013, *J. Nucl. Mater.* **434**, 7.
- Prokeš, K., G. H. Lander, and N. Bernhoeft, 2009, *J. Phys. Condens. Matter* **21**, 285402.
- Pruessmann, T., P. Nagel, L. Simonelli, D. Batchelor, R. Gordon, B. Schimmelpfennig, M. Trumm, and T. Vitova, 2022, *J. Synchrotron Radiat.* **29**, 53.
- Qiao, Y., *et al.*, 2021, *Chem. Commun. (Cambridge)* **57**, 9562.
- Raboud, P.-A., J.-C. Dousse, J. Hozzowska, and I. Savoy, 1999, *Phys. Rev. A* **61**, 012507.
- Raimondi, P., 2016, *Synchrotron Radiat. News* **29**, 8.
- Ramshaw, B. J., A. Shekhter, R. D. McDonald, J. B. Betts, J. N. Mitchell, P. H. Tobash, C. H. Mielke, E. D. Bauer, and A. Migliori, 2015, *Proc. Natl. Acad. Sci. U.S.A.* **112**, 3285.
- Ran, S., *et al.*, 2019, *Science* **365**, 684.
- Raymond, S., *et al.*, 2006, *Phys. Rev. Lett.* **96**, 237003.
- Raymond, S., *et al.*, 2011, *Phys. Rev. Lett.* **107**, 136401.
- Rehr, J. J., J. M. de Leon, S. I. Zabinsky, and R. C. Albers, 1991, *J. Am. Chem. Soc.* **113**, 5135.
- Reinart, F., and S. Hufner, 2005, *New J. Phys.* **7**, 97.
- Rennie, S., E. Lawrence Bright, J. E. Darnbrough, L. Paolasini, A. Bosak, A. D. Smith, N. Mason, G. H. Lander, and R. Springell, 2018, *Phys. Rev. B* **97**, 224303.
- Rennie, S., E. Lawrence Bright, J. E. Sutcliffe, J. E. Darnbrough, R. Burrows, J. Rawle, C. Nicklin, G. H. Lander, and R. Springell, 2018, *Corros. Sci.* **145**, 162.
- Ressouche, E., R. Ballou, F. Bourdarot, D. Aoki, V. Simonet, M. T. Fernandez-Diaz, A. Stunault, and J. Flouquet, 2012, *Phys. Rev. Lett.* **109**, 067202.

- Richmann, M. K., D. T. Reed, A. J. Kropf, S. B. Aase, and M. A. Lewis, 2001, *J. Nucl. Mater.* **297**, 303.
- Rittman, D. R., S. Park, C. L. Tracy, L. Zhang, R. I. Palomares, M. Lang, A. Navrotsky, W. L. Mao, and R. C. Ewing, 2017, *J. Nucl. Mater.* **490**, 28.
- Rogalev, A., and F. Wilhelm, 2015, *Phys. Met. Metallogr.* **116**, 1285.
- Romanchuk, A., A. Trigub, T. Plakhova, A. Kuzenkova, R. Svetogorov, K. Kvashnina, and S. Kalmykov, 2022, *J. Synchrotron Radiat.* **29**, 288.
- Rotenberg, E., and A. Bostwick, 2014, *J. Synchrotron Radiat.* **21**, 1048.
- Rothe, J., *et al.*, 2012, *Rev. Sci. Instrum.* **83**, 043105.
- Rothe, J. J., C. Walther, M. A. Denecke, and T. Fanghänel, 2004, *Inorg. Chem.* **43**, 4708.
- Rueff, J.-P., S. Raymond, A. Yaresko, D. Braithwaite, P. Leininger, G. Vankó, A. Huxley, J. Rebizant, and N. Sato, 2007, *Phys. Rev. B* **76**, 085113.
- Rueff, J.-P., and A. Shukla, 2010, *Rev. Mod. Phys.* **82**, 847.
- Saitoh, E., S. Okamoto, K. Takahashi, K. Tobe, K. Yamamoto, T. Kimura, S. Ishihara, S. Maekawa, and Y. Tokura, 2001, *Nature (London)* **410**, 180.
- Saitoh, Y., T. Nakatani, T. Matsushita, A. Agui, A. Yoshigoe, Y. Teraoka, and A. Yokoya, 2001, *Nucl. Instrum. Methods Phys. Res., Sect. A* **474**, 253.
- Saitoh, Y., *et al.*, 2012, *J. Synchrotron Radiat.* **19**, 388.
- Sakurai, J. J., 1967, *Advanced Quantum Mechanics* (Addison-Wesley, Reading, MA).
- Sanchez, J. P., P. Vulliet, M. M. Abd-Elmeguid, and D. Kaczorowski, 2000, *Phys. Rev. B* **62**, 3839.
- Santini, P., and G. Amoretti, 1994, *Phys. Rev. Lett.* **73**, 1027.
- Santini, P., G. Amoretti, R. Caciuffo, F. Bourdarot, and B. Fåk, 2000, *Phys. Rev. Lett.* **85**, 654.
- Santini, P., S. Carretta, G. Amoretti, R. Caciuffo, N. Magnani, and G. H. Lander, 2009, *Rev. Mod. Phys.* **81**, 807.
- Santini, P., S. Carretta, N. Magnani, G. Amoretti, and R. Caciuffo, 2006, *Phys. Rev. Lett.* **97**, 207203.
- Sarrao, J. L., L. A. Morales, J. D. Thompson, B. L. Scott, G. R. Stewart, F. Wastin, J. Rebizant, P. Boulet, E. Colineau, and G. H. Lander, 2002, *Nature (London)* **420**, 297.
- Savrasov, S. Y., K. Haule, and G. Kotliar, 2006, *Phys. Rev. Lett.* **96**, 036404.
- Schacherl, B., T. Prüssmann, K. Dardenne, K. Hardock, V. Krepper, J. Rothe, T. Vitova, and H. Geckeis, 2022, *J. Synchrotron Radiat.* **29**, 80.
- Schacherl, B., *et al.*, 2022, *Anal. Chim. Acta* **1202**, 339636.
- Scheinost, A. C., *et al.*, 2021, *J. Synchrotron Radiat.* **28**, 333.
- Schmitt, T., F. De Groot, and J. Rubensson, 2014, *J. Synchrotron Radiat.* **21**, 1065.
- Schülke, W., 2007, *Electron Dynamics by Inelastic X-Ray Scattering* (Oxford University Press, Oxford).
- Sen Gupta, S., J. A. Bradley, M. W. Haverkort, G. T. Seidler, A. Tanaka, and G. A. Sawatzky, 2011, *Phys. Rev. B* **84**, 075134.
- Sergentou, D.-C., and J. Autschbach, 2022, *Chem. Sci.* **13**, 3194.
- Shen, G., V. B. Prakapenka, P. J. Eng, M. L. Rivers, and S. R. Sutton, 2005, *J. Synchrotron Radiat.* **12**, 642.
- Shi, W.-Q., L.-Y. Yuan, C.-Z. Wang, L. Wang, L. Mei, C.-L. Xiao, L. Zhang, Z.-J. Li, Y.-L. Zhao, and Z.-F. Chai, 2014, *Adv. Mater.* **26**, 7807.
- Shick, A. B., S.-i. Fujimori, and W. E. Pickett, 2021, *Phys. Rev. B* **103**, 125136.
- Shick, A. B., V. Janiš, V. Drchal, and W. E. Pickett, 2004, *Phys. Rev. B* **70**, 134506.
- Shick, A. B., J. Kolorenc, J. Ruzs, P. M. Oppeneer, A. I. Lichtenstein, M. I. Katsnelson, and R. Caciuffo, 2013, *Phys. Rev. B* **87**, 020505.
- Shim, J., K. Haule, and G. Kotliar, 2007, *Nature (London)* **446**, 513.
- Shim, J. H., K. Haule, and G. Kotliar, 2009, *Europhys. Lett.* **85**, 17007.
- Shpyrko, O. G., 2014, *J. Synchrotron Radiat.* **21**, 1057.
- Shukla, B., N. R. Sanjay Kumar, S. Chandra, N. V. Chandra Shekar, A. K. Sinha, A. Upadhyay, and M. N. Singh, 2017, *Intermetallics* **83**, 110.
- Silva, R. J., and H. Nitsche, 1995, *Radiochim. Acta* **70–71**, 377.
- Skanthakumar, S., M. R. Antonio, R. E. Wilson, and L. Soderholm, 2007, *Inorg. Chem.* **46**, 3485.
- Skinner, L. B., *et al.*, 2014, *Science* **346**, 984.
- Smith, A. L., *et al.*, 2019, *J. Synchrotron Radiat.* **26**, 124.
- Solari, P. L., S. Schlutig, H. Hermange, and B. Sitaud, 2009, *J. Phys. Conf. Ser.* **190**, 012042.
- Springell, R., R. C. C. Ward, J. Bouchet, J. Chivall, D. Wermeille, P. S. Normile, S. Langridge, S. W. Zochowski, and G. H. Lander, 2014, *Phys. Rev. B* **89**, 245101.
- Springell, R., F. Wilhelm, A. Rogalev, W. G. Stirling, R. C. C. Ward, M. R. Wells, S. Langridge, S. W. Zochowski, and G. H. Lander, 2008, *Phys. Rev. B* **77**, 064423.
- Springell, R., *et al.*, 2015, *Faraday Discuss.* **180**, 301.
- Staub Olsen, J., L. Gerward, U. Benedict, S. Dabos, and O. Vogt, 1988, *Phys. Rev. B* **37**, 8713.
- Stöhr, J., 1992, *NEXAFS Spectroscopy* (Springer-Verlag, Heidelberg).
- Stöhr, J., and H. König, 1995, *Phys. Rev. Lett.* **75**, 3748.
- Stubbs, J. E., C. A. Biwer, A. M. Chaka, E. S. Ilton, Y. Du, J. R. Bargar, and P. J. Eng, 2017, *Langmuir* **33**, 13189.
- Stubbs, J. E., A. M. Chaka, E. S. Ilton, C. A. Biwer, M. H. Engelhard, J. R. Bargar, and P. J. Eng, 2015, *Phys. Rev. Lett.* **114**, 246103.
- Sundermann, M., L. Simonelli, S. Huotari, R. Eloirdi, G. H. Lander, R. Caciuffo, and G. van der Laan, 2020, *Phys. Rev. B* **101**, 075103.
- Sundermann, M., G. van der Laan, A. Severing, L. Simonelli, G. H. Lander, M. W. Haverkort, and R. Caciuffo, 2018, *Phys. Rev. B* **98**, 205108.
- Sundermann, M., *et al.*, 2016, *Proc. Natl. Acad. Sci. U.S.A.* **113**, 13989.
- Suzuki, M.-T., N. Magnani, and P. M. Oppeneer, 2010, *Phys. Rev. B* **82**, 241103.
- Takeda, Y., T. Okane, Y. Saitoh, H. Yamagami, E. Yamamoto, and Y. Haga, 2018, *Prog. Nucl. Sci. Technol.* **5**, 171.
- Taupin, M., J.-P. Sanchez, J.-P. Brison, D. Aoki, G. Lapertot, F. Wilhelm, and A. Rogalev, 2015, *Phys. Rev. B* **92**, 035124.
- Tavares, P. F., *et al.*, 2018, *J. Synchrotron Radiat.* **25**, 1291.
- Templeton, D. H., and L. K. Templeton, 1980, *Acta Crystallogr. A* **36**, 237.
- Templeton, D. H., and L. K. Templeton, 1994, *Phys. Rev. B* **49**, 14850.
- Terry, J., R. K. Schulze, J. D. Farr, T. Zocco, K. Heinzelman, E. Rotenberg, D. K. Shuh, G. van der Laan, D. A. Arena, and J. G. Tobin, 2002, *Surf. Sci.* **499**, L141.
- Thibault, P., M. Guizar-Sicairos, and A. Menzel, 2014, *J. Synchrotron Radiat.* **21**, 1011.
- Thole, B. T., P. Carra, F. Sette, and G. van der Laan, 1992, *Phys. Rev. Lett.* **68**, 1943.
- Thole, B. T., and G. van der Laan, 1988, *Phys. Rev. B* **38**, 3158.
- Thole, B. T., G. van der Laan, J. C. Fuggle, G. A. Sawatzky, R. C. Karnatak, and J. M. Esteva, 1985, *Phys. Rev. B* **32**, 5107.
- Thomas, J., A. Figueroa Bengoa, S. Tapaswi Nori, R. Ren, P. Kenesei, J. Almer, J. Hunter, J. Harp, and M. A. Okuniewski, 2020, *J. Nucl. Mater.* **537**, 152161.

- Tian, Q., D. Zhang, N. Li, M. J. Henderson, Q. Li, G. Royal, J. Courtois, M. Yan, Z. Zhu, and L. Almásy, 2020, *Langmuir* **36**, 4820.
- Tobin, J. G., B. W. Chung, R. K. Schulze, J. Terry, J. D. Farr, D. K. Shuh, K. Heinzelman, E. Rotenberg, G. D. Waddill, and G. van der Laan, 2003, *Phys. Rev. B* **68**, 155109.
- Tobin, J. G., K. T. Moore, B. W. Chung, M. A. Wall, A. J. Schwartz, G. van der Laan, and A. L. Kutepov, 2005, *Phys. Rev. B* **72**, 085109.
- Tobin, J. G., S. Nowak, C. H. Booth, E. D. Bauer, S.-W. Yu, R. Alonso-Mori, T. Kroll, D. Nordlund, T.-C. Weng, and D. Sokaras, 2019, *J. Electron Spectrosc. Relat. Phenom.* **232**, 100.
- Tobin, J. G., S. Nowak, S. W. Yu, R. Alonso-Mori, T. Kroll, D. Nordlund, T. C. Weng, and D. Sokaras, 2021, *Appl. Sci.* **11**, 3882.
- Tobin, J. G., P. Söderlind, A. Landa, K. T. Moore, A. J. Schwartz, B. W. Chung, M. A. Wall, J. M. Wills, R. G. Haire, and A. L. Kutepov, 2008, *J. Phys. Condens. Matter* **20**, 125204.
- Tobin, J. G., S.-W. Yu, C. H. Booth, T. Tyliczszak, D. K. Shuh, G. van der Laan, D. Sokaras, D. Nordlund, T.-C. Weng, and P. S. Bagus, 2015, *Phys. Rev. B* **92**, 035111.
- Tobin, J. G., S.-W. Yu, R. Qiao, W. L. Yang, C. H. Booth, D. K. Shuh, A. M. Duffin, D. Sokaras, D. Nordlund, and T.-C. Weng, 2015, *Phys. Rev. B* **92**, 045130.
- Tröger, L., D. Arvanitis, K. Baberschke, H. Michaelis, U. Grimm, and E. Zschech, 1992, *Phys. Rev. B* **46**, 3283.
- Usuda, M., J.-i. Igarashi, and A. Kodama, 2004, *Phys. Rev. B* **69**, 224402.
- van der Laan, G., 1998a, *Phys. Rev. B* **57**, 5250.
- van der Laan, G., 1998b, *Phys. Rev. B* **57**, 112.
- van der Laan, G., 1999, *Phys. Rev. Lett.* **82**, 640.
- van der Laan, G., 2006, *Lect. Notes Phys.* **697**, 201.
- van der Laan, G., 2008, *C.R. Phys.* **9**, 570.
- van der Laan, G., 2012a, *Phys. Rev. B* **86**, 035138.
- van der Laan, G., 2012b, *Phys. Rev. Lett.* **108**, 077401.
- van der Laan, G., 2013, *J. Phys. Conf. Ser.* **430**, 012127.
- van der Laan, G., and A. Figueroa, 2014, *Coord. Chem. Rev.* **277–278**, 95.
- van der Laan, G., and S. W. Lovesey, 2021, *Phys. Rev. B* **103**, 125124.
- van der Laan, G., K. T. Moore, J. G. Tobin, B. W. Chung, M. A. Wall, and A. J. Schwartz, 2004, *Phys. Rev. Lett.* **93**, 097401.
- van der Laan, G., and M. Taguchi, 2010, *Phys. Rev. B* **82**, 045114.
- van der Laan, G., and B. T. Thole, 1996, *Phys. Rev. B* **53**, 14458.
- van der Laan, G., C. Westra, C. Haas, and G. A. Sawatzky, 1981, *Phys. Rev. B* **23**, 4369.
- van der Laan, G., J. Zaanen, G. A. Sawatzky, R. C. Karnatak, and J. M. Esteva, 1986, *Phys. Rev. B* **33**, 4253.
- van der Laan, G., *et al.*, 1999, *Phys. Rev. B* **59**, 8835.
- Van Hove, L., 1954, *Phys. Rev.* **95**, 249.
- van Veelen, A., S. M. Hickam, N. P. Edwards, S. M. Webb, D. L. Clark, M. P. Wilkerson, A. L. Pugmire, and J. R. Bargar, 2022, *Anal. Chem.* **94**, 7084.
- van Veenendaal, M., 2003, *Phys. Rev. B* **67**, 134112.
- van Veenendaal, M., P. Carra, and B. T. Thole, 1996, *Phys. Rev. B* **54**, 16010.
- van Veenendaal, M., and M. W. Haverkort, 2008, *Phys. Rev. B* **77**, 224107.
- Veal, B. W., and D. J. Lam, 1974, *Phys. Rev. B* **10**, 4902.
- Verbeni, R., T. Pylkkänen, S. Huotari, L. Simonelli, G. Vankó, K. Martel, C. Henriquet, and G. Monaco, 2009, *J. Synchrotron Radiat.* **16**, 469.
- Vitova, T., M. A. Denecke, J. Göttlicher, K. Jorissen, J. J. Kas, K. O. Kvashnina, T. Prüssmann, J. J. Rehr, and J. Rothe, 2013, *J. Phys. Conf. Ser.* **430**, 012117.
- Vitova, T., *et al.*, 2010, *Phys. Rev. B* **82**, 235118.
- Vitova, T., *et al.*, 2018, *Chem. Commun. (Cambridge)* **54**, 12824.
- Vitova, T., *et al.*, 2020, *Inorg. Chem.* **59**, 8.
- Volkovich, V., I. May, T. Griffiths, J. Charnock, A. Bhatt, and B. Lewin, 2005, *J. Nucl. Mater.* **344**, 100.
- von Löhnneysen, H., A. Rosch, M. Vojta, and P. Wölfle, 2007, *Rev. Mod. Phys.* **79**, 1015.
- Walker, H. C., R. Caciuffo, D. Aoki, F. Bourdarot, G. H. Lander, and J. Flouquet, 2011, *Phys. Rev. B* **83**, 193102.
- Walker, H. C., M. D. Le, K. A. McEwen, M. Bleckmann, S. Süllow, C. Mazzoli, S. B. Wilkins, and D. Fort, 2011, *Phys. Rev. B* **84**, 235142.
- Walker, H. C., K. A. McEwen, M. D. Le, L. Paolasini, and D. Fort, 2008, *J. Phys. Condens. Matter* **20**, 395221.
- Walker, H. C., K. A. McEwen, D. F. McMorro, S. B. Wilkins, F. Wastin, E. Colineau, and D. Fort, 2006, *Phys. Rev. Lett.* **97**, 137203.
- Walker, M. B., W. J. L. Buyers, Z. Tun, W. Que, A. A. Menovsky, and J. D. Garrett, 1993, *Phys. Rev. Lett.* **71**, 2630.
- Walshe, A., T. Prüssmann, T. Vitova, and R. J. Baker, 2014, *Dalton Trans.* **43**, 4400.
- Walter, M., J. Somers, A. Fernandez-Carretero, and J. Rothe, 2008, *J. Nucl. Mater.* **373**, 90.
- Walters, A. C., *et al.*, 2015, *J. Phys. Condens. Matter* **27**, 325702.
- Wang, J., R. C. Ewing, and U. Becker, 2014, *Sci. Rep.* **4**, 4216.
- Wang, Y. L., *et al.*, 2017, *Phys. Rev. B* **96**, 085146.
- Watson, G. M., D. Gibbs, G. H. Lander, B. D. Gaulin, L. E. Berman, H. Matzke, and W. Ellis, 1996, *Phys. Rev. Lett.* **77**, 751.
- Watson, G. M., D. Gibbs, G. H. Lander, B. D. Gaulin, L. E. Berman, H. Matzke, and W. Ellis, 2000, *Phys. Rev. B* **61**, 8966.
- Wermeille, D., C. Vettier, N. Bernhoeft, A. Stunault, S. Langridge, F. de Bergevin, F. Yakhov, E. Lidström, J. Flouquet, and P. Lejay, 1998, *Phys. Rev. B* **58**, 9185.
- Wilhelm, F., R. Eloirdi, J. Ruzs, R. Springell, E. Colineau, J.-C. Griveau, P. M. Oppeneer, R. Caciuffo, A. Rogalev, and G. H. Lander, 2013, *Phys. Rev. B* **88**, 024424.
- Wilhelm, F., J.-P. Sanchez, and A. Rogalev, 2018, *J. Phys. D* **51**, 333001.
- Wilhelm, F., *et al.*, 2007, *Phys. Rev. B* **76**, 024425.
- Wilkins, S. B., R. Caciuffo, C. Detlefs, J. Rebizant, E. Colineau, F. Wastin, and G. H. Lander, 2006, *Phys. Rev. B* **73**, 060406.
- Wilkins, S. B., J. A. Paixao, R. Caciuffo, P. Javorský, F. Wastin, J. Rebizant, C. Detlefs, N. Bernhoeft, P. Santini, and G. H. Lander, 2004, *Phys. Rev. B* **70**, 214402.
- Willers, T., *et al.*, 2012, *Phys. Rev. Lett.* **109**, 046401.
- Willis, B. T. M., 1987, *J. Chem. Soc., Faraday Trans. 2* **83**, 1073.
- Wong, J., M. Krisch, D. L. Farber, F. Occelli, A. J. Schwartz, T.-C. Chiang, M. Wall, C. Boro, and R. Xu, 2003, *Science* **301**, 1078.
- Wong, J., M. Krisch, D. L. Farber, F. Occelli, R. Xu, T.-C. Chiang, D. Clatterbuck, A. J. Schwartz, M. Wall, and C. Boro, 2005, *Phys. Rev. B* **72**, 064115.
- Wong, J., M. Wall, A. J. Schwartz, R. Xu, M. Holt, H. Hong, P. Zschack, and T.-C. Chiang, 2004, *Appl. Phys. Lett.* **84**, 3747.
- Wray, L. A., J. Denlinger, S.-W. Huang, H. He, N. P. Butch, M. B. Maple, Z. Hussain, and Y.-D. Chuang, 2015, *Phys. Rev. Lett.* **114**, 236401.
- Wulff, M., G. H. Lander, B. Lebech, and A. Delapalme, 1989, *Phys. Rev. B* **39**, 4719.
- Xu, R., J. Wong, P. Zschack, H. Hong, and T.-C. Chiang, 2008, *Europhys. Lett.* **82**, 26001.
- Yakel, H. L., 1969, *J. Nucl. Mater.* **33**, 286.
- Yakhov, F., A. Létoublon, F. Livet, M. De Boissieu, and F. Bley, 2001, *J. Magn. Magn. Mater.* **233**, 119.

- Yaouanc, A., P. Dalmás de Réotier, G. van der Laan, A. Hiess, J. Goulon, C. Neumann, P. Lejay, and N. Sato, 1998, *Phys. Rev. B* **58**, 8793.
- Ye, G., J. Roques, P.-L. Solari, C. Den Auwer, A. Jeanson, J. Brandel, L. J. Charbonnière, W. Wu, and E. Simoni, 2021, *Inorg. Chem.* **60**, 2149.
- Yoo, C.-S., H. Cynn, and P. Söderlind, 1998, *Phys. Rev. B* **57**, 10359.
- Yu, S.-W., J. G. Tobin, J. C. Crowhurst, S. Sharma, J. K. Dewhurst, P. Olalde-Velasco, W. L. Yang, and W. J. Siekhaus, 2011, *Phys. Rev. B* **83**, 165102.
- Zabinsky, S. I., J. J. Rehr, A. Ankudinov, R. C. Albers, and M. J. Eller, 1995, *Phys. Rev. B* **52**, 2995.
- Zachariasen, W. H., and F. H. Ellinger, 1955, *Acta Crystallogr.* **8**, 431.
- Zachariasen, W. H., and F. H. Ellinger, 1957, *J. Chem. Phys.* **27**, 811.
- Zachariasen, W. H., and F. H. Ellinger, 1963a, *Acta Crystallogr.* **16**, 777.
- Zachariasen, W. H., and F. H. Ellinger, 1963b, *Acta Crystallogr.* **16**, 369.
- Zhai, B., Q. Tian, N. Li, M. Yan, and M. J. Henderson, 2022, *J. Synchrotron Radiat.* **29**, 281.
- Zhou, K.-J., *et al.*, 2022, *J. Synchrotron Radiat.* **29**, 563.
- Zimina, A., *et al.*, 2017, *Rev. Sci. Instrum.* **88**, 113113.
- Zurita, C., S. Tsushima, C. Bresson, M. Garcia Cortes, P. L. Solari, A. Jeanson, G. Creff, and C. Den Auwer, 2021, *Chem. Eur. J.* **27**, 2393.
- Zurita, C., S. Tsushima, P. L. Solari, A. Jeanson, G. Creff, and C. Den Auwer, 2022, *J. Synchrotron Radiat.* **29**, 45.
- Zvoriste-Walters, C. E., S. Heathman, R. Jovani-Abril, J. L. Spino, A. Janssen, and R. Caciuffo, 2013, *J. Nucl. Mater.* **435**, 123.